DEVELOPMENT AND *IN VIVO* TESTING OF GELATIN AND SILK-FIBROIN BASED CALCIUM PHOSPHATE BONE CEMENT

by

İbrahim Kapıcı

Submitted to Graduate School of Natural and Applied Sciences
in Partial Fulfillment of the Requirements
for the Degree of Master of Science in
Biotechnology

Yeditepe University
2020

DEVELOPMENT AND *IN VIVO* TESTING OF GELATIN AND SILK-FIBROIN BASED CALCIUM PHOSPHATE BONE CEMENT

APPROVED BY:

Assist. Prof. Dr. Feride Şermin Utku ……
(Thesis Supervisor)
(Yeditepe University)

Prof. Dr. Fatma Neşe Kök ……
(İstanbul Technical University)

Prof. Dr. Gamze Torun Köse ……
(Yeditepe University)

DATE OF APPROVAL: …./…./2020

ACKNOWLEDGEMENTS

I would like to start with expressing my sincerest gratitudes to Assist. Prof. Dr. Feride Şermin Utku for supervising this thesis with her broad expertise, assistance, kind guidance and most importantly with her unlimited patience from the start. Her contribution is what made this thesis possible.

Secondly, I find it very crucial to thank the veterinarian Engin Sümer for the assistance and guidance during all the animal experiments. I should also mention that I am sincerely grateful to Assoc. Dr. Muhammed Hamitoğlu, Prof. Dr. Mustafa Çulha and Prof. Dr. Ferda Özkan.

Also, I am genuinely grateful to my dear colleagues, the biomedical assistants and chemistry assistants of the Yeditepe University, for providing me unconditional help in every possible aspect. Especially, Avram Aruh and Ömer Barış Emek who supported me with their precious friendship and advice throughout our time together.

Lastly, I want to show a wholehearted gratitude to my incredible, beloved family for being there for me regardless of time and place, for all the support they provided whenever I needed one, or even when I didn't need; to my father who is constantly by my side with his vision and valuable thoughts, always ready to make sacrifices for us; to my mother for her humorous manner, which lifts my mood when I need to blow off some steam and for her deep belief in me; and finally, I thank my dearest little sister Fulin, who helps me without saying a word whenever I ask her, with her bright intellect and intuitive approach, whom I dedicate this thesis to.

ABSTRACT

DEVELOPMENT AND *IN VIVO* TESTING OF GELATIN AND SILK-FIBROIN BASED CALCIUM PHOSPHATE BONE CEMENT

Calcium phosphate cement bone replacement materials are used in biomedical and dental applications as composites and coatings, due to their physical and chemical similarity to bone structure. Bone cements are used in hard tissue repair by inducing new bone formation as well as supporting internal fixation. This study was conducted with the aim to produce, characterize and apply gelatin and silk based calcium phosphate cements. The composition of bone cement was based mainly on an inorganic component consisting of hydroxyapatite, tetracalcium phosphate, disodium phosphate, carbonate and an organic component consisting of gelatin and silk fibroin. The various formulations studied varied from each other in terms of gelatin concentration, water content, setting temperature, setting time and the use of Na^{+} versus Ca^{++} as the carbonate cation. The bone cement setting time was determined mechanically using the Vicat Testing Method. Cement samples were further characterized by contact angle analysis, XRD, SEM and FTIR to determine their hydrophilicity, crystal structure, morphology and molecular bonding pattern. The mechanical properties of the cements were studied using the Universal Testing Device. In vivo performance tests were conducted on Sprague-Dawley rats using 3 mm wide defects formed on both sides of the calvarium. The results of characterization indicated formation of Ca-P based bone cement with a minimum setting time of 16.5±0.5 minutes. Among the various formulations studied, cement 80C-3/37 demonstrated a contact angle of 28.8°±1.78, formation of hydroxyapatite crystals with crystal size of approximately 135 nm, Ca/P ratio of 1.71, Calcium solubility of 73.96 µg/µl, Phosphate solubility of 0.24 µg/µl, mechanical strength of 0.31±0.25 MPa, and a setting time of 16.5±0.5 min. The *in-vivo* testing histological scores indicated time-based bone healing in the experimental groups with the superior healing in cement 80C-3/37 implanted animals, wheres the four-week group demonstrating partial and the eight week group complete healing and replacement of the defect by the newly formed calvarial bone.

ÖZET

JELATİN VE İPEK-FİBROİN BAZLI KALSİYUM FOSFAT ÇİMENTOLARININ GELİŞTİRİLMESİ VE *IN VIVO* TESTLERİ

Kalsiyum fosfat çimento bazlı kemik implantları, kimyasal ve fiziksel özelliklerinin kemik yapısına olan benzerlikleri sebebiyle biyomedikal ve dişçilik uygulamalarında kompozitler ve kaplamalar olarak kullanılmaktadırlar. Sert dokuların tedavisinde kullanılan kemik çimentoları yeni kemik oluşumunu tetiklediği gibi doku içerisinde bağlılığı da destekler. Bu çalışma ile jelatin ve ipek bazlı kalsiyum fosfat çimentoların üretimi, karakterizasyonu, ve uygulaması amaçlanmıştır. Kemik çimentosunun yapısında inorganik yapı olarak ağırlıkla hidroksiapatit, tetrakalsiyum fosfat, disodyum fosfat, karbonat ve organik yapı olarak da jelatin ve ipek fibroin kullanılmıştır. Birbirinden farklı formülasyonlarla çalışılmış olup, bu formülasyonlarda jelatin konsantrasyonu, su miktarı, katılaşma sıcaklığı, katılaşma süresi, ve Na^{+} ve Ca^{++} karbonat katyonlarının etkisi karşılaştırılmıştır. Kemik çimento örneklerinin katılaşma süreleri Vicat Testi yöntemi ile mekanik olarak belirlendi. Ayrıca çimentoların karakterizasyonu yüzey gerilim analizi, XRD, SEM, ve FTIR kullanılarak malzemelerin hidrofilitesi, kristal yapısı, morfolojisi, ve moleküler bağ örgüsü belirlendi. Çimentoların mekanik özellikleri Instron evrensel test cihazı ile belirlendi. In-vivo performans testleri ise Sprague-Dawley sıçanlarının kalvariyumunun her iki tarafında birer 3 mm.lik hasar oluşturularak gerçekleştirildi. Karakterizasyon sonuçları Ka-F bazlı kemik çimentosunun en düşük katılaşma süresi olan 16.5±0.5 dakikada oluştuğunu ortaya koydu. Çalışılan çeşitli formülasyonlar arasında hidroksiapatit kristalleri oluşumları gösteren çimento 80C-3/37'nin yüzey gerilimi 28.8°±1.78°, ortalama kristal boyutu 135 nm, Ca/P oranı 1.71, kalsiyum çözünürlüğü 73.96 µg/µl, fosfat çözünürlüğü 0.24 µg/µl, mekanik dayanımı 0.31±0.25 MPa ve katılaşma süresi 16.5±0.5 dakika olarak belirlendi. *İn-vivo* testlerinin histolojik skorları deneysel gruplarda zamana bağlı olarak tam kemik iyileşme gösterdi. 4 haftalık deney gruplarında kısmen, 8 haftalık deney gruplarında da kemik dokusunun tamamımın iyileştiği ve hasarlı dokunun yeni oluşan kalvarial kemik dokusuyla yer değiştirdiğini gösterdi.

TABLE OF CONTENTS

LIST OF FIGURES

LIST OF TABLES

LIST OF SYMBOLS/ABBREVIATIONS

HA	Hydroxyapatite
CDHA	Calcium deficient hydroxyapatite
DCPA	Dicalcium phosphate anhydrous
DCPD	Dicalcium phosphate dihydrate
TTCP	Tetracalcium phosphate
PMMA	Polymethyl-methacrylate
CPC	Calcium phosphate cement
ICPC	Injectable calcium phosphate cement
OHAp	Hydroxyapatite
CHA	Carbonated hydroxyapatite
MCPM	Monocalcium phosphate monohydrate
OCP	Octacalcium phosphate
TCP	Tricalcium phosphate
L	Liters
ml	Milliliters
µl	Microliters
g	Grams
mg	Milligrams
µg	Micrograms
mM	Millimolar
µM	Micromolar
sT	Setting temperature
min	Minutes
st	Setting time
gel	Gelatin
P/L	Powder to liquid ratio

1. INTRODUCTION

Bone is a very complex material consisting of collagen and hydroxyapatite organized at nine levels of hierarchy [1]. The various bone features ranging from collagen arrays at the nanometric level to the osteons at the micrometric level to that of the spongious and cortical bone at the milimetric level demonstrate the intriguing complexity of this structure. In the introduction of this thesis, various aspects of bone structure and physiology will be discussed in order to describe the difficult task of formulating a bone cement as bone replacement material, which can partially fulfill the complexity of bone as a natural composite.

1.1. BONE STRUCTURE

Bone is a hard tissue consisting of an organic matrix, inorganic mineral salts, bone cells, and water [2]. The organic part of bone constitues 40 percent of the dry weigh bone. Type I Collagen is the main component of the organic portion. The inorganic component of bone mainly consists of hydroxyapatite (HA), so that calcium and phosphate can be stored. Addition to that; osteoblasts, osteoclasts and osteocytes are the cellular components of the bone [3].

With some variation, bone tissue is formed as part of the skeletal system in all vertebrates. The skeletal system not only protects the vital organs, but also provides motility. In addition, inorganic ions in bone maintain the calcium-phosphate (Ca-P) balance in the body. During the life span of an organism, bone tissue is continuosly deposited and resorbed so that bone can grow in size and shape. In vertabrates skeletal system is developed by two different mechanisms called intramembranous ossification and endochondral ossification. These mechanisms are carried out by diffentiated mesenchymal stem cells [4].

1.1.1. Major Bone Components

1.1.1.1. Hydroxyapatite

Hydroxyapatite, a form of calcium apatite, is a naturally occurring mineral. HA has a hexagonal close packed crystal structure with a stochiometric Ca/P ratio of 1.67 (Figure 1.1).

HA can be easily synthesized and transformed into powder form. In addition to that, HA is the most stable calcium apatite under geological conditions, differentiating it from biological apatite, i.e. carbonated hydroxyapatite (CHA), which also appears as a stable form under physiological conditions, specifically temperature, pH and body fluids [5]. Thus, there are basic differences between highly crystalline hydroxyapatites and poorly crystalline biologic apatites which display differing results due to the biological *in-vivo* processes. While hydroxyapatite is modified by physicochemical processes such as dissolution, reprecipitation, and incorporation of foreign ions, bone mineral (CHA) is resorbed and deposited by cellular activity [6].

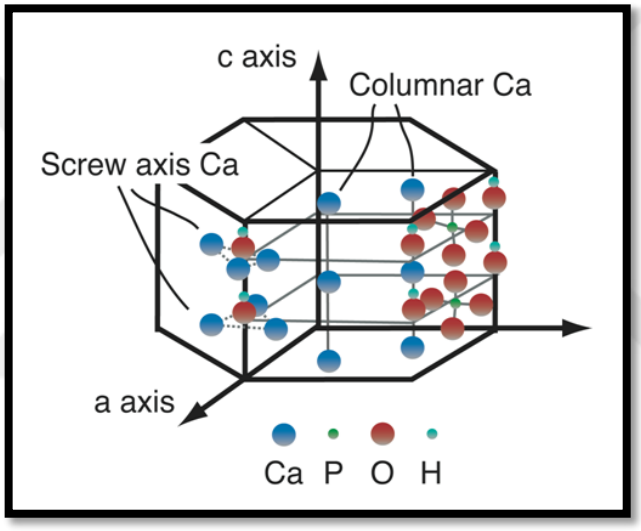

Figure 1.1. Crystal structure of Hydroxyapatite [5].

A transient amorphous calcium phosphate phase (ACP) with a Ca/P molar ratio of 1.5 precipitates spontaneously from highly supersaturated solutions and is suggested to convert to apatite at physiologic pH via an octacalcium phosphate (OCP) transition phase due to the presence of surface HPO_4^{2-} ions, making it poorly crystalline. With increased alkalinity, HPO_4^{2-} content is reduced, more carbonate substituted, more crystalline and thus a more organized structure is obtained. Thus, the apatite in bone, dentin and cementum have small crystal size, high degree of carbonate substitution, substantial OH deficiency, lattice vacancies and increased solubility. The small crystal size is indicative of adsorption of a large percentage of ions and proteins to the surface of the crystal as in biologic hydroxylapatite the mineral phase associates with the organic matrix [6].

The human bone and dentin mineral has plate-like, nanosized crystals with a length of ~20–50 nm and a width of 12–20 nanometers, with the enamel crystals having about 10 times larger sizes, where the apatite crystals develop in the c-axes direction parallel to the collagen fibril axis. The collagen and associated proteins play an important role in determining the nucleation, growth, and proliferation of these crystals [6].

Cells secrete organic mattices to form scaffolds for biomineralization, and then deposit crystals. During biomineralization, extracellular matrix proteins which interact with mineralized collagen in bone and dentin change with time. Primarily, crystal formation takes place in the generous environment containing the SIBLING (Small Integrin-Binding LIgand N-linked Glycoprotein) proteins. Interactions with bone modelling regulator proteins (such as osteocalcin) are increased during bone crystal development. In dentistry, since the roots are remodelled in response to disease under cellular regulation, dentin mineral is remodeled to a far lesser degree. Mineral enamel is not remodelled, so when mineralization takes place, the enamel matrix is degraded. Owing to dissolution due to bacterical acids resulting in dental cavities, enamel minerals can be lost [6].

1.1.1.2. Collagen

Type I Collagen is the major protein component of the extra cellular matrix (ECM), making 25 percent of all the protein content of the body. Among more than 27 types of collagen, Type I is the most common type in bone, dentin and cementum combined. Collagen polypeptide chains, made of glycine, proline and hydroxyproline, wind into a triple-helical fibrillar triplicate, a unique structure consisting of three collagen chains, which undergo post-translational modifications such as proline and lysine hydroxylation, and attachment of glucose and galactose to hydroxylysine residues [7]. Collagen fibrils form arrays with gaps formed between the collagen fibril ends, making the nonmineralized tissue scaffold. The gaps between collagen fibrils are then filled with bone fluid, which then become sites of mineralization, then spreading through the matrix. Noncollagenous proteins, found tightly associated with collagen, enable mineralization [6,8].

1.1.1.3. Mineralization

Formation of organic matrix, where mineralization will occur, is carried out by cells, and these cells regulate the sequential flux of ions into extracellular matrix, as well as, send signals to stop biomineralization. Extracellular matrix encircles the cells, and becomes suitable volume to deposit minerals; it also determines the area that mineralization takes

place as well as crystal size and type. Mineral deposition in dentin and bone become possible with a collagen that ensured by fibroin additionally; size and order of the fibroin fibrils become limiting factor for the crystal deposition [6].

1.1.2. Bone Forming Cells

1.1.2.1. Osteoblasts

Osteoblasts, large cells responsible for bone formation and remodelling, have a single cuboidally shaped nucleus. During bone formation osteoblasts secrete collagen-rich ECM, which is later mineralized. Mesenchymal progenitor cells (MSCs) differentiate into cells responsible for two different types of bone formation. During intramembranous ossification, MSCs differentiate into osteoblastic linage. In endochondral ossification, MSCs differentiate into chondrocytes and perichondral cells [9].

1.1.2.2. Osteoclasts

Osteoclasts, enlarged cells with multi nuclei, belong to macrophage lineage [10]. Osteoclasts are responsible for bone degradation. Osteoclasts are responsible for bone resorption. Osteoclast formation depends on the interactions between osteoblasts, proteins secreted from osteoblasts and monocytic precursors [9].

1.1.2.3. Osteocytes

Osteocytes are cells that are derived from the osteoblasts. They are usually found inside the ECM, secreted by the osteoblasts. Osteocytes are linked with each other via the canaliculi by their cytoplasmic extentions [9].

1.1.3. Bone Deposition and Resorption

1.1.3.1. Intramembranous Ossification

Skull bones, facial bones, and collar bone are formed by intramembranous ossification. Osteoblast progenitor cells in the mesenchymal membrane differentiates to mature osteoblast cells and secretes Type I Collagen and proteoglycan forming the osteid [10]. The secreted collagen and proteoglycan are able to bind calcium salts. As a result of calcium binding, the osteoid matrix becomes calcified. Usually, the osteoid layer separates

osteoblasts from the area that calcification occurs. As calcification continues, bone spicules spread out from the ossification center (Figure 1.2) and calcified spicules surrounded by the MSCs form the periosteum. Osteoblast cells on the inner surface of periosteum deposits osteiod matrix parallel to generated spicules. In this way, layers of bone are formed [3,6].

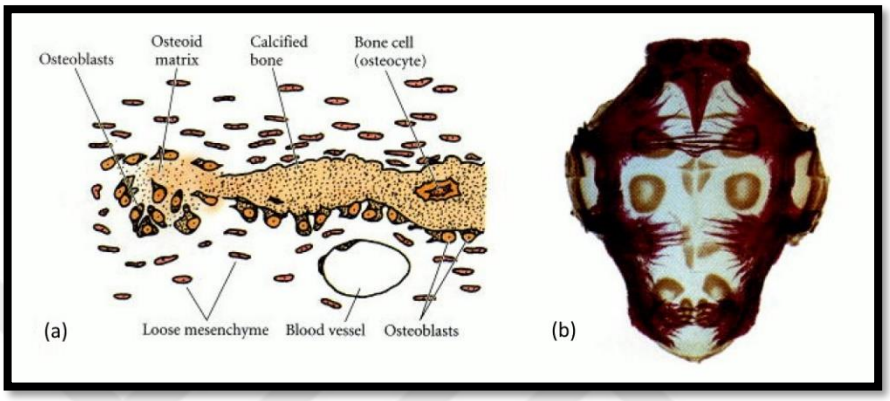

Figure 1.2. (a) Bone precursor cells, (b) bone spicules is spreading out from the ossification center [10].

1.1.3.2. Endochondral Ossification

Endochondral ossification starts with differentiation of MSCs into cartilage cells. These cells become condensed and differentiate into chondrocytes. With a division and proliferation of chondroctytes, bone model is formed. Chondrocytes secrete a cartilage specific ECM during division. In the following step, chondrocytes discontinue dividing to gain volume and become hypertrophic chondrocytes. Enlarged chondrocytes modify the secreted matrix by adding Type X collagen and fibronectin. Thus, altered matrix can be mineralized by calcium phosphate. Hypertrophic chondrocyte death occur due to apoptosis and the bone marrow takes place of the hypertrophic chondrocytes. When the cartilage cells die, cells on the cartilage model differentiate into osteoblasts and they start constructing the bone matrix on the degraded cartilage. In the end, degraded cartilage is substituted by bone (Figure 1.3) [3,6].

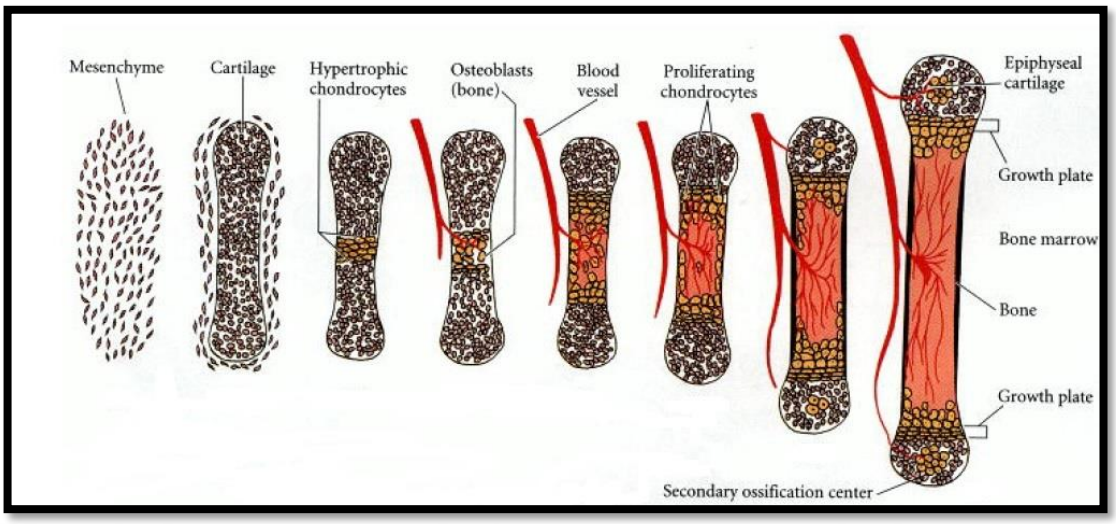

Figure 1.3. Endochondral ossification [10].

1.1.3.3. Bone Resorption

Bone resorption takes place during endochondral ossification and bone remodelling and carried out by the osteoclasts. Before bone resorption, osteoblasts secrete the proteins required for osteoclast formation and maturation. After the osteoclasts mature, molecular interactions takes place between osteoblasts and osteoclasts [4].

RANK is a transmembrane receptor from a tumor necrosis factor (TNF) family, and are found on the cell surface of the osteoclast precursors. RANK is responsible for osteoclast maturation. RANK has a ligand, RANKL, that is secreted from the osteoblasts. Molecular signalling between RANK and RANKL evokes the nuclear factor kB (NFKB) and transcriptional activation of targeted genes takes place for the recruitment, differentiation, activation and survival of osteoclasts. On the bone surface, there are Howship's Lacunae (where bone resorption occurs) and osteoclasts are found against it. When the osteoclastic activity and bone degradation starts, osteoclasts secrete Cathepsin K (CTSK) enzyme on the ruffled border to absorb osteoids. Osteoclasts secrete another enzyme called Tartrate-resistant Acid Phosphatase (TRAP) to dissolve hydroxyapatite crystals. Maturated osteoclast cells secrete integrin protein to attach vitronectin on the bone surface. Sealing zone is formed with a binding of integrin and vitronectin. When the sealing is complete, osteoclast creates an acidic enviroment to increase solubility by producing carbonic anhydrases. Another enzyme, Cathepsin B is also secreted from the osteoclasts to carry out organic matrix

degradation. As a result of absorption, calcium ion concentration increases as a function of time. If the calcium concentration increases more than the osteoblasts can deposit that will lead to failure of bone remodelling. To prevent that, calcitonin receptor on the osteoclasts regulates the calcium concentration by inhibiting osteoclast activity [2,3,5].

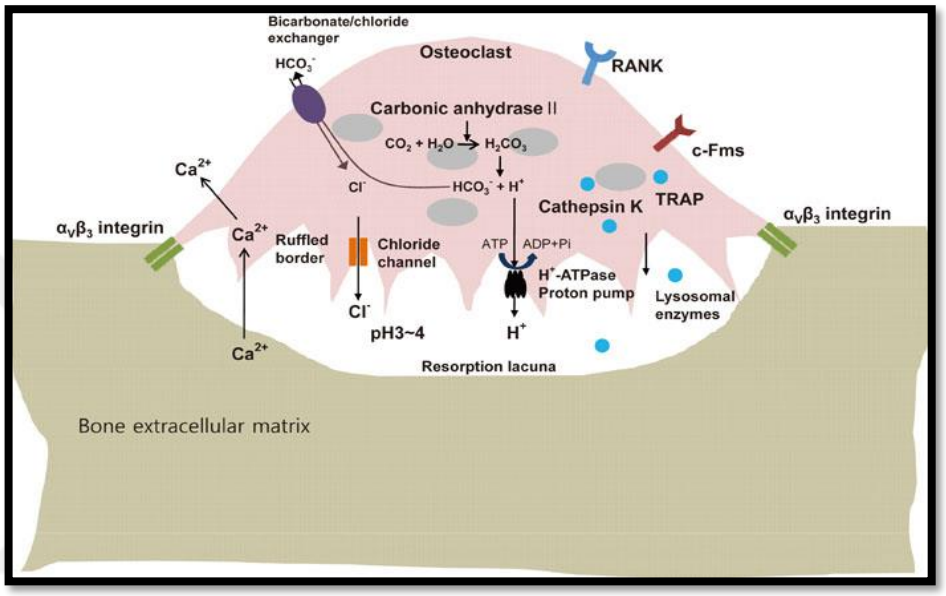

Figure 1.4. Osteoclast attachment to the bone surface.

OPG is a osteoclastogenesis inhibiting factor that is a soluble receptor of RANK and secreted from osteoblasts to balance effect of RANKL. OPG is a decoy recoptor for RANKL, and it prevents RANK and RANKL signalling by binding to the RANKL, which then prevents osteoclastic activity. Also OPG has important role during bone remodelling. Throughout bone remodelling, osteoblasts increase the OPG formation therewith, bone formation increases and bone resorption decreases [2,3,5]. To summarize, osteoclast activitation is regulated by RANK-RANKL interactions and the osteoclast inhibition is regulated by calcitonin and OPG (Figure 1.4).

1.2. BONE TYPES

1.2.1. Based on Shape

In vertebrates, bone can be classified as long bones, short bones, flat bones, irregular shaped bones, and sesamoid bones. Each bone type has different formation mechanism as given below in more detail. Long bones contain a cylindrical tube in the middle (diaphysis), a transition section (metaphysis) above the diaphysis, and epiphysis on the top of metaphysis. In long bone, the diaphysis and the epiphysis are derived from different ossification centers and are separated by cartilage layer, called the growth plate (Figure 1.5). Additionally, long bones are formed by endochondral ossification [3]. Short bones are usually cube shaped bones and consist of spongy bone with a thin compact bone layer on the exterior. Carpal bones and tarsal bones can be given as example to short bones. As it in long bones, short bones are also formed by endochondral ossification [3]. Flat bones are formed by intramembranous ossification and inner and outer sections of the flat bones consist of compact bone, but between these sections are filled by cancellous bone. Skull bones are perfect example of flat bones [3]. Irregular bones are comprimised from spongy bone in the inner region and that region is covered by thin layer of compact bone. Endochondral ossification is responsible from formation of irregular bones. The scapula is classified as irregular bone [3]. Sesamoid bones are buried in the tendons and they are subtype of short bones. Like short bones they are also formed by endochondral ossification. Patella and pisiform can be given as example to sesamoid bones [3].

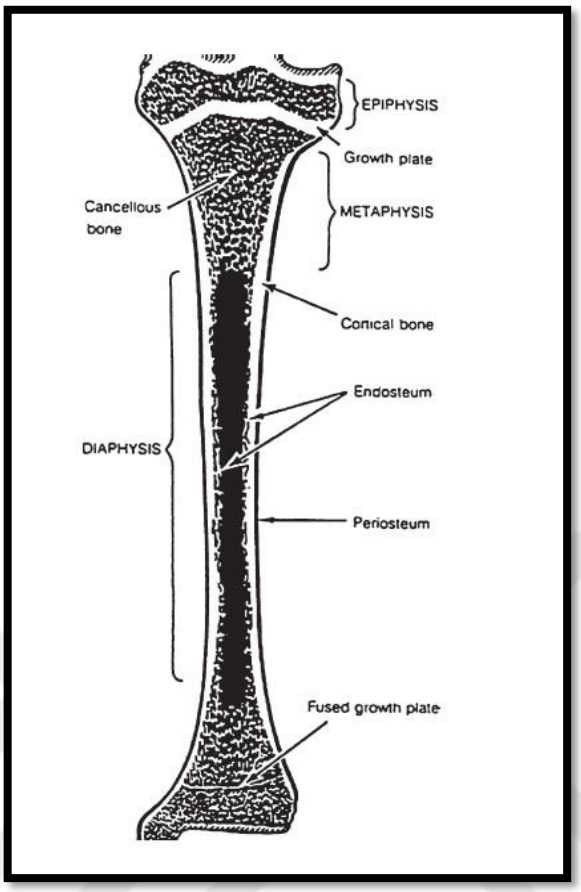

Figure 1.5. Long bone tibia. Diaphysis, metaphysis, and epiphysis are labeled [3].

1.2.2. Based on Porosity

1.2.2.1. Compact Bone

Compact bone is strong and dense bone; therefore, it provides protection for internal organs and supports the body. Compact bone consist of osteons (Haversian System) and each osteon is formed from concentric calcified matrix rings (lamallae) (Figure 1.6). Osteons contain Haversian canal in the center, and blood vessels, nerves, and lymphatic vessels are placed in the Haversian canal. These vessels, and nerves brach out by interpenetrating Haversian canal to reach the periosteum and the endosteum, as well as connecting canals named Volkmann's canals. In addition to that; osteocytes are located in the space (lacuna) between the calcified matrix rings. Eventually, canaliculi connect with the canaliculi of other lacunae and with the Haversian canal. Therefore; transportation of nutrients and wastes is enabled in bone [3].

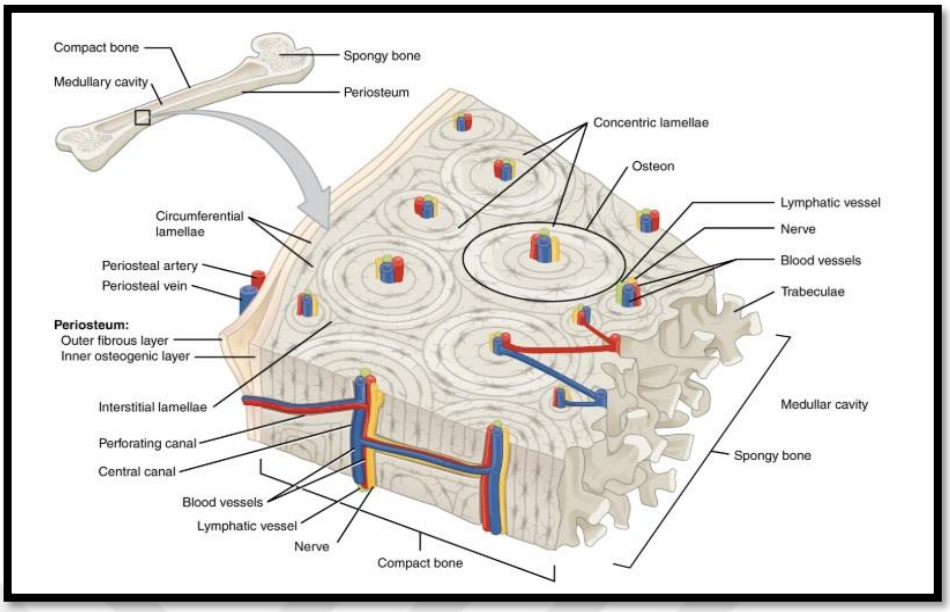

Figure 1.6. Compact bone [3].

1.2.2.2. Cancellous (Spongy) Bone

Spongy bone is found in the bone marrow and similar to the compact bone, spongy bone also has osteocytes in the lacunae, but they are found as lattice-like network of matrix (trabeculae) (Figure 1.7). Trabeculae generate stress lines to provide strength to the bone. Spacing between the trabeculae maintains the balance of compact bone by making bone lighter and reduces the muscle work required to move bone [3].

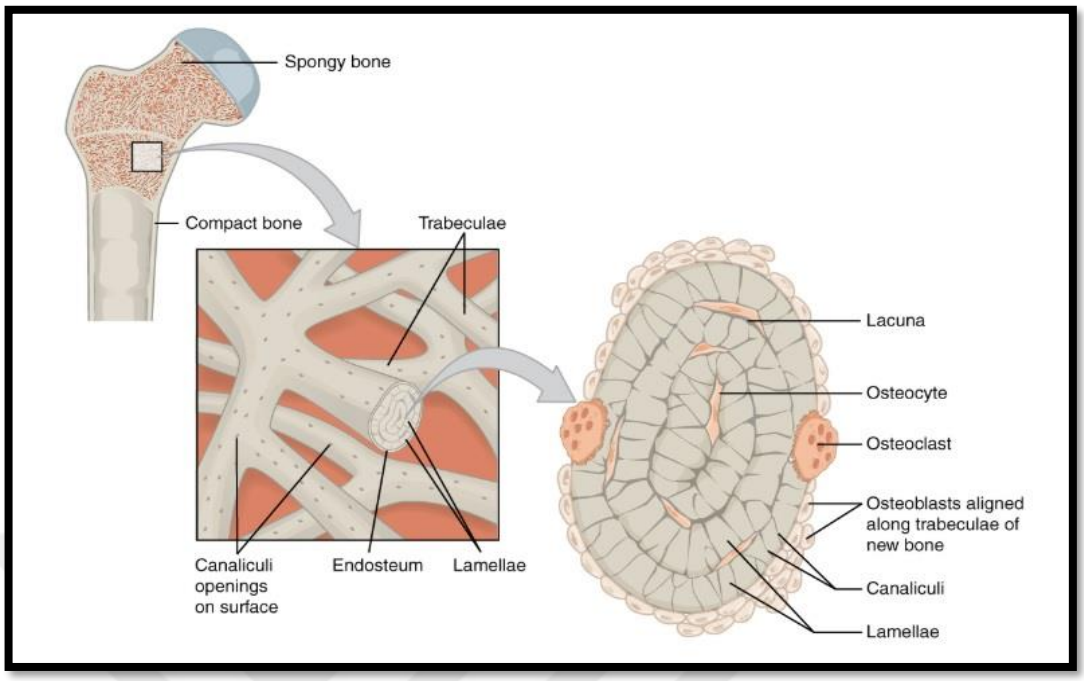

Figure 1.7. Spongy bone [3].

1.3. BONE GRAFT MATERIALS

1.3.1. History of Hard Tissue Implants and Biomaterials

In the 1800's it was nearly impossible to perform complicated surgeries because people of that era didn't know of sterilization techniques and the use of anaesthesia. In the 1860's British surgeon Joseph Lister found the sterilization technique; and subsequently, Crawford Long, an American pharmacist and a surgeon combined Lister's aseptic surgery technique with the use of anaesthesia making it possible to perform more complicated and longer operations [11].

In the area of bone tissue treatment, first attempts for the treatment of bone fractures and joints were practiced by British surgeon and physican Sir William Arbuthnot Lane and his coworkers. They invented a fracture implant made of stainless steel for the treatment of a tibial fracture. In 1926, Ernest William Hey Groves achived to treat femural neck fracture using stainless steel. He was also the first person to use carpentry screws to nail during the operation. During World War II and in the years that followed, German surgeon Martin

Kirschner developed the usage of wires and pins for the fixation of bone fractures. As a result of his research, new implants were developed by mixing the refined materials. At the same time, antibiotics were discovered and inflammation risk during the operation was reduced. Besides that, in 1967 Computed Tomography (CT) scan was invented by Sir Godfrey Hounsfield, making it possible to obtain visual information from the body. Those improvements enhanced both medical and biomedical studies all over the world [11].

1.3.2. Graft Materials

Basically, bone graft material is an implant which encourages the bone reconstruction by ensuring osteoconductive and osteoinductive mechanisms on the implantation site. Bone graft materials are classified as autografts, allografts, and xenografts [12]. Comparison of bone graft materials are given in Table 1.1.

1.3.2.1. Autografts

In autografts, bone tissue harvested from the patient is implanted back into the same patient. Tissue harvesting can be conducted on both cancellous bone and cortical bone. Regardless of the harvested bone tissue, both of the grafts support osteoconductive and osteoinductive interactions. Even though mechanically sufficient, autografts might cause morbidity at the donor site. Additionally, the patient might encounter with post-operative pain and complications at both donor and recipient sites [7,8].

1.3.2.2. Allografts

Allograft bone tissue is harvested from the cadavres of the same species in different shapes and sizes. Contrary to autograft, allograft does not cause donor morbidity; however, it may cause complications due to infection transmission [7,8]. Sterilization and tissue processing techniques, lyophilization and irradiation are required to eliminate infections, in order to reduce immune system rejections against to implant. On the other hand, those techniques affect the mechanical strength of the bone graft. Despite these processing procedures, harvested bone tissue still has the risk of infection and immune system rejection [14].

Table 1.1. Comparison of bone graft features [12].

Bone Graft	Structural Strength	Osteo-Conduction	Osteo-Induction	Osteogenesis
Autograft				
Cancellous	No	+++	+++	+++
Cortical	+++	++	++	++
Allograft				
Cancellous				
Frozen	No	++	+	No
Freeze-Dry	No	++	+	No
Cortical				
Frozen	+++	+	No	No
Freeze-Dry	+	+	No	No
Demineralized Allogeneic Cancellous Chips	No	+	++	No

1.3.2.3. Xenografts

Xenoraft bone substitutes are harvested from species other than the human. Xenoraft applications are limited by the host's powerful immune system response. Therefore, xenograft bone substitutes are deproteinated and defatted to reduce immune system reaction, but those procedures demolish the matrix proteins that are required for osteoinductive mechanisms [12].

1.3.3. Silk

Silks are mostly defined as protein polymers that are spun into fibers by some lepidoptera larvae such as silkworms, spiders, scorpions, mites and flies. Silk is composed of two proteins: fibroin and sericin [15]. Silks are hierarchically regulated from the amino level up

to micro- and macroscopic structures .Silks represent a new family of advanced biomaterials due to their unique attributes of high mechanical strength and excellent biocompatibility.

Silk-fibroin is a natural protein that is generally obtained from silkworms. Both fibroin and sericin are proteins insoluable in water. Sericin is more amorphous and easily attacked by chemicals. Fibroin is cystalline and more resistant to chemicals. While sericin is a glue-like protein surrounding the fibers to hold them together in cocoon case, fibroin is the core filament of silk (Figure 1.8).

Mulberry silk which is mainly produced by Bombyx mori and has been modified to use in surgery and tissue engineering applications. These silk cocoons are mainly consist of 72–81 percent of a fibrous protein fibroin core and 19–28 percent glue protein sericin in the surrounding region. Bombyx mori fibroin has been used to attach and growth osteoblast, fibroblast, hepatocyte and keratinocyte, substrates for enzyme immobilization and has also been used in tissue engineering applications as an alternative to collagen [16].

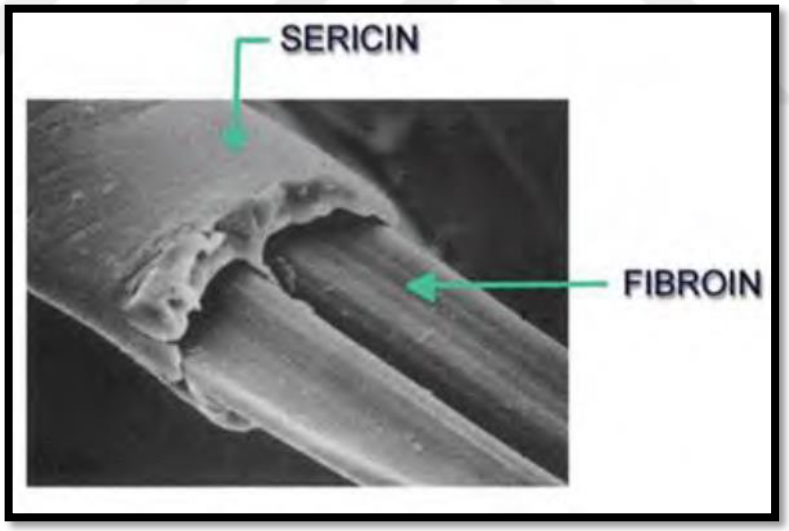

Figure 1.8. Protein composition of silk-fibroin [17].

Fibroin is the major biomedical application of silk, which is a hydrophobic protein with a molecular mass of around 400 kDa. Silk-fibroin proteins' essential structure chiefly comprises of the amino acid succession which is organized intermittently (Gly-Ser-Gly-Ala-Gly-Ala)n . Silk I, silk II and silk III stand out as structural forms of fibroin.

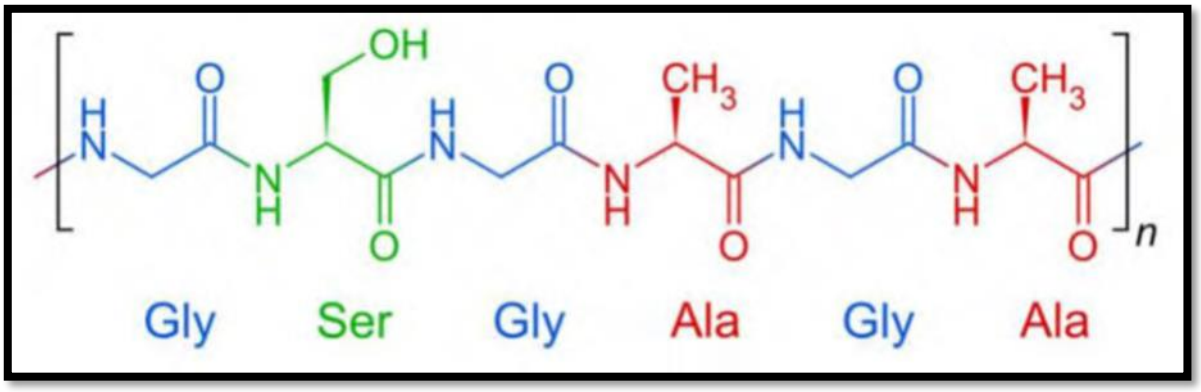

Figure 1.9. Silk-fibroin primary structure [18].

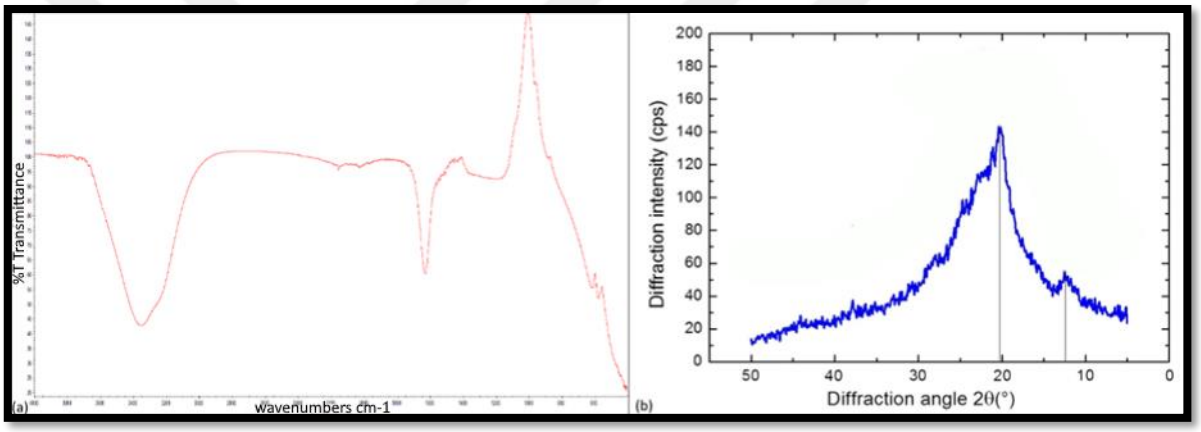

Figure 1. 10. (a) The FT-IR and (b) XRD spectra of prepared silk solution [19].

The distinctive type of fibroin, as released from the silk glands of Bombyx mori, is Silk I. Silk II refers to the modification of fibroin molecules in spun silk, has a higher strength and mostly used in industrial applications. Most of the biomaterial properties of the silk is determined by the secondary structure and the hierarchial organization of silk fibroin. The hydrophilic domains consisting of the repeated amino acid sequence of the silk polymer chains are form β-sheets. The hydrophilic connections between these hydrophobic domains are the amorphous part of the secondary structure and consist of bulky and polar side chains. In amaorphous blocks, the chain conformation is a random coil, giving elasticity to silk [20,21]. Silk III, which is a virginally discovered structure of the silk-fibroin has a helical structure which consist of air-water assembled interfacial silk. The high glycine content enables tight pressing of the β-sheets, which results in silk fibroin's inflexible, inextendable

structure. The silk-fibroin protein is composed of layers of antiparallel β-sheet structures as a result of the dominance of hydrophobic domains consisting of short side chain amino acids in the primary sequence. These structures enable tight packing of stacked sheets of hydrogen bonded anti-parallel chains of the protein. Also as given in Figure 1.10 typical FTIR peaks of silk fibroin is visible at 3296 cm^{-1} for Amide A 1630, 1516, 1231 cm^{-1} for Amide I, II, III respectively.

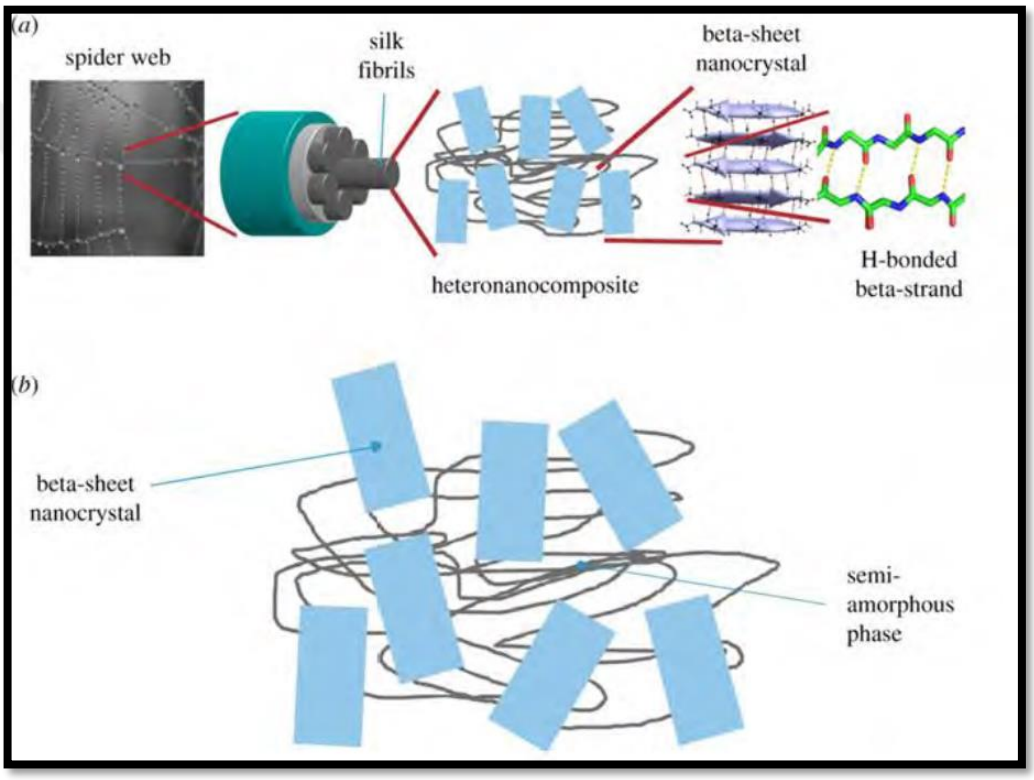

Figure 1.11. (a) Hierarchical structure of silk spider, (b) β-sheet nanocrystals are immersed in an matrix of semi-amorphous protein [18].

1.3.3.1. Forms of Silk Fibroins

Forms of silk-fibroin can branch into six categories such as silk fibers, non-woven silk-fibroin mats, silk-fibroin film, silk-fibroin porous sponge, silk-fibroin hydrogels and microspheres. Silk fibers derived from the bombyx mori type of silkworm cocoon are used to produce regenerated silk solution to produce surgical sutures. Non-woven silk-fibroin mats from reprocessed local silk filaments or by electrospining have expanded surface region and roughness which have been used for cell seeding. Silk-fibroin film, produced by blending with other polymers with aqueous or organic solvent systems, can have oxygen and

water vapor permeability dependent on the content of silk I and silk II structures [22]. Sing porogen, gas, foaming, and lyophilisation, porous sponge scaffolds, used in tissue engineering applications for cell attacahements, proliferation, and migration, as well as for nutrient and waste transport, have been created. Solvent-based sponges prepared before pouring into a mold and freezing with the addition of a small amount of solvent (ethanol, methanol) into aquous silkf fibroin solution. With aqueous-based processing, sponges with high porosity and improved mechanical strength have been obtained. Stiffness, compressive strength, and modulus were elevated with an increase in percent silk-fibroin solution utilized in the process [23]. Regeneration of silk-fibroin solution may also be processed to produce three dimensional sponge scaffold for use in tissue engineering. Porous three dimensional silk sponges used in various study to generate various connective tissue. Hydrogels based production of silk-fibroin involves the process of gelation controlled by temperature, calcium ion concentration, pH and polymer blending [24].Silk-fibroin microspheres may be used in drug delivery applications. With nanometer to micron range diameters and spherical shape, silk microspheres can be readily produced by mixing regenerated fibroin solution with lipid vesicles that act as templates to efficiently load biological molecules in an active form for sustained release. The lipid could then be subsequently removed by methanol or sodium chloride treatments [24].

1.3.3.2. Mechanical Properties of Silk Fibroin

Silk-fibroin is used as biomaterial due to its high elasticity, toughness, crystallinity, strength and high compression properties. Semi-crystalline structure of the silk protein provides elasticity for the protein. Additionally, β-sheet crystals, and interphase between the β-sheet crystals and semi-crystalline structure is the reason oof silk's unique mechanical properties. Tensile properties, elasticity, and biodegradation of the silk is releated with its β-sheet structure and modification of these properties can be conducted with cross-linking process. When fibroins are spun into fibers, the poly-alanine blocks form β-sheet crystals that crosslink the fibroins into a polymer network with great stiffness, strength and toughness [25]. Silk is incomparable in terms of strength and toughness among all the natural and synthetic fibers. Strength-to- density ratio indicate that silk is up to ten times higher than that of steel. Silk is tougher than steel and kevlar. Interestingly, an increase in rate of loading causes an increased elongation and thus greater resistance to rupturing. This is a typical feature of all natural silks including silkworm silk, which represents an exception to most

fibrous material. In general, silk has an excellent ability to absorb energy at high rates of loading [26].

1.3.3.3. Biocompatibility of Silk-Fibroin

Biomaterial characteristics, including implantation site, size, geometry, and surface topography can influence the level of the foreign body response. Biocompatibility; the ability of a material to perform with an appropriate host response in a specific application. The biocompatibility property of silk-fibroin protein is one of the significant reasons for the wide range of application on biomedical field. Case of immunogenicity is closely connected with biocompatibility. Sericin, a glue-like protein that keeps the fibroin fibres together, has been described as the source of immunogenic reactions. Suitably degummed and sterilized silk products have good biocompatibility and can be compared with other commonly used biomaterials such as poly (lactic acid) and collagen.

Not only non-autologous biomaterials but also some adverse immunological events associated with silk proteins can cause foreign body response due to the non-mammalian origin. Some incidents of delayed hypersensitivity of silk sutures in rare cases are suggested to be due to the presence of silk gum-like protein sericin [27,28]. RGD supplemented B.mori silk has been shown to support cell attachment and growth to a greater extend than B.mori silk [29].

Immunological reactions to biomaterials are a substantial consideration. Macrophage response to fibroin film educed that film form or fiber form do not cause any significant immunological response *in-vivo*. Inflammatory reaction to fibroin films *in-vivo*, similar to that of collagen. Another study suggested that B. mori silk braided into yarns elicited a mild inflammatory response after seven days *in-vivo* [30]. Besides that gelatin-coated Bombyx mori silk point to a minimal inflammatory response. Spider silk has been found to invoke a similar inflammatory response to materials used clinically such as collagen and medical-grade polyurethane [31].

1.3.3.4. Biodegradation Properties of Silk-Fibroin

Silk is degradable but over longer time periods due to preteolytic degradation usually mediated by foreign body response. Biodegradation of silk-fibroin is mostly performed by enzymes. Enzymes on the surface of a substrate were adsorb and ester bonds of an amino

acids were become hydrolized [32]. Appliccation of proteolytic enzymes to the silk films cause a decrease on sample weight and degree of polymerization. Also these modifications may vary with type of enzymes, the enzyme-to-substrate ratio, and the degradation time [33]. Proteolytic enzymatic degradation is better at degrading low molecular weight silk fibroins and non-compact structures [34]. The molecular weight and structure of silk biomaterials, so structure and molecular weight of polymers are two main factors influencing the biodegradation process.

1.3.3.5. Silk-fibroin in Biomedical Application

Silk-fibroin can be processed into foams, films, fibers and meshes. As a protein, silk-fibroin is a polyampholyte with anionic and cationic side chains and an isoelectric point. Dissolved in water, silk-fibroin has a net negative charge, due to the negatively charged amino acids with respect to positively charged amino acids. If subjected to an electric field, the protein will experience a net force towards the positive electrode and will accumulate on it, forming a gel-like adhering coating [35]. Control drying, water annealing or alcohol immersion ensure the stability and improve the β-sheet structure. Fibroin films induced bone tissue growth *in-vitro* when seeded with osteoblasts. When the films were chemically decorated with the peptide RGD to promote integrin interactions for adhesion, the induction of bone formation *in-vitro* was significantly enhanced [36]. Silk-fibroin when evaluated as films, foams and fibers, may offer a ‘new’ alternative biomaterial for use as matrices in tissue engineering where mechanically tough, long-term degradable materials are needed. the matrix degradation into biocompitable fragments or monomer capable of being metabolized by host cell. Though, the rate of degradation must match or be less than the rate of tissue in growth and development.

1.3.4. Gelatin

Gelatin is a high molecular weight compound that derived from collagen [7]. Collagen is a fibrous protein with triple helix structure and major component of the connective tissues like skin, bone and tendon [37]. Gelatin consists of α- amino acids that are linked with each other by peptide bonds. Properties of the chain molecules depend on the amino acids and their alignment [38]. Gelatin is widely used in food engineering, biomedical engineering, and pharmaceutical studies. Gelatin has applications in drug-delivery systems, encapsulation

techniques, wound patches, hydrogels, and tissue engineering studies as tissue scaffolds [39,40]. Modified gelatin can be produced and side chains of the gelatin can function as sites for reactions with other molecules, modifying the characteristics of gelatin . Gelatin can be degraded by heat, acids, and alkalis. The molecular weight or gelling factor of gelatin can affected differently according to degradation method [38].

In the nature, gelatin does not occur naturally so it is synthesized from physically or chemically degraded collagen. Gelatin is commonly synthesized by two methods. In the first method, tissue of interest is treated with lime slurry to transform amide groups of collagen into carboxyl groups [38]. This treatment also reduces the length of the polypeptide chains. After lime slurry treatment, gelatin is obtained through heating process at 65 °C at neatural pH [38]. As a second method, skin tissue sample is treated with dilute acid, where collagen is dissolved with warm water at 40 °C. In this method, amide groups of the collagen are not affected and the properties of the generated gelatin may differ from the gelatin that is synthesized with the first method [38].

Collagen polypeptide chains, made of glycine, proline and hydroxyproline, wind into a triple-helical fibrillar triplicate, a unique structure consisting of three collagen chains (Figure 1.12). The FTIR spectrum of the gelatin indicates the peaks at 3411 cm^{-1} for NH, 2874-2938 cm^{-1} region for CH_2, 1649 cm^{-1} for Amide I, 1537 cm^{-1} for Amide II, 1243 cm^{-1} for Amide III, 1085 scm^{-1} for CH_3 and 554-607 cm^{-1} range for the COC. Additionly, XRD peaks can be found at the 21.87° 2θ and 37.87° 2θ.

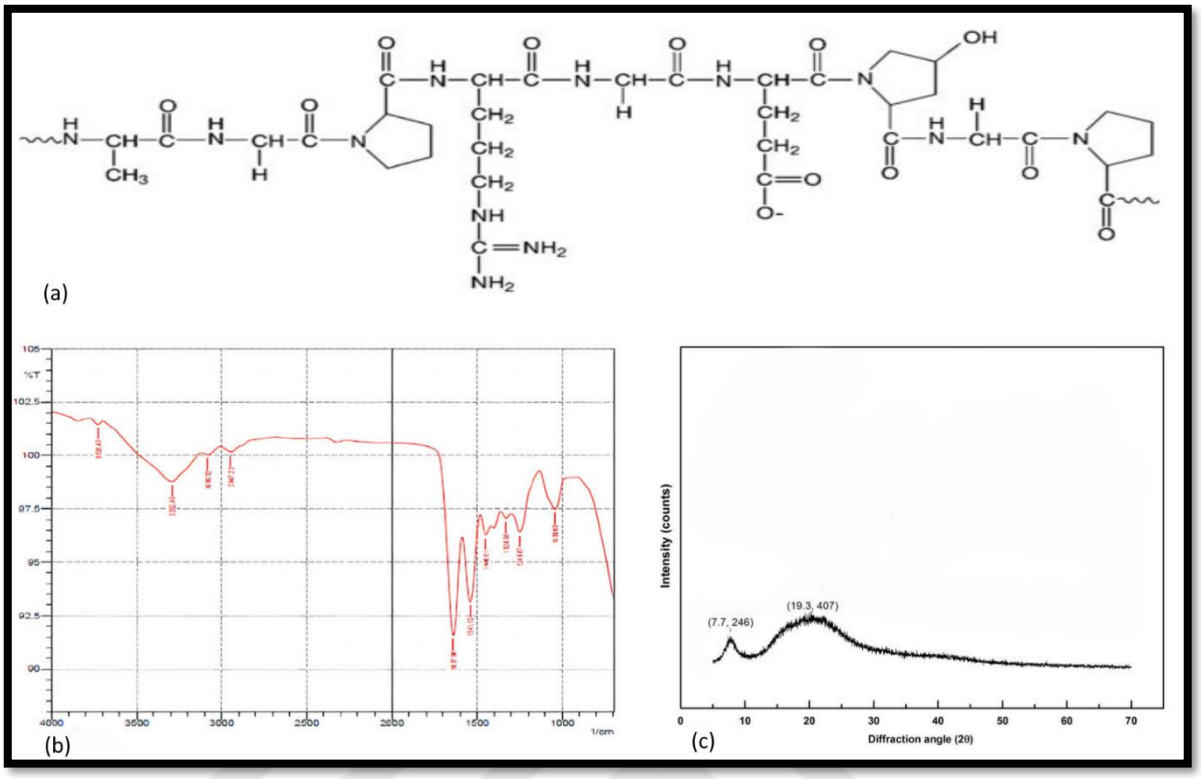

Figure 1.12. (a) Polypeptide chain of gelatine, (b) the FT-IR, and (c) XRD spectra of gelatin [41–43].

1.4. BONE CEMENTS

In this section brief information is given about the conventional methods for the bone substitutions and implants. Further details are given in the following sections.

1.4.1. Polymethyl Methacrylate Cements

Polymethyl metacrylate (PMMA) is a transparent and thermoplastic polymer, which is developed by Otto Röhm in 1901. It is usually synthesized by mixing the powder buthyl acrylate with the liquid methyl methacylate. Mixture transforms into putty form and hardens. Hardening proceses is carried out by an exothermic polimerization reaction, increasing the temperature to 70 °C. PMMA cements are low cost, easy-to-handle/use polymers. On the other hand, high heat generated during the polymerization reaction might cause tissue necrosis. In addition, as a result of its low viscosity, the setting time increases and the

polymer might leak after application. Additionally, PMMA cements exhibit fragile characteristics under high pressure [44,45].

1.4.2. Biphasic Coatings

Biphasic coatings were first introduced in 1975. They can be produced in many ways; commonly produced by sintering calcium-deficient hydroxyapatite or amorphous calcium phosphate. Biphasic coatings are used as bone grafts, bone substitute biomaterials, in maxiollofacial operations, and dental applications. Their structure shows similarities to bone structure and they can be easily degradable. Biodegradation rate can be modified by the changing ratios of hydroxyapatite and tricalcium phosphate. Additionally, they exhibit osteoconductive properties. However, micro grain sized and non-homogenous particle structure cause poor mechanical strength, and complicates porosity control [44].

1.4.3. Calcium Phosphate Cements

Calcium phosphate cements are formed by a reaction between a powder mixture and a liquid solution (Figure 1.13). Powder mixture can contain different types of calcium phosphate apatites, like monocalcium phosphate, dicalcium phosphate, (α/β) tricalcium phosphate, tetracalcium phosphate, and amorphous calcium phosphate. Liquid component of the calcium phosphate cements can contain distilled water, disodium hydrogen phosphate solution, and potassium dihydrogen phosphate solution [46]. As a result of such variety, calcium phosphate cements can be generated with a different formulations. Calcium phosphate cements are self-setting biomaterials due to hydrolysis reaction that occur during preparation. Setting of the cement starts with the hydrolysis reaction and continues with dissolution and precipitation. Calcium phosphate cements support the osteoconductive and osteoinductive mechanisms due to their structural similarities to the hydroxyapatite mineral in bone. Calcium phosphate cements do not generate heat during the reaction contrary to PMMA cements. These features of the calcium phosphate cements make them promising materials for the bone tissue engineering, orthopedic, and dental applications [47].

1.4.4. Injectable Calcium Phosphate Cements

Injectable calcium phosphate cements are used for treatment of bone fractures due to osteoporosis and traumas. Injectable calcium phosphate cement fills the voids in the deformed bone tissue and reclaims the integrity of bone [48]. Osteoporosis is commonly encountered in elder people and post-menopausal women. For these patients orthopedic applications can be limited due to their age and the risk that comes along with elderness. Surgical operations are applied only in the case of continuous deformity and dysfunction [48].

Injectable calcium phosphate cements are easily prepared and its injectable morphology eases the application. After the application, the setting reaction takes place without any heat genaration, with the cement hardening within minutes. Injectable calcium phosphate cements have higher viscosity than the PMMA cements and during their application leakage is not encountered [49].

1.4.5. Commercially Available Calcium Phosphate Cements

Bone Source is the first self-setting calcium phosphate cement invented by Brown and Chow for the treatment of bone tissue [46]. Bone Source is prepared by a reaction of TTCP and DCPD in the presence of water with a powder to liquid ratio of 4. Pure HA is formed as a final product of the reaction. Initial setting time starts within 15 to 20 minutes and complete hardening takes more than 4 hour at 37 °C. Bone Source has 34 MPa compressive strength when its fully hardened. It has been marketed by Stryker Howmedica Leibinger Inc. (Freiburg, Germany) with a name Bone Source. Application of the Bone Source is limited due to its long hardening time and requirement of dry envoirement to set [46,50].

Norian Skeletal Repair System and Cranifacial Reconstruction System are invented and marketed by Norian Corp. (Cupertino, USA). Norian SRS and CRS consist of mono calcium phosphate, α-tri calcium phosphate, and calcium carbonate as the powder component and an aqueous settting accelerator sodium phosphate as the solvent [50,51]. Carbonated apatite is formed as the final product of the reaction , where the initial setting starts within 10 minutes of mixture and become completely set after 12 hours. Cement reaches 55 MPa compressive strength after the 12 hour setting process [52].

Another product in the market, α-Bone Substitute Material, Emborc (Jacksonville, USA), is invented by Etex Corporation and marketed by Lorenz Surgical company as Emborc. It consists of amorphous calcium phopshate precursors and initial setting starts within 15-20 minutes at 37 °C. This cement has limitations because the setting reaction does not occur after 1 hour in the room temperature [46].

1.5. AIM OF THIS STUDY

Calcium phosphate cement based bone replacement materials are used in biomedical and dental applications as composites and coatings, due to their similarity to bone structure and osteoconductive and osteoactive properties. Bone cements are used in hard tissue repair by inducing new bone formation as well as supporting internal fixation in the tissue.

The aim of this study was to produce a gelatin, silk-fibroin based calcium phosphate cement for the treatment of craniofacial defects. The main objective was to simulate the chemical, mechanical and physiological properties of bone using natural components comparable to those of bone. For that purpose, a calcium phosphate cement (CPC) with similar chemical and mechanical properties to that of bone was produced. Collagen component of bone was replaced with the silk-fibroin polymer to enhance the mechanical and osteoconductive properties of the CPC [33,45]. In addition, gelatin was used to enhance both hydrophilicity and the mechanical properties of cements [53]. Tetracalcium phosphate used in the preparation of bone cements was prepared in the laboratory by sintering at 1300 °C and characterized using XRD, SEM and FT-IR. It was then included in the formulations to react with disodium phosphate in order to produce hydroxyapatite forming bone cement. Hydroxyapatite component of bone was biomimicked by reacting TTCP with DCPD in presence of HA. The cement system with equimolar ratios of TTCP and DCPD was expected to form CDHA as the final product [54]. Formation of CDHA in calcium phosphate cement systems was investigated at differing reactant ratios, cation types and temperatures [40,55]. Cements were also prepared at 1:2 molar ratios of TTCP and DCPD respectively. As various formulations were studied at this point, concerns regarding the gelatin and silk-fibroin concentration, the water content while taking the hydration shell of the polymeric component, the setting temperature and the use of Na^{+} versus Ca^{++} as the carbonate cation

were taken into consideration and various compounds were formulated. The water concentration and its absorption by gelatin was investigated [56,57]. The effect of temperature on the chemistry and porosity of the cements was examined at 25 °C, 37 °C, 50 °C, 65 °C and 80 °C in order to understand if the cement could be produced at these temperatures to be shaped using 3D printed molds [58]. The CPC formulations were characterized and tested *in-vivo* and evaluated using the histological scoring method [59–61]. The selection or elimination criteria depended initially on visual evaluation, simple tactile evaluation and the setting temperature. Further analysis included evaluations of the results of the FT-IR analysis, the contact angle analysis, the XRD analysis, and the SEM-EDS imaging which provided the Ca/P ratio. At the last stage of evaluations, the results of the dissolution tests and the mechanical tests were used to make conclusive decisions on the selection of cements to be implanted.

2. MATERIALS AND METHODS

2.1. MATERIALS

In this section, materials and chemicals used in the study are presented. The chemicals used in the cement systems are given in Table 2.1.

Table 2.1. Chemicals used in the CPC.

Chemical Name	Formula	Supplier
Tetracalcium phosphate (TTCP)	$Ca_4(PO_4)_2O$	Lab-produced
Dicalcium phosphate dihydrate (DCPD)	$CaHPO_4 \cdot 2H_2O$	Sigma-Aldrich
Hydroxyapatite (HA)	$Ca_5(PO_4)_3(OH)$	Sigma-Aldrich
Calcium carbonate	$CaCO_3$	Sigma-Aldrich
Sodium carbonate	Na_2CO_3	Sigma-Aldrich
Disodium hydrogen phosphate	Na_2HPO_4	Sigma-Aldrich
Calcium chloride dihyrate	$CaCl_2 \cdot 2H_2O$	Sigma-Aldrich
Ethanol	C_2H_5OH	Sigma-Aldrich
Ammonium dihydrogen phosphate	$NH_4H_2PO_4$	Sigma-Aldrich
Calcium acetate monohydrate	$Ca(CH_3COO)_2 \cdot H_2O$	MERCK

2.1.1. Tetracalcium Phosphate Synthesis

TTCP is one of the key elements used in dental and orthopedic cement systems. TTCP powder was produced using the solid state process following the procedure of Jalota et al. [62] with the minor change in the sintering temperature, i.e. the muffle furnace temperature of 1300 °C was used instead of 1230 °C. Detailed procedure is given below.

i. Muffle furnace setted to 300 °C.
ii. 7.709 grams of ammonium dihydrogen phosphate was ground into fine powder using agate mortar and pestle.
iii. 24.505 grams of calcium acatate monohydrate was added to the mortar and mixed with ammonium dihydrogen phosphate for 45 minutes.
iv. After the mixing process, the mixed powder contained in alumina jar was placed in the muffle furnace, pre-heated at 300 °C for 30 minutes.
v. Heated powder mixture was taken out from the muffle furnace and gently mixed and in agate mortar for 15 minutes.
vi. Mixed powder was heated to 800 °C for 1 hour.
vii. The powder was taken out and further mixed for 15 minutes.
viii. The powder was placed in the furnace and heated to 1300 °C for 6 hours (Figure 2.1).
ix. Powder was placed in a desiccator for 15 minutes to prevent absorption of moisture.
x. The powder was gently ground for 3 minutes and reheated to 1300 °C for 6 hours.
xi. Finally, the powder was taken out and let to quench at room temperature (Figure 2.2).

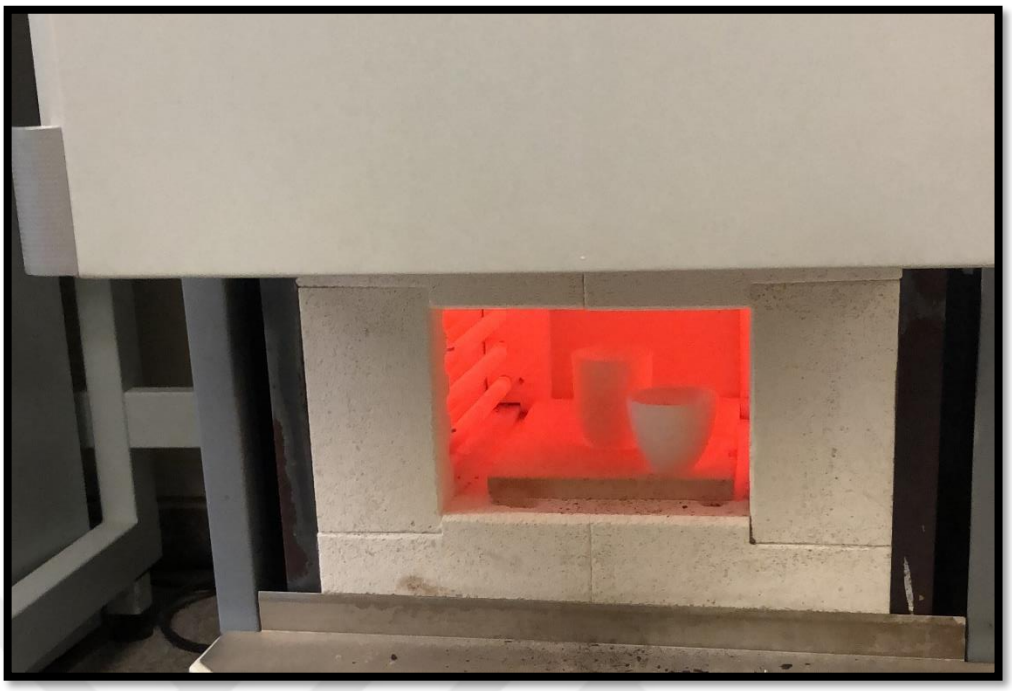

Figure 2.1. TTCP synthesis in the muffle furnace.

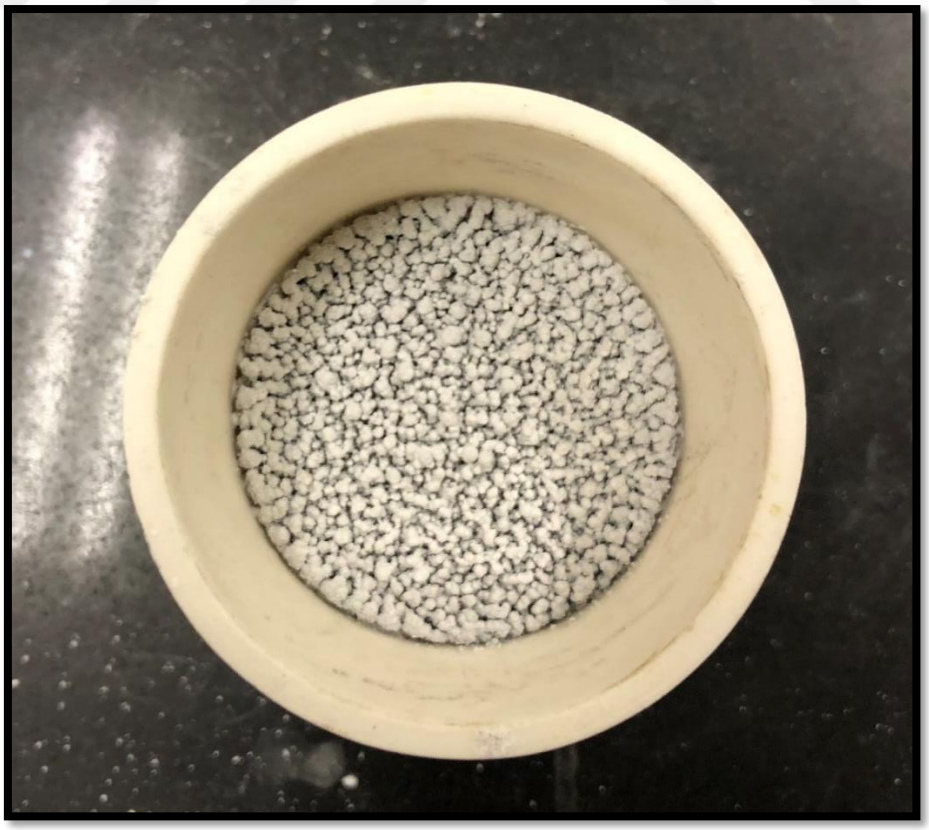

Figure 2.2. Synthesized TTCP powder

2.1.2. Silk Solution Preparation

i. 1.002 g of silk was weighed and cut into small pieces.

ii. 1.001 g of Na_2CO_3 was dissolved in 200 mL of distilled water at 80 °C.

iii. Silk was added to Na_2CO_3 solution and boiled intermittently three times for 20 minutes each, with a through rinse between each carbonate wash.

iv. Rinsed silk fragments were dried using a heat gun.

v. 100 mL of ternary solvent was prepared using $CaCl_2.2H_2O$, C_2H_5OH, and distilled H_2O with a mole ratio of 1:2:8 respectively.

vi. The terniary solution ratios were as follows: for 1 g silk fabric, 14.7 g $CaCl_2.2H_2O$ was dissolved in 11.9 mL ethanol (96.4 v/v percent) and 14.4 g distilled water.

vii. Dried silk pieces were placed in 100 mL ternary solution at 40 °C until the silk fragments were completely dissolved (Figure 2.3).

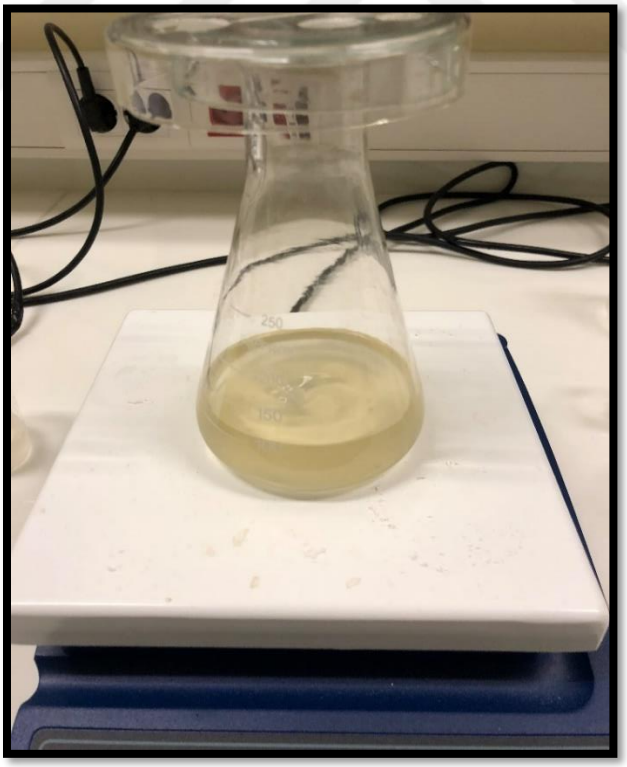

Figure 2.3. Silk-fibroin solution.

2.1.3. 1 M Na_2HPO_4 Solution Preparation

i. 14.196 grams of Na_2HPO_4 was weighed.
ii. 100 milliters of distilled water was measured.
iii. Na_2HPO_4 was dissolved in distilled water by stirring.

2.1.4. Simulated Body Fluid (SBF) Preparation

SBF was prepared in the guidance of Tas et al. [63]. Recipe is indicated below.

i. 6.547 g of NaCl was weighed.
ii. 2.268 g of $NaHCO_3$ was weighed.
iii. 0.373 g of KCl was weighed.
iv. 0.178 g of $Na_2HPO_4{\cdot}2H_2O$ was weighed.
v. 0.305 g of $MgCl_2{\cdot}6H_2O$ was weighed.
vi. 0.368 g of $CaCl_2{\cdot}2H_2O$ was weighed.
vii. 0.071 g of Na_2SO_4 was weighed.
viii. 6.057 g of $(CH_2OH)_3CNH_2$ was weighed.
ix. 40 mL of 1 molar HCl solution was prepared for the pH adjustments.
x. Reagents were dissolved, one by one with a given order in 700 mL of deionized water. Before adding the 6^{th} reagent, $CaCl_2{\cdot}2H_2O$, 15 mL of 1 molar HCl was added to prevent turbidity in the solution.
xi. When the solutions were dissolved temperature increased to 37 °C and HCl was used for titration to adjust pH 7.4.
xii. After the pH set to 7.4 total volume of the solution was completed to 1 L by adding deionized water.

2.2. CALCIUM PHOSPHATE CEMENT PREPARATION

Different types of cement (C) were prepared using various chemicals at different ratios in order to determine an adequate formulation. As a result of trials conducted, out of the thirteen different cement types prepared, the compounds with the chemical contents given in Table 2.2 were chosen for further analysis. There were slight variations among the cements, which were introduced with the aim to compare the formulations from various aspects, i.e. setting temperature, porosity, pore size, Ca/P ratio, and the final compound obtained.

Table 2.2. Chemical content of cements

Cement No	**58C-2/50**	**75C-5/25**	**76C-5/37**	**73C-5/50**	**69C-5/65**	**70C-5/80**	**79C-3/25**
TTCP (g)	0.673	0.673	0.673	0.673	0.673	0.673	0.673
DCPD (g)	0	0.632	0.632	0.632	0.632	0.632	0.632
DCPA (g)	0.5	0	0	0	0	0	0
HA (g)	0.105	0.105	0.105	0.105	0.105	0.105	0.105
$CaCO_3$ (g)	0	0.105	0.105	0.105	0.105	0.105	0.105
Na_2CO_3 (g)	0.105	0	0	0	0	0	0
Gelatin (g)	0.027	0.072	0.072	0.072	0.072	0.072	0.042
1M Na_2HPO_4 (µL)	433	433	433	433	433	433	433
0.5M Na_2HPO_4 (µL)	0	0	0	0	0	0	0
dH_2O (µL)	30	280	280	280	280	280	177
1 wt% Silk Sol (µL)	124	124	124	124	124	124	124
Setting Temp. (°C)	50	65	80	50	25	37	25
Setting Time at 25 °C (min)	23.5	88	76.5	73.5	82.5	-	33

Table 2.2. (Continue'd).

Cement No	80C-3/37	81C-3/50NaH	82C-3/50NaL	83C-3/50NCH	84C-3/50NCL	85C-0/50
TTCP(g)	0.673	0.673	0.673	0.673	0.673	0.673
DCPD(g)	0.632	0.6323	0.6323	0.6323	0.6323	0.316
DCPA(g)	0	0	0	0	0	0
HA(g)	0.1056	0.1056	0.1056	0.1056	0.1056	0.105
$CaCO_3$(g)	0.1056	0	0	0.528	0.528	0
Na_2CO_3(g)	0	0.1056	0.1056	0.528	0.528	0
Gelatin (g)	0.0428	0.0428	0.0428	0.0428	0.0428	0
1M Na_2HPO_4 (µL)	433	433	433	433	433	0
0.5M Na_2HPO_4 (µL)	0	0	0	0	0	494
dH_2O (µL)	177	402	280	402	280	0
1 wt% Silk Sol (µL)	124	124	124	124	124	0
Setting Temp. (°C)	37	50	50	50	50	50
Setting Time at 25 °C (min)	63.5	-	-	-	-	43.5

2.2.1. Cement 75C-5/25 (sT 25 °C)

i. 0.673 g of TTCP, 0.632 g of DCPD, 0.105 g of HA, 0.105 g of $CaCO_3$, and 0.072 g of gelatin were weighed, placed in agate mortar, gently ground and mixed using agate pestle.

i. 280 µL of distilled water was added to the powder mixture.

ii. 433 µL of 1 M Na_2HPO_4 solution was mixed in.

iii. 124 µL of silk solution was mixed in for 3 minutes.

iv. After mixing, the cement, transformed into a putty, was placed in 2 mL syringe.

v. The prepared cement was placed in the incubator set at 25 °C for 24 hours (Figure 2.4).

2.2.2. Cement 79C-3/25 (sT 25 °C)

i. 0.673 g of TTCP, 0.632 g of DCPD, 0.105 g of HA, 0.105 g of $CaCO_3$, and 0.042 g of gelatin were weighed, placed in agate mortar, gently ground and mixed using agate pestle.

i. 177 µL of distilled water was added to the powder mixture.

ii. 433 µL of 1 M Na_2HPO_4 solution was mixed in.

iii. 124 µL of silk solution was mixed in for 3 minutes.

iv. After mixing, the cement, transformed into a putty, was placed in 2 mL syringe.

v. The prepared cement was placed in the incubator set at 25 °C for 24 hours (Figure 2.4).

2.2.3. Cement 76C-5/37 (sT 37 °C)

i. 0.673 g of TTCP, 0.632 g of DCPD, 0.105 g of HA, 0.105 g of $CaCO_3$, and 0.072 g of gelatin were weighed, placed in agate mortar, gently ground and mixed using agate pestle.

ii. 280 μL of distilled water was added to the powder mixture.

iii. 433 μL of 1 M Na_2HPO_4 solution was mixed in.

iv. 124 μL of silk solution was mixed in for 3 minutes.

v. After mixing, the cement, transformed into a putty, was placed in 2 mL syringe.

vi. The prepared cement was placed in the incubator set at 37 °C for 24 hours (Figure 2.4).

2.2.4. Cement 80C-3/37 (sT 37 °C)

i. 0.673 g of TTCP, 0.632 g of DCPD, 0.105 g of HA, 0.105 g of $CaCO_3$, and 0.042 g of gelatin were weighed, placed in agate mortar, gently ground and mixed using agate pestle.

i. Afterwards, 177 μL of distilled water was added to the powder mixture.

ii. 433 μL of 1 M Na_2HPO_4 solution was mixed in.

iii. 124 μL of silk solution was mixed in for 3 minutes.

iv. After mixing, the cement, transformed into a putty, was placed in 2 mL syringe.

v. The prepared cement was placed in the incubator set at 37 °C for 24 hours (Figure 2.4).

2.2.5. Cement-58C-2/50 (sT 50°C)

i. 0.673 g of TTCP, 0.500 g of DCPA, 0.105 g of HA, 0.105 g of Na_2CO_3, and 0.027 g of gelatin were weighed, placed in agate mortar, gently ground and mixed using agate pestle.

ii. 30 µL of distilled water was added to the powder mixture.

iii. 433 µL of 1 M Na_2HPO_4 solution was added to the mixture and mixed.

iv. 124 µL of silk solution was added to the mixture and mixed for 3 minutes.

v. After mixing, the cement was transformed into a putty, was placed in 2 mL syringe.

vi. The prepared cement was placed in the incubator set at 50 °C for 24 hours (Figure 2.4).

2.2.6. Cement 73C-5/50 (sT 50 °C)

i. 0.673 g of TTCP, 0.632 g of DCPD, 0.105 g of HA, 0.105 g of $CaCO_3$, and 0.072 g of gelatin were weighed, placed in agate mortar, gently ground and mixed using agate pestle.

ii. 280 µL of distilled water was added to the powder mixture.

iii. 433 µL of 1 M Na_2HPO_4 solution was mixed in.

iv. 124 µL of silk solution was mixed in for 3 minutes.

v. After mixing, the cement, transformed into a putty, was placed in 2 mL syringe.

vi. The prepared cement was placed in the incubator set at 50 °C for 24 hours (Figure 2.4).

2.2.7. Cement 81C-3/50NaH (sT 50 °C)

i. 0.673 g of TTCP, 0.632 g of DCPD, 0.105 g of HA, 0.105 g of Na_2CO_3, and 0.042 g of gelatin were weighed, placed in agate mortar, gently ground and mixed using agate pestle.

i. 402 µL of distilled water was added to the powder mixture.

ii. 433 µL of 1 M Na_2HPO_4 solution was mixed in.

iii. 124 microliters of silk solution was mixed in for 3 minutes.

iv. After mixing, the cement, transformed into a putty, was placed in 2 mL syringe.

v. The prepared cement was placed in the incubator set at 50 °C for 24 hours (Figure 2.4).

2.2.8. Cement 82C-3/50NaL (sT 50 °C)

i. 0.673 g of TTCP, 0.632 g of DCPD, 0.105 g of HA, 0.105 g of $CaCO_3$, and 0.042 g of gelatin were weighed, placed in agate mortar, gently ground and mixed using agate pestle.

i. 281 µL of distilled water was added to the powder mixture.

ii. 433 µL of 1 M Na_2HPO_4 solution was mixed in.

iii. 124 µL of silk solution was mixed in for 3 minutes.

iv. After mixing, the cement, transformed into a putty, was placed in 2 mL syringe.

v. The prepared cement was placed in the incubator set at 50 °C for 24 hours (Figure 2.4).

2.2.9. Cement 83C-3/50NCH (sT 50 °C)

i. 0.673 g of TTCP, 0.632 g of DCPD, 0.105 g of HA, 0.052 g of $CaCO_3$, 0.052 g of Na_2CO_3, and 0.042 g of gelatin were weighed, placed in agate mortar, gently ground and mixed using agate pestle.

i. 402 µL of distilled water was added to the powder mixture.

ii. 433 µL of 1 M Na_2HPO_4 solution was mixed in.

iii. 124 µL of silk solution was mixed in for 3 minutes.

iv. After mixing, the cement, transformed into a putty, was placed in 2 mL syringe.

v. The prepared cement was placed in the incubator set at 50 °C for 24 hours (Figure 2.4).

2.2.10. Cement 84C-3/50NCL (sT 50 °C)

i. 0.673 g of TTCP, 0.632 g of DCPD, 0.105 g of HA, 0.052 g of $CaCO_3$, 0.052 g of Na_2CO_3, and 0.042 g of gelatin were weighed, placed in agate mortar, gently ground and mixed using agate pestle.

i. 281 µL of distilled water was added to the powder mixture.

ii. 433 µL of 1 M Na_2HPO_4 solution was mixed in.

iii. 124 µL of silk solution was mixed in for 3 minutes.

iv. After mixing, the cement, transformed into a putty, was placed in 2 mL syringe.

v. The prepared cement was placed in the incubator set at 50 °C for 24 hours (Figure 2.4).

2.2.11. Cement 85C-0/50 (sT 50 °C)

i. 0.673 g of TTCP, and 0.316 g of DCPD were weighed, placed in agate mortar, gently ground and mixed using agate pestle.

i. 495 µL of 0.5 M Na_2HPO_4 solution was added to the powder mixture.

ii. After mixing, the cement, transformed into a putty, was placed in 2 mL syringe.

iii. The prepared cement was placed in the incubator set at 50 °C for 24 hours (Figure 2.4).

2.2.12. Cement 69C-5/65 (sT 65 °C)

i. 0.673 g of TTCP, 0.632 g of DCPD, 0.105 g of HA, 0.105 g of $CaCO_3$, and 0.072 g of gelatin were weighed, placed in agate mortar, gently ground and mixed using agate pestle.

ii. 280 µL of distilled water was added to the powder mixture.

iii. 433 µL of 1 M Na_2HPO_4 solution was mixed in.

iv. 124 µL of silk solution was mixed in for 3 minutes.

v. After mixing, the cement, transformed into a putty, was placed in 2 mL syringe.

vi. The prepared cement was placed in the incubator set at 65 °C for 24 hours (Figure 2.4).

2.2.13. Cement 70C-5/80 (sT 80 °C)

i. 0.673 g of TTCP, 0.632 g of DCPD, 0.105 g of HA, 0.105 g of $CaCO_3$, and 0.072 g of gelatin were weighed, placed in agate mortar, gently ground and mixed using agate pestle.

ii. 280 µL of distilled water was added to the powder mixture.

iii. 433 µL of 1 M Na_2HPO_4 solution was mixed in.

iv. 124 µL of silk solution was mixed in for 3 minutes.

v. After mixing, the cement, transformed into a putty, was placed in 2 mL syringe.

vi. The prepared cement was placed in the incubator set at 80 °C for 24 hours (Figure 2.4).

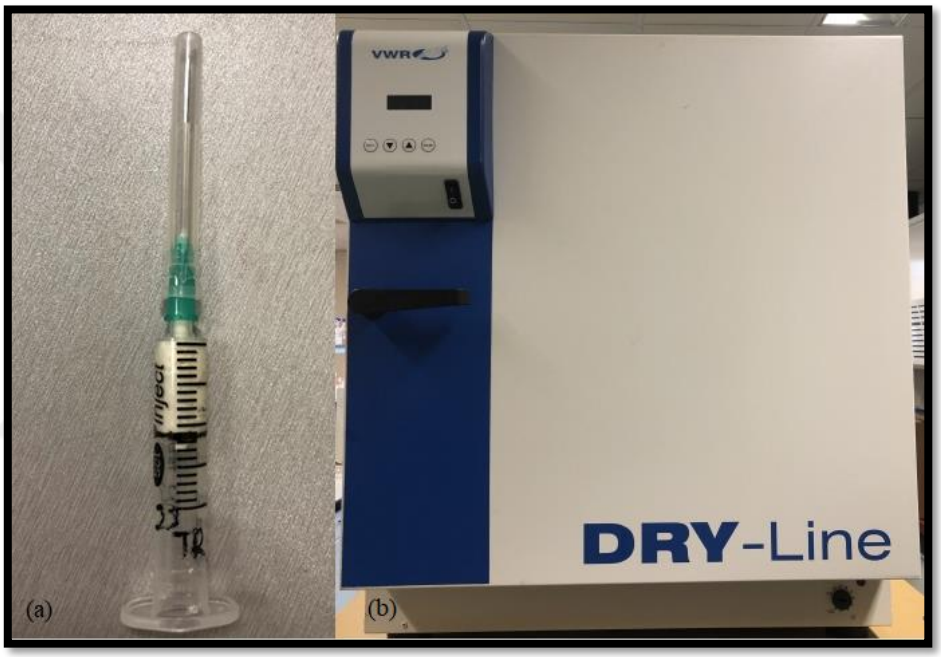

Figure 2.4. (a) Cement placed in syringe (b) before the incubation step.

2.3. CEMENT CHARACTERIZATION AND SURFACE MORPHOLOGY

2.3.1. The Contact Angle

For the contact angle measurements, samples were molded as 2 x 1 cm diameter (⌀) cylinders. All the samples were gently polished with 800 Grid Emery paper to eliminate any surface irregularities and inclines. Therefore, homogenized samples were obtained and any failure due to surface differences were eliminated. Measurements were conducted using KSV CAM 101 contact angle measurement device (KSV Instruments Ltd., Finland) (Figure

2.5). Measurements were conducted with 5 ml. of distilled water using Hamilton syringe. 12 images were taken for each sample and recording started 5 seconds after the first drop. Images were taken with a 1 second interval for each specimen. Contact angle calculations were estimated using KSV CAM 101 contact angle program and on average of the these intervals were taken as the final contact angle value [64].

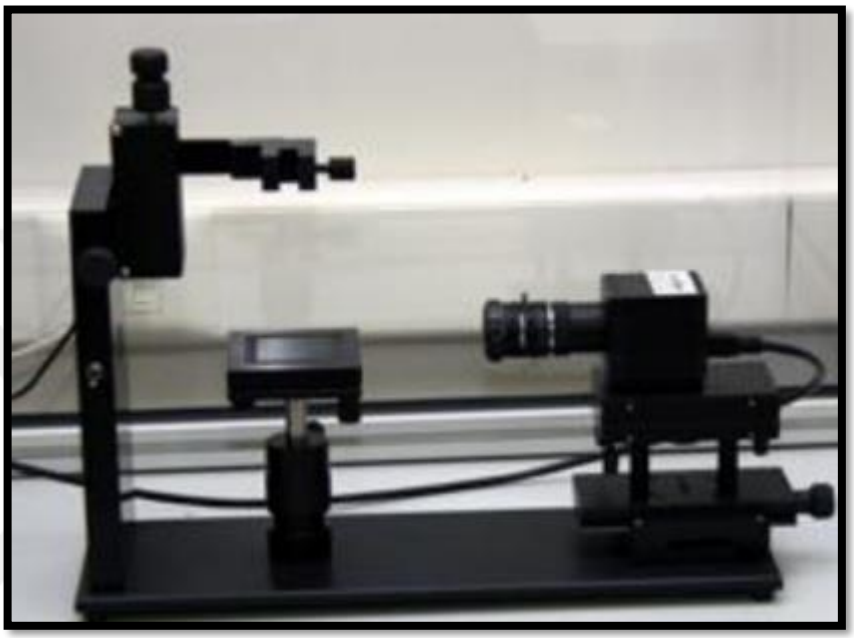

Figure 2.5. The KSV CAM 101 contact angle goniometer.

2.3.2. Fourier-Transform Infrared Spectrometer (FTIR)

In this study, FTIR was used to determine structure characterization of prepared TTCP powders, and calcium phosphate cements. All the measurements were performed by Nicolet IS50 ATR spectroscopy device (Madison, USA) (Figure 2.6). Samples were crushed into fine powder using agate mortar and pestle and placed into the FT-IR device. For each sample, data was collected using OMNIC 9 software, where the experiment setup was adjusted to 16 number of scans with a resolution of 4 cm^{-1} in the wavenumber range of 400-4000 cm^{-1} [62].

Figure 2.6. Nicolet IS50 ATR device.

2.3.3. The X-Ray Diffractometer (XRD)

X-Ray diffraction was used to identify the elements and crystal structure of the synthesized TTCP powders and calcium phosphate cements. Prepared samples were transformed into very fine powder using agate mortar and pestle. XRD data (Bruker ASX, D8 ADVANCE, Berlin, Germany, Figure 2.7) was collected at 20° to 70° 2θ range [62].

Figure 2.7. The X-Ray Diffractometer D8 ADVANCE [65].

2.3.4. The Scanning Electron Microscope and Energy Dispersive X-Ray Spectroscopy

Surface morphology and elemental analysis of the prepared calcium phosphate cements were observed by Carl Zeiss EVO 40 scanning electron microscope (Figure 2.8) (Carl Zeiss, Germany). Samples were divided into two pieces carefully not to cause any damage on the surface. Divided samples were placed on slides using double sided carbon tape and coated with gold under argon gas. SEM imaging was conducted at high vacuum at 10 kV at 150X, 500X, and 120.000X magnification.

Figure 2.8. The Carl Zeiss EVO 40 scanning electron microscope.

2.3.5. Estimation of Porosity and Pore Distribution

ImageJ, an open source program, was used for SEM image processing to estimate porosity and pore distribution of the cement samples [66]. For that purpose, using the scale of the SEM image, 500 μm, was defined in pixels, thus was used to manually measure the diameter of each pore the program toolbar (0.554 pixels/μm). The area of each pore was calculated in Excel 2010 (Microsoft Office, USA) and added to give the total pore area and percent porosity was by calculated by dividing the total pore area by image area.

2.3.6. Compression Tests

For the compression tests, 16.0 x 8.0 mm (⌀), duplicate samples were prepared. Samples were then further polished using Emery Paper Grid No. 800. Compressive strength of the specimens were determined using Instron Universal Testing Machine (Norwood, USA) with a force loading rate of 0.1 N/min and cross-head speed of 1 mm/min (Figure 2.9). Compressive strength calculations were made by dividing the fracture load of the specimens in Newtons by the cross sectional area of the specimen [67].

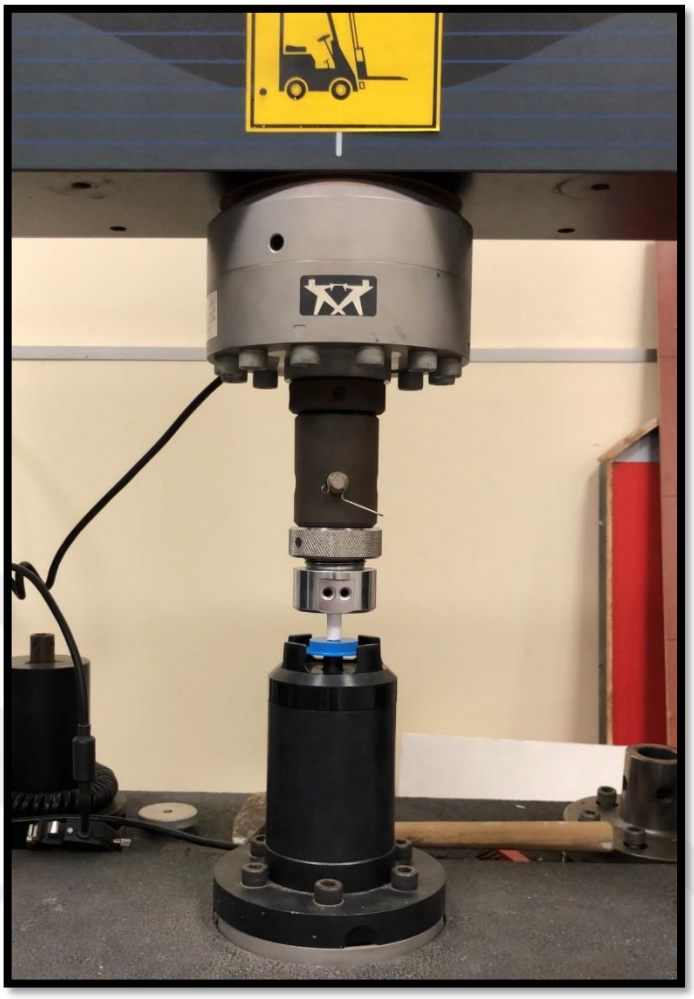

Figure 2.9. The Instron Universal Testing Machine.

2.3.7. Setting Time Assesment

Setting time of a cement is the length of time required for the cement to solidify. Conventionally, Vicat apparatus is used to determine the setting time of cements (Figure 2.10). All of the samples were prepared at room temperature and for the consistency of the experiment, cement mixing time was set to 2 minutes. A 4 mm high and 8 mm inner diameter ring was placed on glass plate and prepared cements were poured into the ring. 2.5 minutes later, a standard Gillmore needle weighing 453.6 grams was vertically lowered on the surface of the cement. The Gillmore needle was dropped repeatedly at 30 second intervals until the needle failed to penetrate the cement surface. At that point, the average of the last three data points were taken as the final setting time [68]. The Vicat testing was conducted at the setting temeperature of cement as will be discussed in section 3.37.

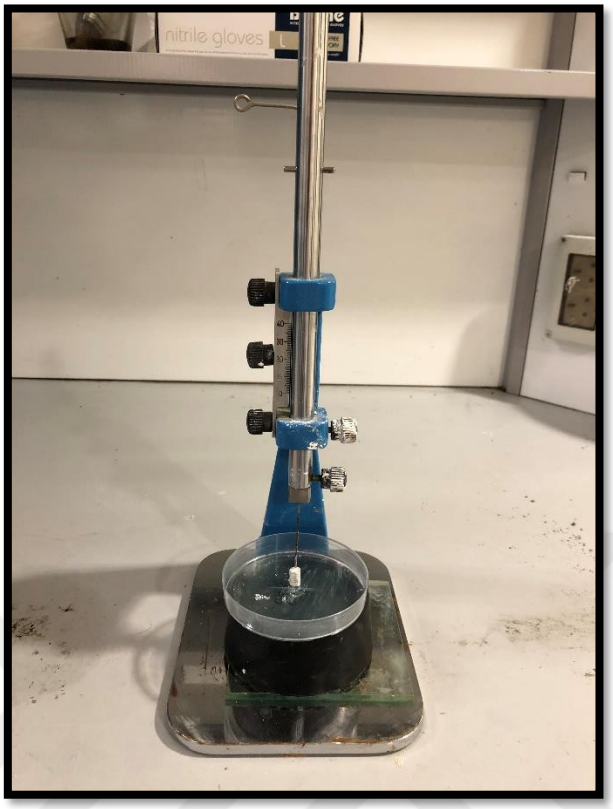

Figure 2.10. The Vicat apparatus for the setting time assesment.

2.3.8. Dissolution of Cement in Simulated Body Fluid (SBF)

Dissolution tests were conducted by determining the calcium and phosphate ion concentrations in the SBF (pH=7.4 and ion concentrations are given in section 2.1.4). 8 mm long, 4 mm diameter cylindrical samples were shaped in molds and allowed to set. After the samples were set, they were placed in falcon tubes and 50 ml. of SBF were added. Falcon tubes were placed into incubator at 37 °C and 3 ml. of SBF samples were collected at 1, 2, 7, 14 and 28 days of the incubation and replaced with an equal amount of fresh SBF solution. calcium and phosphate ion concentrations of the SBF samples were measured using flame atomic absorbance spectrometry and UV-VIS spectroscopy [69].

2.3.8.1. Flame Atomic Absorbance Spectrometry

Flame atomic absorption spectrometry is a very sensitive elemental analysis technique. A Zeenit 700 (AnalytikJena, Germany) atomic absorption spectrometer was used in this study (Figure 2.11.). Nitrus oxide acetlyene burner was used for calcium determination. Lamp was standard AnalytikJena hollow cathode lamp with instrument parameters as listed (Table 2.3).

Table 2. 3. Flame atomic absorption spectrometer parameters.

Parameters	Ca
Flame	
Fuel flow	170 l/h
Burner hight	8 mm
Burner angle	0°
Nubolizer rate	5.0 ml/min
Autosampler	
Pipetter volume	500 µl
Wash time	10 s
Spectrometer	
Wavelength	422.7 nm
Slit width	1.2 nm
HCL current	4.0 mA

Type 1 water was used as the diluent in preparing standards (Simplicity UV, France). All reagents were analytical grade. Standards were diluted from commercial 1000 mg/L stock solution (Merck). The calibration curve was plotted with standard solutions of calcium (0.25-2 mg/L). Standard solutions were prepared with 1 percent HNO_3. Measurements were conducted according to the manufacturer's application notes.

Figure 2.11. Atomic flame spectrometer.

2.3.8.2. UV-VIS Spectroscopy

Stock solution of phosphorus was prepared by dissolving 0.11 g of KH_2PO_4 in 250 ml distilled water (Stock solution A). 10 ml of stock solution A was added to 240 ml distilled water (Stock solution B). Standards were prepared using stock solution B; 0.20, 0.40, 0.60, 0.80, and 1.00 mg/L and 5, 10, 20, and 25 ml of solution B were added into separate volumetric flasks (100 ml). As a blank 50 ml distilled water was used. All solutions were filled to 50 ml using distilled water.

Combined reagent was prepared by combining 500 cm^3 of 2.5 M H_2SO_4, 50 cm^3 potassium antimony tartrate solution (i.e. prepared by dissolving 1.371 g $K(SbO)C_4H_4O_6.0.5H_2O$ in about 400 cm^3 distilled water and diluting to 500 cm^3) and 150 cm^3 ammonium molybdate solution (20 g $(NH_4)_6Mo_7O_6.4H_2O$ in 500 cm^3 of water), 300 cm^3 ascorbic acid solution (made by dissolving 5.28 g of ascorbic acid in 300 cm^3 of H_2O). 13 ml of combined reagent was added to standard 1 and shaken. Same procedure was applied to all sample solutions. Afterwards all the solutions were allowed to react for color development for 30 minutes. Before the measurement, wavelength of the UV-VIS Spectrometer (Beckmann, DU 650, Germany) was set to 880 nm then zero with distilled water in 1 cm cuvette (Figure 2.12.). Absorbance of the samples were measured (3 cycle) through the lowest concentration to highest concentration. Absorbance of the blank solution was subtracted from samples and the calibration curve was obtained [70]. The linear regression curve was used to calculate the phosphate concentration.

Figure 2.12. UV-VIS spectrometer.

2.4. ANIMAL EXPERIMENTS

In this study, animal experiments were conducted to investigate the osteoconductive and osteoinductive behavior of the calcium phosphate cement formulations on the implanted bone tissue of a living organism. Experiments of a pilot study were conducted on the 6 male 8-10 week old Sprague-Dawley rats. Rats were randomly divided into three groups as control, 4-week, and 8-week groups (Table 2.4).

Table 2.4. Animal experimental design and animal groups.

Type	Animal #	4-week	8-week	Implanted in the Left Calvarium	Implanted in the Right Calvarium
Control	1	X	-	Own tissue	Own tissue
Control	3	-	X	Own tissue	Own tissue
Sample	4	X	-	76C-5/37	80C-3/37
Sample	5	X	-	76C-5/37	80C-3/37
Sample	2	-	X	76C-5/37	58C-2/50
Sample	6	-	X	76C-5/37	80C-3/37

For each rat, two defects with a 3 mm diameter generated using drilling blades (Krowne-Meisinger, 229-030-RAL, Germany) on the right and left sides of the cranium [59].

2.4.1. Pre-operative Procedure

i. All the equipment was sterilized before the operation.
ii. Heating pad was set to 42 °C.
iii. Each rat was weighed and 80 mg/kg ketamine and 10 mg/kg xylazine were administered intraperitoneally as an anesthetic agents.
iv. Physiological response of the rat was monitored to determine the deepness of anesthesia. For that purpose, the leg of the rat was pinched while oberving its respiration rate.

v. Hair on the calvarium was shaved (Figure 2.13a) and terramycin cream was applied to eyes of the rat to prevent any damage that can occur due to anesthesia (Figure 2.13b).

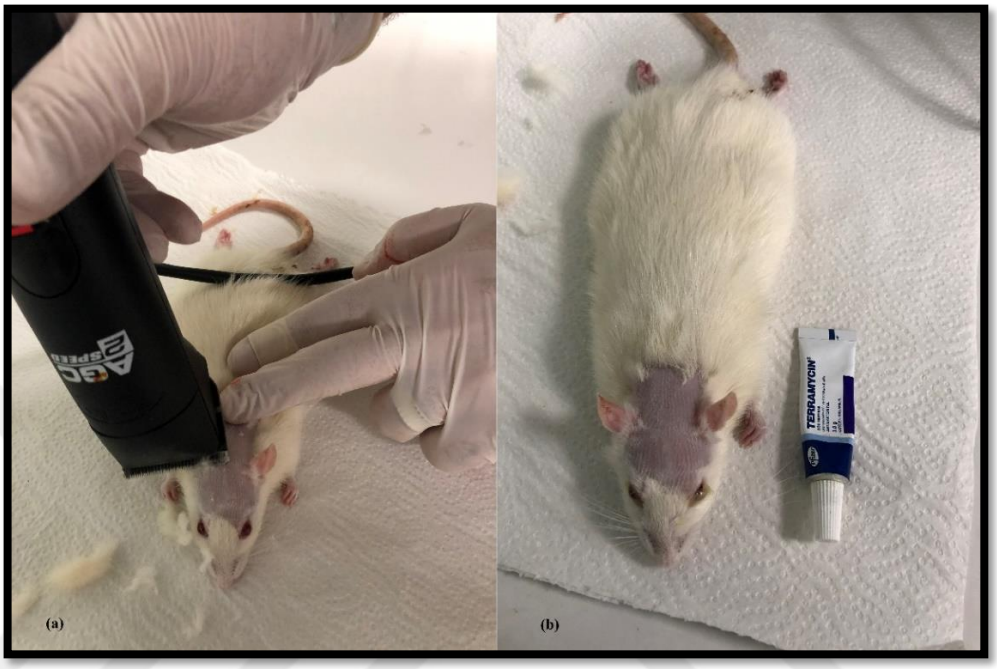

Figure 2.13. (a) Hair on the calvarium was shaved, (b) terramycin cream was applied.

2.4.2. Operation Procedure

i. Using a scalpel, an incision was made from the periosteum to snout bridge by following the middle sagittal crest.
ii. Periosteum was revealed by pinning the skin layer with a hook on both left and right sides (Figure 2.14a).
iii. Periosteum was removed carefully using scalpel to reveal cranium.
iv. 3 mm defect was carefully created on the right side of the cranium with using drill and sterile saline was applied during the process to prevent any thermal damage on the defect tissue (Figure 2.14b).
v. The defect was displaced with a help of scalpel (Figure 2.14c).
vi. After that, 3 mm defect was gently created on the left side with following same procedure at step iv.

vii. The defect was removed and two different calcium phosphate cements were implanted in both defects (Figure 2.14d).

viii. Afterall, skin layer was sutured to close the periosteum (Figure 2.14e).

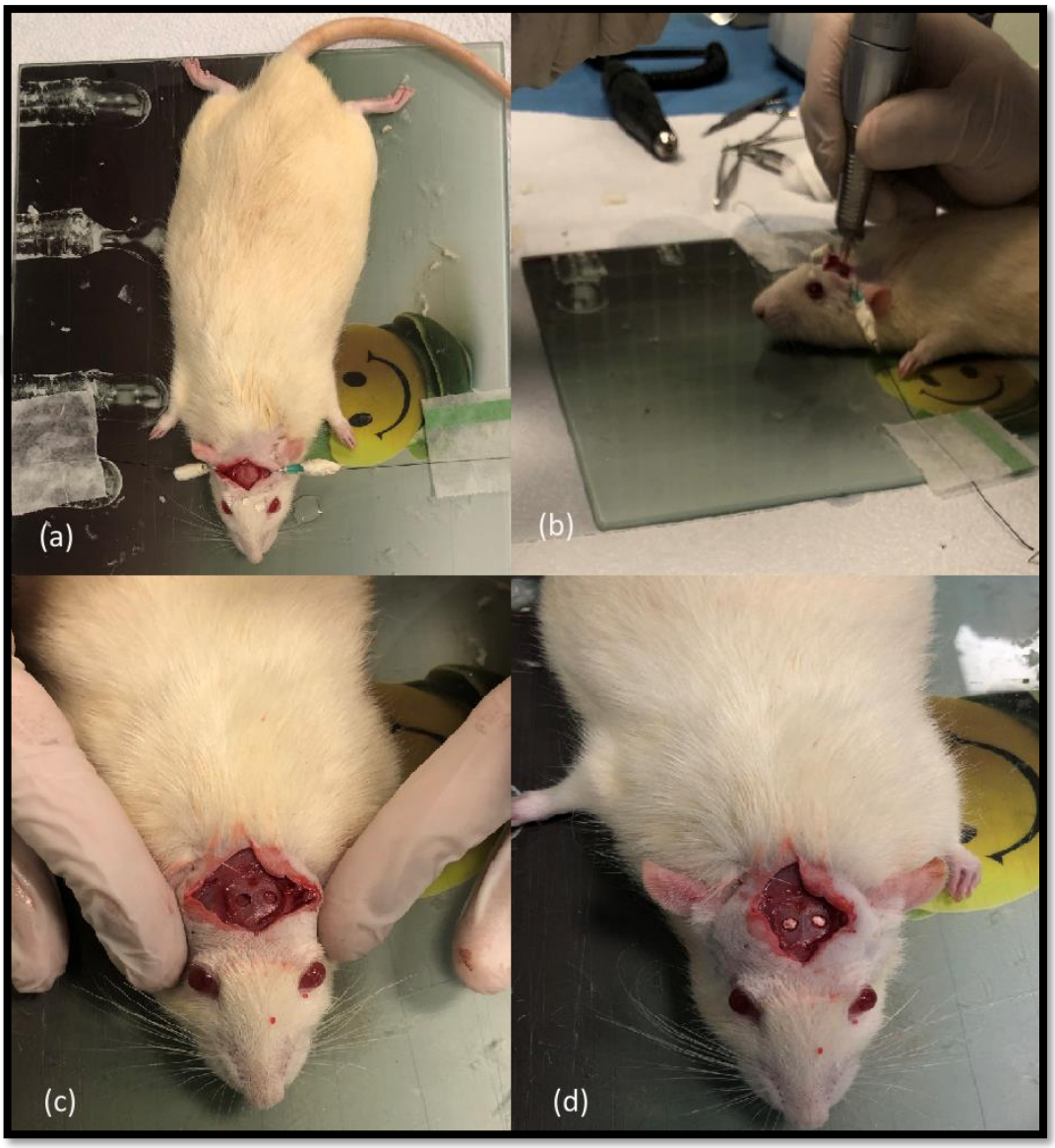

Figure 2.14. (a) Skin layer was detached and periosteum revealed, (b) 3 mm defect was created using drill, (c) defects were created and removed using scalpel, (d) calcium phosphate cements were implanted, (e) skin layer was sutured, (f) cranium was completely closed and surgery was succesfully completed..

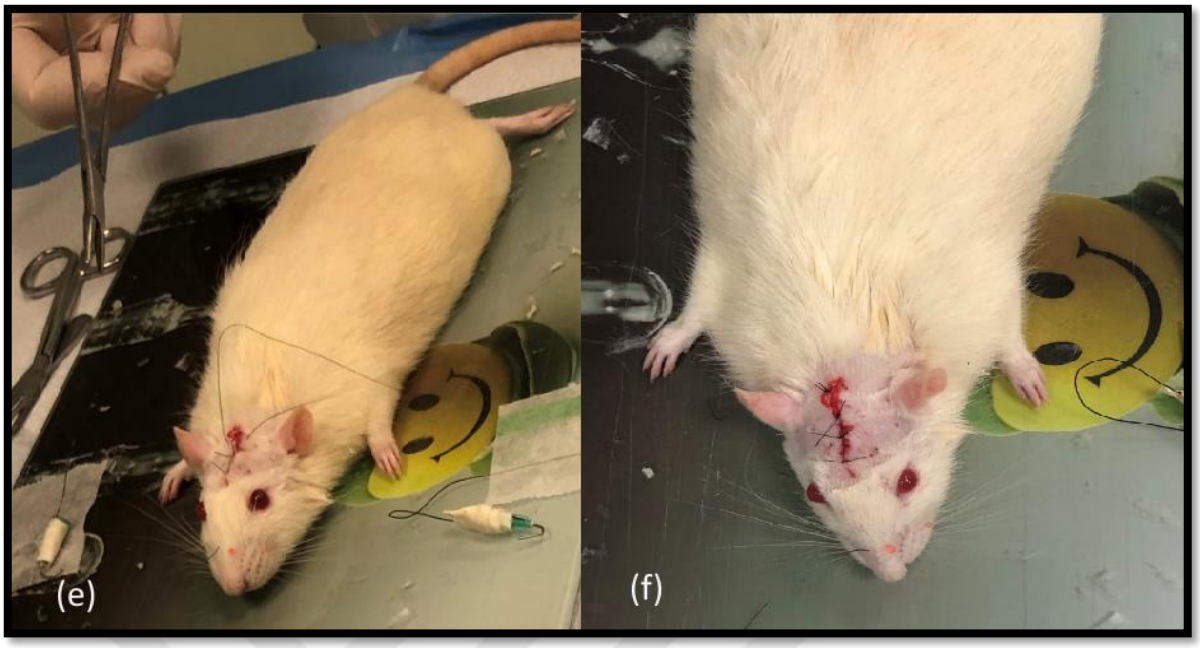

Figure 2.14. (continue'd).

2.4.3. Post-operative Procedure

i. After the surgery, rats were placed on heating pad to maintain their body temperature (Figure 2.15).
ii. Tails of the rats were labelled for identification purposes.
iii. Isotonic water (5 cc) was given to ease effect of anesthesia.
iv. To prevent dryness in the eyes due to anesthesia, terramycin cream was applied.
v. Physiological response of the rats were observed and rats were transferred into cages.
vi. Rats were monitored and relabelled every 3 day.

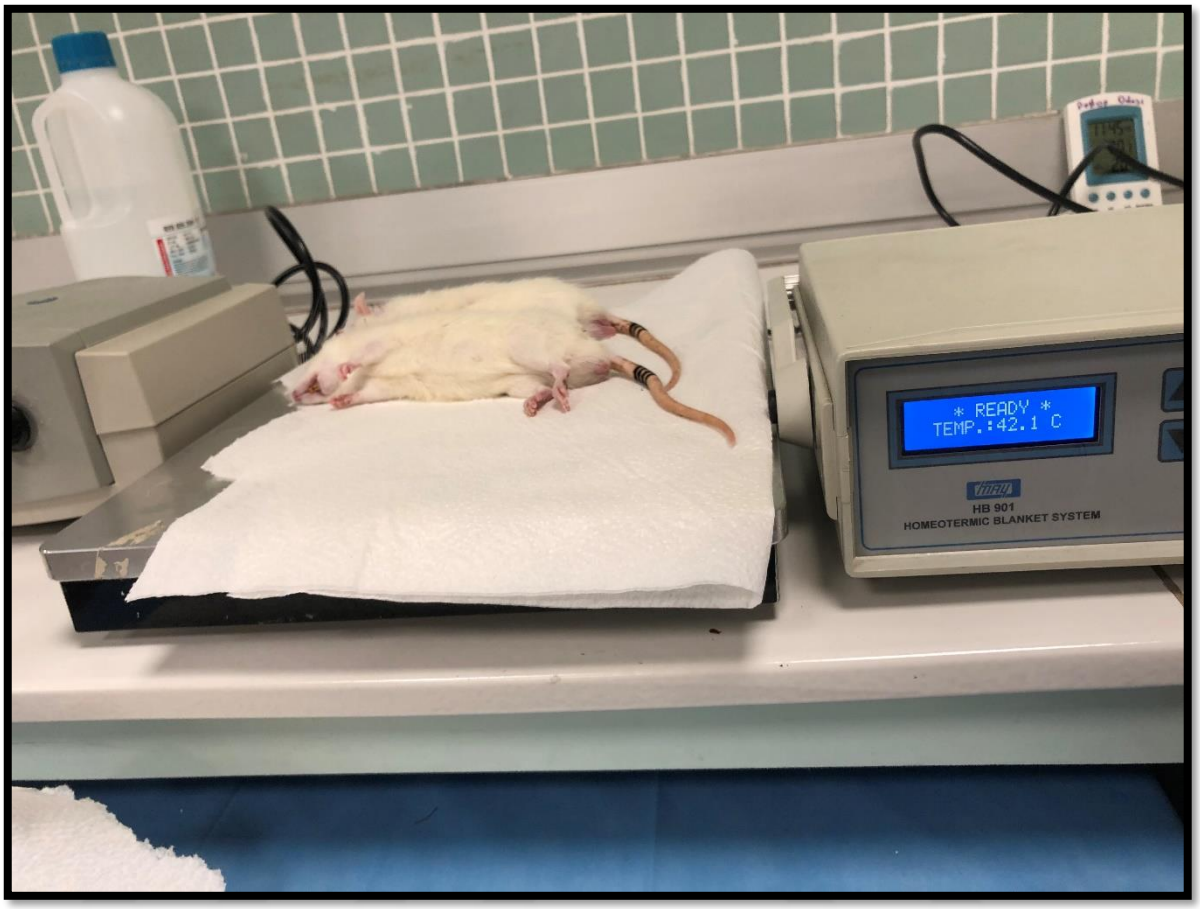

Figure 2.15. The rats were placed on the heating pad and labelled.

2.4.4. Implant Harvest and Euthanasia

Euthanasia was performed by CO_2 respiration and implanted tissue was harvested using bone scissors and immediately placed into 10 percent formalin solution and stored at room temperature (at 25 °C).

2.4.5. Histological Assesment

2.4.5.1. Histological Preparation

The histomorphometric preparation and analysis were conducted under the supervision of Prof Dr. Ferda Ozkan at the Yeditepe University Hospital Pathology Laboratory. Tissue samples were placed in formic acid decalcifier (Shandon TBD-2) for 10 to 20 hours, which depends on the sample and samples were controlled during the process to prevent any

damage. Subsequently to decalcification process, samples were taken out and washed with distilled water. Tissues were placed in casettes and macroscopic of the samples were taken. Afterwards, the tissues were placed in tissue processor and processed as given in below.

- Tissue was soaked in buffered formaldehyde for 2 hours,
- Tissue was soaked in 70 percent ethanol for 40 minutes, in 80 percent ethanol for 45 minutes, in 96 percent ethanol for 50 minutes and in 100 percent ethanol consecutively three times for 1 hour periods,
- Tissue was soaked in xylene consecutively for 40 minutes, for 45 minutes and for 50 minutes,
- Tissue was soaked in paraffin consecutively three times for 1 hour.

Afterwards, processed tissue samples were placed in base molds and hot paraffin were poured onto tissue and tissue let cool in room temperature. Cooled paraffin blocks placed in -18 °C for further cooling process. Frozen tissue samples were cut with a 3 micron thickness and were placed in oven at 75 °C to melt down paraffin therefore prepared samples were then ready for the hematoxylin-eosin (H&E) staining technique, as given below:

- Samples were soaked twice in xylene for 4 minutes each,
- Samples were soaked consecutively in 96 percent ethanol three times for 1 minute each
- Samples were washed with distilled water for 30 seconds
- Samples were soaked in hematoxylin stain for 30 seconds
- Stained samples were washed with distilled water until the hematoxylin washed out
- Samples were soaked in 96 percent ethanol for 30 seconds
- Samples were soaked in eosin stain for 6 minutes
- Samples were soaked twice in 96 percent ethanol for 30 seconds
- Samples were soaked in acetone for 10 seconds

- After the soaking with acetone slides were let to dry
- Dried slides were closed with the Shandon Consul-Mount coverslipper.

2.4.5.2. The Scoring Method

The scoring method used was a modified Lane and Sandhu method developed by Han et al. [71], identifying and measuring the amount of newly formed osteonal and cartilaginous and fibrous tissue as well as the remaining defect. The newly formed bone was determined on the basis of hard callus formation, the newly formed cartilage was indicated by soft callus formation and the newly formed fibrous tissue occuring during the soft callus phase. The remaining defect size is the area of nonhealed area. These parameters were normalized to form a percentage (%). The minimum and maximum scores for each parameter were added to give a final score ranging from 0 to 40 as listed in Table 2.5. Higher ossification meant higher scores, while lower scores indicated a higher amount of remaining defect.

Table 2.5. Histological scoring method

Newly formed bone	**Score**
No evidence of newly formed bone	0
≤10 % of the original bone defect	1
≤20 % of the original bone defect	2
≤30 % of the original bone defect	3
≤40 % of the original bone defect	4
≤50 % of the original bone defect	5
≤60 % of the original bone defect	6
≤70 % of the original bone defect	7
≤80 % of the original bone defect	8
≤90 % of the original bone defect	9
≤100 % of the original bone defect	10
Newly formed cartilage	
No evidence of hypertrophic cartilage	0
≤10 % of the remnant defect	1
≤20 % of the remnant defect	2
≤30 % of the remnant defect	3
≤40 % of the remnant defect	4
≤50 % of the remnant defect	5
≤60 % of the remnant defect	6
≤70 % of the remnant defect	7
≤80 % of the remnant defect	8
≤90 % of the remnant defect	9
≤100 % of the remnant defect	10
Newly formed fibrous tissue	
Full healing	10
≤10 % of the remnant defect	9
≤20 % of the remnant defect	8
≤30 % of the remnant defect	7
≤40 % of the remnant defect	6

Table 2.5.(Continue'd) Histological scoring method

≤50 % of the remnant defect	5
≤60 % of the remnant defect	4
≤70 % of the remnant defect	3
≤80 % of the remnant defect	2
≤90 % of the remnant defect	1
≤100 % of the remnant defect	0
Remnant defect size	
Full healing	10
≤10 % of the original defect size	9
≤20 % of the original defect size	8
≤30 % of the original defect size	7
≤40 % of the original defect size	6
≤50 % of the original defect size	5
≤60 % of the original defect size	4
≤70 % of the original defect size	3
≤80 % of the original defect size	2
≤90 % of the original defect size	1
≤100 % of the original defect size	0

3. RESULTS AND DISCUSSION

In the first part of this section, the FT-IR spectroscopy and X-Ray Diffraction results of the synthesized TTCP powder will be discussed. In the second part, the results of the numerous formulations generated to attain the most appropriate calcium phosphate cement will be discussed.

3.1. CHARACTERIZATION OF TTCP

3.1.1. TTCP Formation Reaction

TTCP has the highest Ca/P ratio and solubility among all the calcium phosphates. There are several methods for the synthesis of TTCP, conventionally produced by a solid-state reaction between calcium carbonate ($CaCO_3$) and dicalcium phosphate anyhdrous ($CaHPO_4$). This reaction requires high heating temperatures like 1450-1500 °C for 12 hours and has to be quenched at room temperature subsequent to the heating process. Rapid cooling of TTCP is essential in order to preserve purity of the synthesized TTCP. Furthermore, slower cooling will cause decomposition of TTCP to undesired by-products like HA, CaO, and $CaCO_3$ [72].

In this study, TTCP is sythesized following the method that was developed by Jalota et al. [62]. In the guidance of the procedure, 1:2 stochiometric mol ratio of ammonium dihydrogen phosphate and calcium diacetate monohydrate was used according to reaction given in Figure 3.1.

Ammonium dihydrogen phosphate melts around 190 °C (Figure 3.1 (2)) and decomposes to an acidic phosphate liquid which also immediately reacts with calcium diacetaate monohydrate and forms calcium acetate anhydrous (Figure 3.1 (1)). These two reactions take place when the temperature reaches 200 °C.

Following these reactions, calcium acetate anhydrous decomposes at 400 °C and forms calcium carbonate as a final product with a by-product as acetone, which is evaporated during the reaction (Figure 3.1 (3a)).

When the temperature reaches 790-800 °C calcium carbonate transforms completely to calcium oxide and carbon dioxide gas is released to the environment as a second by-product (Figure 3.1 (3b)). Decomposition reaction of calcium acetate can be finalized as seen in Figure 3.1 (3c), With a further temperature increase to 800 °C, ammonia evaporates from the environment and leaves the phosphorus pentoxide as a final product (Figure 3.1 (4)). As a final step of the reaction calcium oxide and phosphorus pentoxide reacts to synthesize TTCP as the final product (Figure 3.1 (5)).

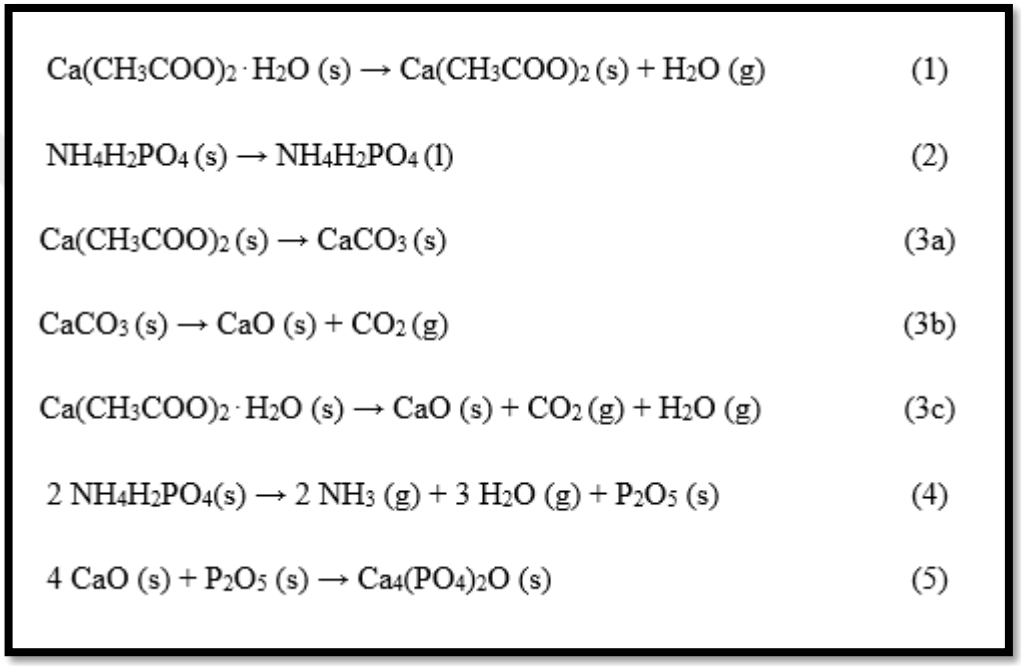

Figure 3.1. TTCP forming reactions.

3.1.2. FT-IR and XRD Spectra of Hydroxyapatite

3.1.2.1. FT-IR Spectroscopic Analysis of TTCP

The FT-IR spectroscopy results of the synthesized TTCP powder (Figure 3.2) correlated with the results reported in the literature (Figure 3.3) [62]. The characteristic peaks of the TTCP are expected at 454 cm^{-1}, 470 cm−1, 501 cm−1, 570 cm−1, 593 cm−1, 601 cm−1, 621 cm−1, and 930–1100 cm−1. In the spectra, the PO_4^{3-} group vibrations were visible in the 1105-989 cm^{-1} range for ν_3, 962-941 cm^{-1} for ν_1 and 620-571 cm^{-1} for ν_4. Additionally, the distinctive OH^- peak at 3640 cm^{-1}, calcium hydroxyde related O-H streching vibration of O-

H group was also present [62]. Adsorption of water by CaO was formed $Ca(OH)_2$ and 3644 cm^{-1} was visible for that group [73].

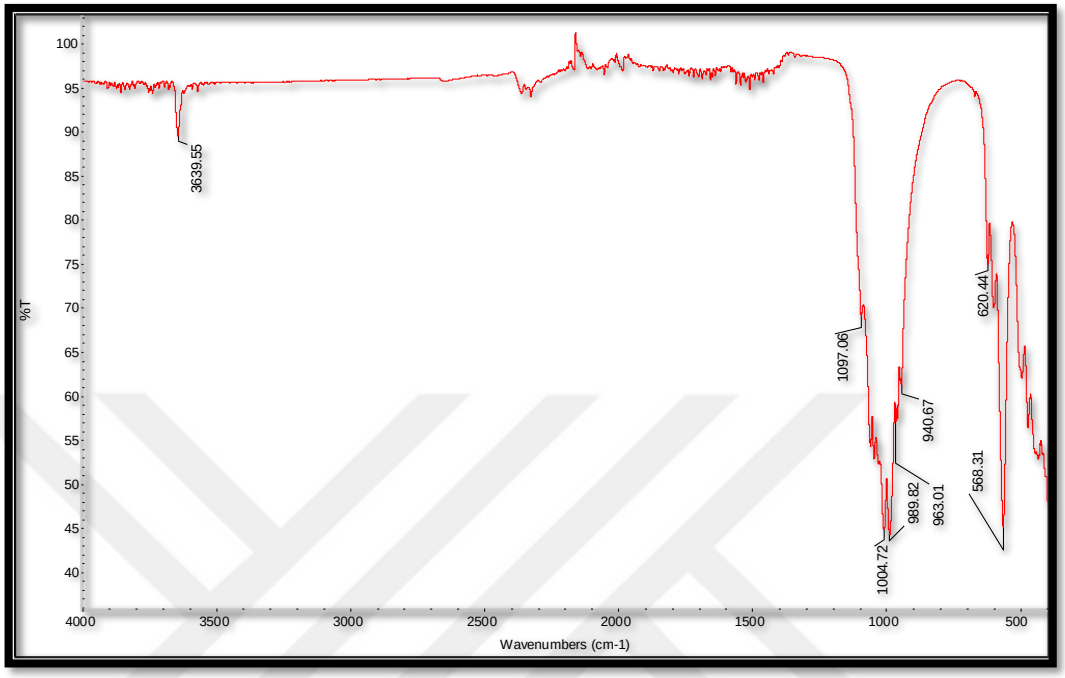

Figure 3.2. The FT-IR spectrum of the synthesized TTCP powder.

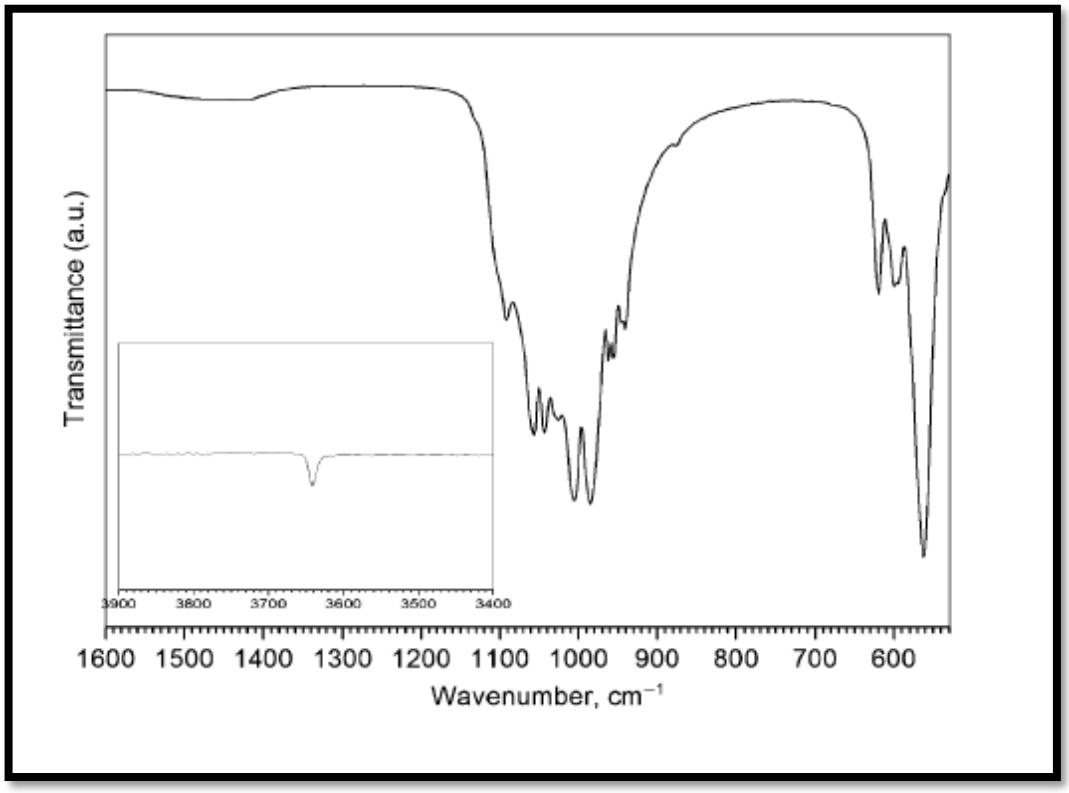

Figure 3.3. The FT-IR spectrum of TTCP powder synthesized by Jalota et al. [62].

3.1.2.2. X-Ray Diffraction Analysis of TTCP

The crystal structure of the synthesized TTCP powders and cements were determined using the XRD. The XRD spectrum results of Jalota et al. [62] (Figure 3.4) were compared with the XRD spectrum of the synthesized TTCP powder (Figure 3.5). The characteristic TTCP peaks were at 2θ angles of 21.8° (121), 25.4° (200), 25.7° (130), 28.0° (211), 28.3° (211), 29.3° (032), 29.8° (040), the 100 percent peak at 30.9° (−103), 31.2° (221), 31.9° (−132), 32.1° (113), 32.4° (−212), and 32.9° (212), which agreed with the JCPDS pattern number 25-1137 of TTCP as well as the CaO peaks at 34.17° 2θ and the $Ca(OH)_2$ peak at 37.6° 2θ [62].

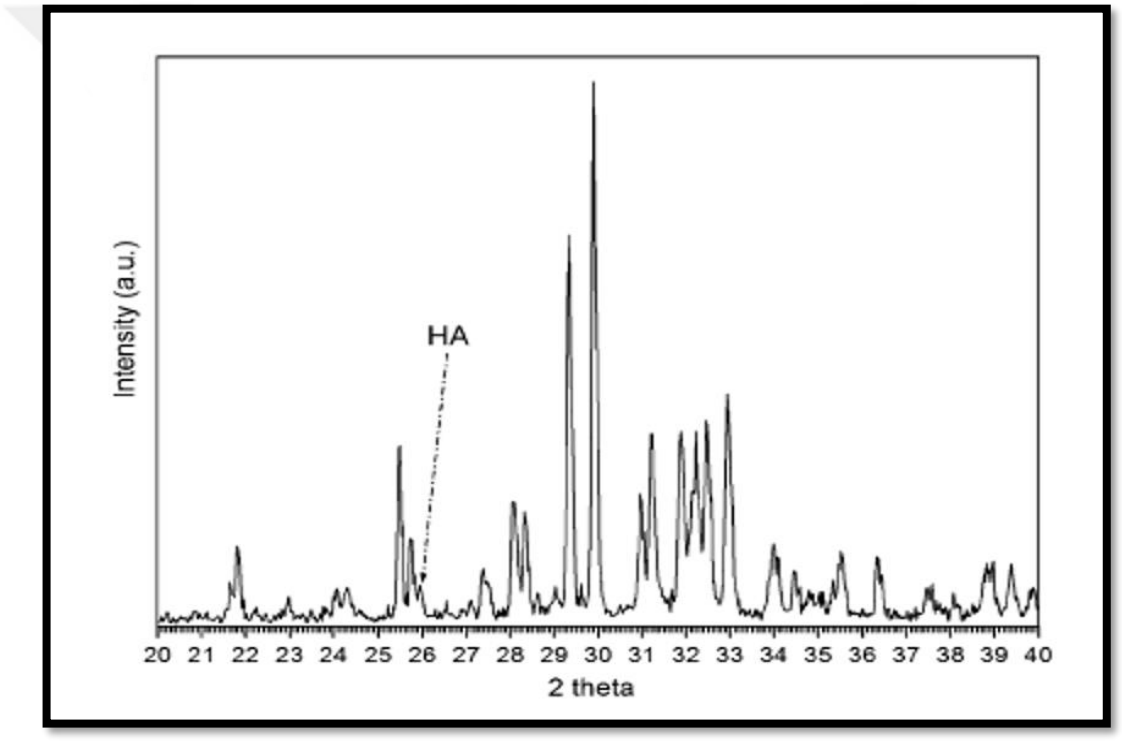

Figure 3.4. The XRD spectroscopy of TTCP powder synthesized by Jalota et al. [62].

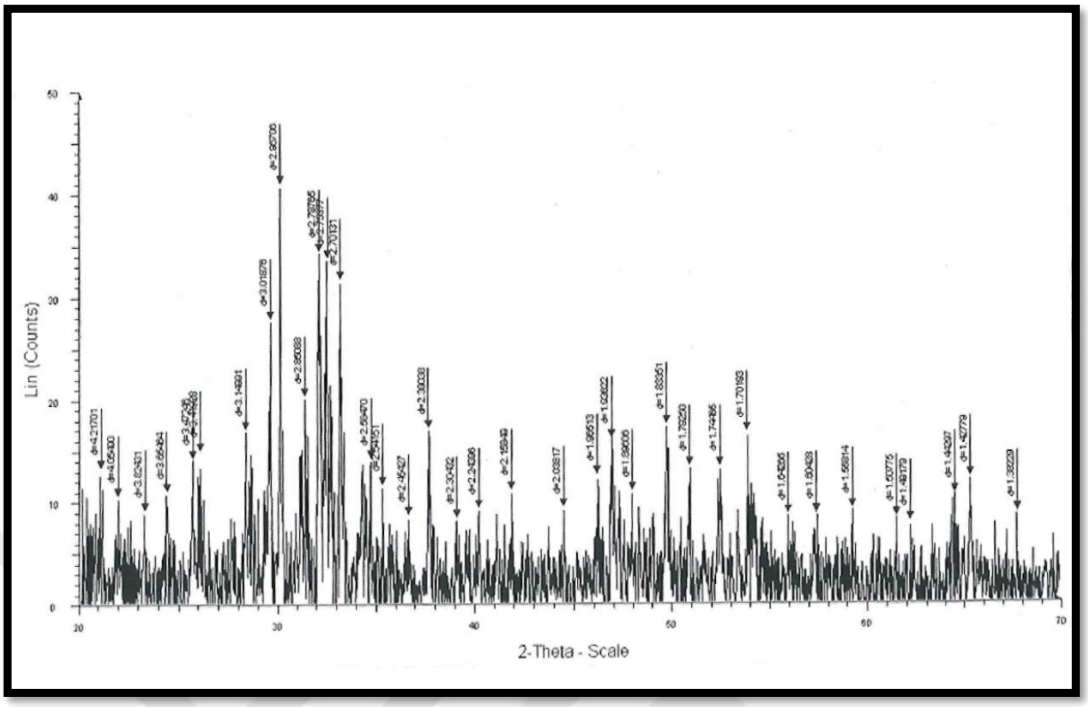

Figure 3.5. The XRD spectroscopy of the synthesized TTCP powder.

3.1.2.3. Scaning Electron Microscopy of TTCP

Particle morphology of the TTCP powders are given in Figure 3.6.(a) and (b). Synthesized powders demonstrated micro structures smaller than the 2µm indicating that vapor-and-liquid phase reactions have taken place [Ref jalota]. The SEM images of the TTCP particles of about 50µm could be observed.

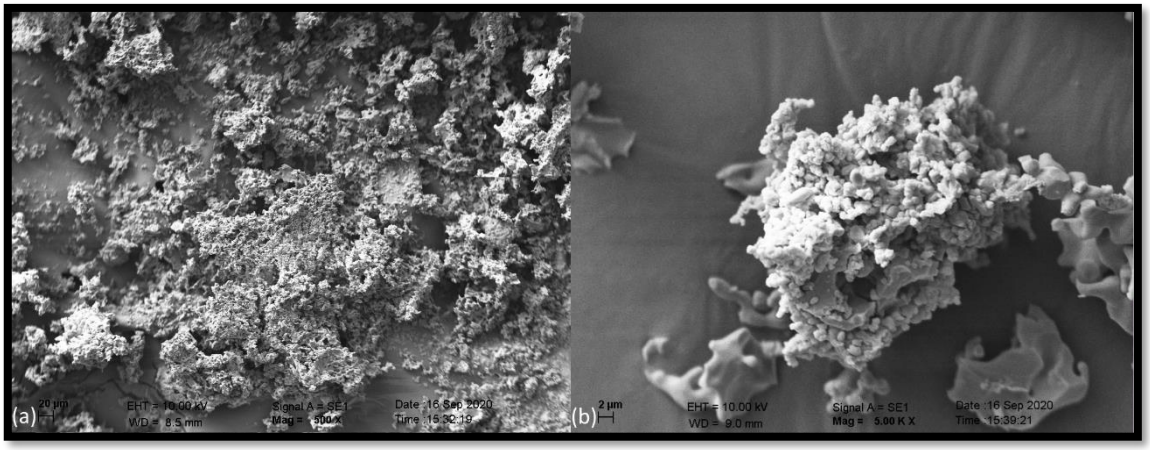

Figure 3.6. The SEM images of TTCP powders at (a) 500X, (b) 5000X magnification.

3.1.3. FTIR Spectroscopy of Silk Fibroin

According to FTIR spectrum of the silk-fibroin indicated Amide A peaks at the region of 3296 cm^{-1}, and Amide I, II, and III peaks were visible at the regions of 1630, 1516, and 1231 cm^{-1} respectively (Figure 3.7.).

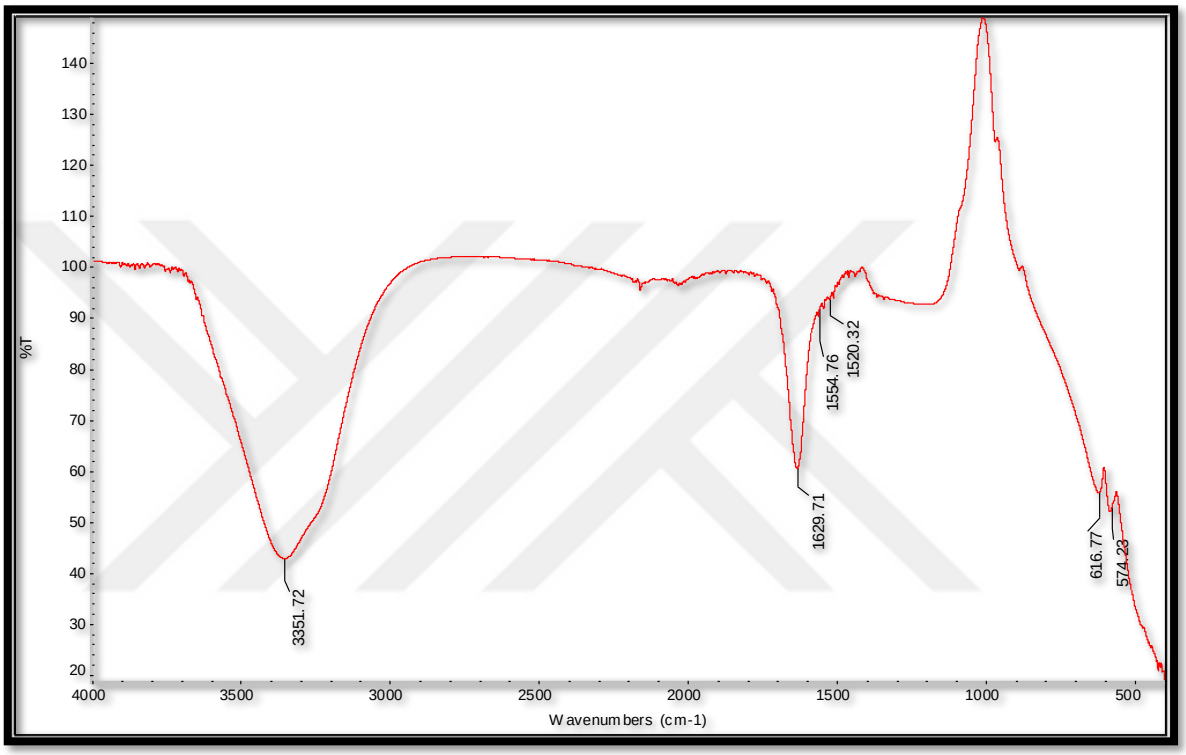

Figure 3.7. FTIR spectrum of silk-fibroin protein.

XRD peaks of the silk-fibroin are visible at the 2θ angles of 12.2°, 19.7°, 24.7°, 28.2° for silk I, and 9.1°, 18.9°, and 20.7° for silk II (Figure 3.8.) [74].

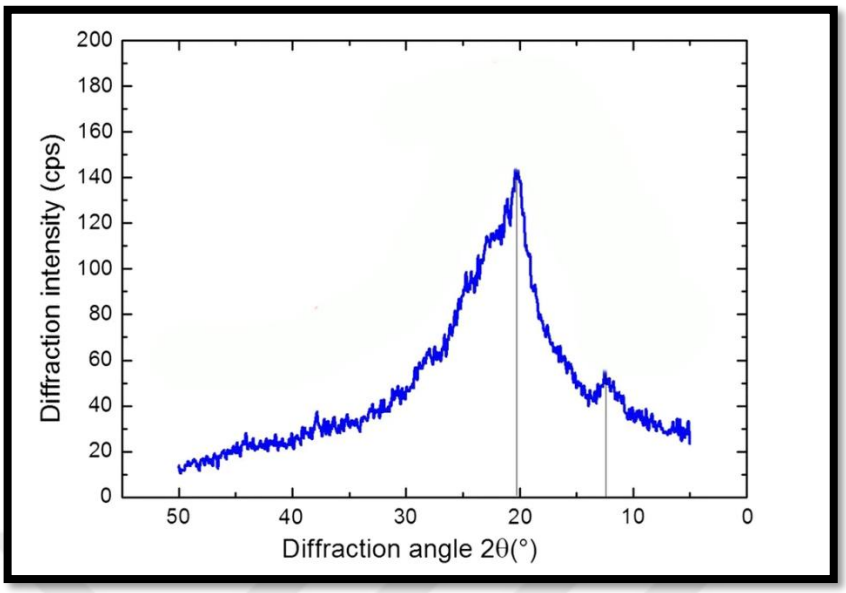

Figure 3.8. XRD spectrum of silk-fibroin protein [19].

3.2. HYDROXYAPATITE FORMING REACTIONS

HA is formed as a result of acid-base reaction between weak base TTCP and weak acid DCPA/DCPD. Equimolar reaction of TTCP and DCPA or DCPD forms stoichiometric HA (Figure 3.9 (a) and (b)) [54]. Additionally, reaction of 1 mole TTCP and 2 moles of DCPA yields calcium deficient HA with a Ca/P ratio of 1.5 (Figure 3.9 (c)) [54].

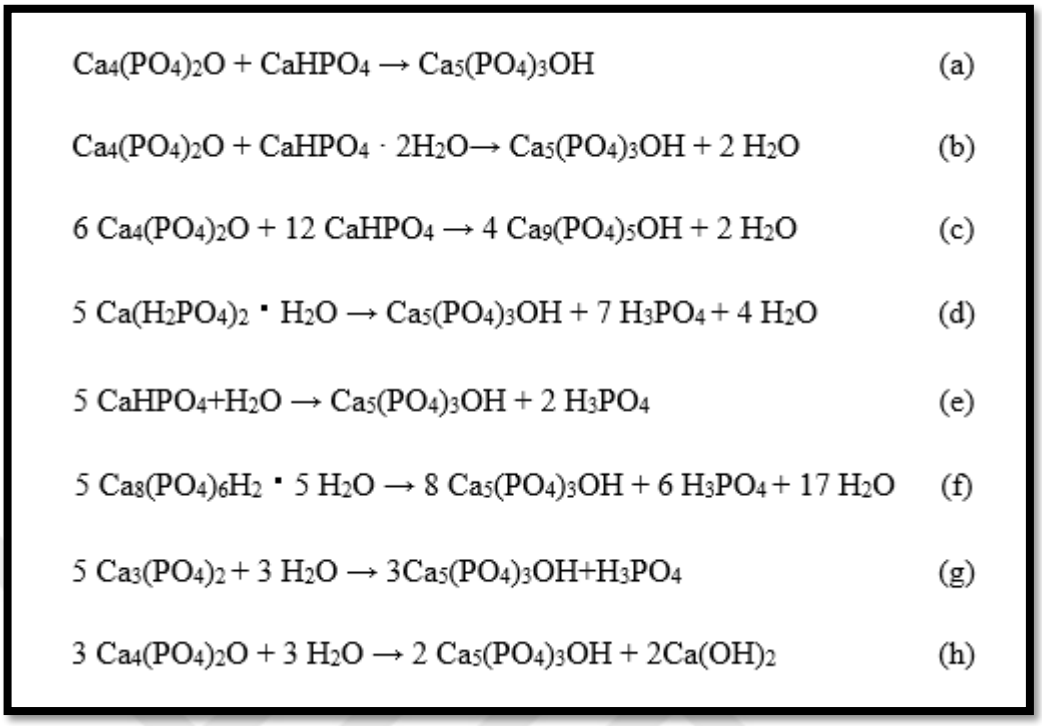

Figure 3.9. Hydroxyapatite and calcium deficient hydroxyapatite formation reaction with TTCP, DCPA, and DCPD. (a) 1:1 molar ratio of TTCP and DCPA (b) 1:1 molar ratio of TTCP and DCPD (c) 1:2 molar ratio of TTCP and DCPA [54], (d) from MCPM, (e) from the hydrolysis of DCPA, (f) from OCP pentahydrate, (g) from the hydrolysis of TCP, and (h) from the hydrolysis of TTCP.

In the reactions given above, in addition to HA, phosphoric acid can also be the product of the reaction formed by the dissolution of various Ca-P compounds. However, TTCP hydrolysis produces $Ca(OH)_2$ as a by product (Figure 3.9. (h)), increasing the pH and causing the solution to become less supersaturated with respect to HA (thus, formation of HA), where either the reaction rate or HA supersaturation may diminish at higher pH values [68, 82].

TTCP, with a Ca/P ratio greater than that of HA, can be reacted with calcium phosphate salts with lower Ca/P ratios, where the reaction will not release acidic or basic by products (Figure 3.9. a-c). The TTCP+DCPA and TTCP+DCPD systems have the advantage of completion in 4 hours at a near-constant rate, following zero order reaction kinetics, at near physiological pH contributing to high biocompatibility. The reaction rate could also be related to the surface area of DCPA or TTCP, the diffusion rate of calcium and phosphate ions and the distances over which these ions must migrate [68, 82].

In this study, HA seed was used as a nucleation center and a setting accelerator, as given in the literature because it leads to HA transformation at 40 wt. percent from a 1:1 molar ratio of TTCP and DCPA, and CDHA, $Ca_9(HPO_4)(PO_4)_5OH$, at a 1:2 molar ratio [68, 82].

3.3. CHARACTERIZATION AND EVALUATION OF CALCIUM PHOSPHATE CEMENTS

The gelatin and silk-fibroin protein containing calcium phosphate cements were aimed for use in non-load bearing operations, i.e. as (a) implant support structures and (b) skull bone replacements. As implant support structures, the gelatin and silk-fibroin calcium phosphate cements were variably tested as formulations that contain different gelatin concentrations, powder to liquid ratios and calcium or natrium carbonate salts. As cranial bone replacements, the gelatin and silk-fibroin calcium phosphate cements were prepared at different setting temperatures, with the idea that they could be shaped as implants that are fitted to the implantation site. The cements were prepared, characterized, compared in groups. The results were assessed in order to choose the formulations to be implanted and *in-vivo* tested. In the following sections of this thesis, these procedures and assessments will be discussed.

Several aspects were considered to formulate the final product with the appropriate setting time, setting temperature, carbonate type and the organic/inorganic content as given below.

- To formulate with the adequate amount of organic content (silk-fibroin protein and gelatin).
- To choose the appropriate powder to liquid ratio for the organic content.
- To choose the appropriate setting temperature.
- To formulate with either/or or both calcium and natrium carbonate salts.

The cements were formulated. characterized and compared as listed in Table 3.1. The cements were named to indicate gelatin content (wt. percent) and setting temperature (°C). As an example, 80C-3/37, means that cement 80 has 3 wt. percent gelatin and is set at 37 °C. NaH and NaL indicate presence of natrium cation, NCH and NCL indicate presence of natrium and calcium cations along with the higher and lower water content respectively.

Table 3.1. The calcium phosphate cement formulations and nomenclature.

	A	B	C	D	E	F
Cement No	**0G**	**2Na**	**3Ca**	**3NA/Ca**	**3Na**	**5Ca**
TTCP (g)	0.673	0,.673	0.673	0.673	0.673	0.673
DCPD (g)	0.316	0	0.632	0.632	0.632	0.632
DCPA (g)	0	0.5	0	0	0	0
HA (g)	0.105	0.105	0.105	0.105	0.105	0.105
$CaCO_3$ (g)	0	0	0.105	0.0525		0.105
Na_2CO_3 (g)	0	0.105	0	0.0525	0.105	0
Gelatin (g)	0	0.027	0.0428	0.0428	0.0428	0.072
1M Na_2HPO_4 (µL)	0	433	433	433	433	433
0.5M Na_2HPO_4 (µL)	494	0	0	0	0	0
dH_2O (µL)	0	30	280	402 // 280	402 // 280	280
Silk Sol (µL)	0	124	124	124	124	124
25 °C			**79C-3/25**			**75C-5/25**
37 °C			**80C-3/37**			**76C-5/37**
50 °C	**85C-0/50**	**58C-2/50**		**83C3/50NCH //84C3/50NCL**	**81C3/50NaH //82C3/50NaL**	**73C-5/50**
65 °C						**69C-5/65**
80 °C						**70C-5/37**

3.3.1. FT-IR Spectroscopy Analysis

3.3.1.1. FT-IR Spectroscopy and XRD Analysis

As the calcium phosphate cements were expected to transform into hydroxyapatite, the FT-IR and XRD spectra of the CPC formulations were expected to display the characteristic hydroxyapatite peaks. PO_4^{3-} ion has vibrations of ν_1, ν_2, ν_3, ν_4. ν_1 is the vibration of P-O symmetric motion, and the bending vibrations are called ν_2. ν_3 corresponds to the

wavenumber of asymmetric vibrations and ν_4 represents the wavenumber of O-P-O asymmetric bending. The characteristic hydroxyapatite FT-IR spectrum (Figure 3.10) displays peaks consisting of the PO_4^{3-} group in the region of 560, 602, 961 cm^{-1}, and 976–1190 cm^{-1}. In HA, the peaks at 603 and 567 cm^{-1} represent the PO_4^{3-} group vibrations, which is asymetric bending, ν_4. Addtionally, 1037 and 1092 cm^{-1} indicates asymmetric streching ν_3 of PO_4^{3-} group. ν_1 symmetry strecthing vibration of PO_4^{3-} group is avaible at 962 cm^{-1}. The hydroxide peaks at 634 cm-1 for –OH libration and at 3570 cm-1 for –OH stretch are diplayed with a sharp OH^- peak at 3570 cm^{-1} along the –OH stretch at 3200–3400 cm^{-1}. The CO_3^{2-} group is displayed as weak peaks at 880-870 cm^{-1} indicating presence of carbonate groups in the lattice of phosphate ions, and at 1419 and 1454 cm^{-1}, indicating presence of surface carbonate ions interacting with water in the compound, an additional peak appearing at 1654 cm^{-1} for water bending vibration and intense peaks at 1530-1460 cm^{-1} (Figure 3.10). Water that adsorbed on the surface has bending vibration at 1637 cm^{-1} and strecthing vibration at 3431 cm^{-1}. Carbonate substitution for hydroxide as well as the inclusion of a bivalent ion results in a decrease in ionic content, formation of Ca^{+2} or OH^- vacancy due to a charge compensation mechanism and a consequent reduction in the intensity of the hydroxide peak in the spectrum [75]. The CO_3^{2-} group has antisymmetric vibration at 857 cm^{-1} and out-of-plane bending at 1481 cm^{-1} [73]

Table 3.2. The XRD peaks of HA [76].

h	k	*l*	Degrees 2θ	Peak intensity (%)
0	0	2	25.879	40
2	1	1	31.773	100
1	1	2	32.196	60
3	0	0	32.902	60
2	0	2	34.048	25
3	1	0	39.818	20
2	2	2	46.711	30
2	1	3	49.468	40
3	2	1	50.493	20
0	0	4	53.143	20

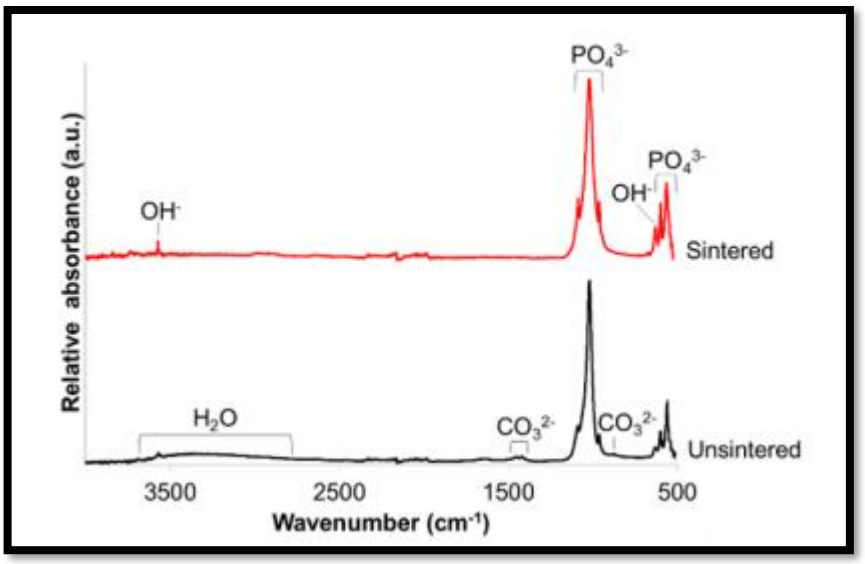

Figure 3.10. The FTIR spectrum of HA [77].

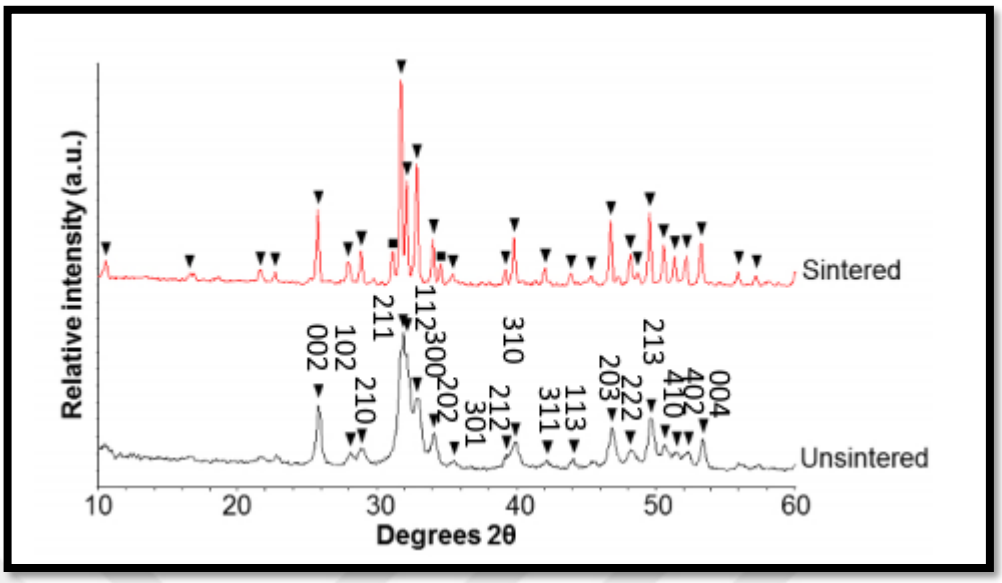

Figure 3.11. The standard XRD peaks of HA [77].

3.3.2. The Chemical Formulation of the CPC

3.3.2.1. The Inorganic Content

The cement consisting of only the inorganic component without carbonate was used as the basic cement formulation. The reactants producing 85C-0/50 were TTCP and DCPD mixed with Na_2HPO_4 (0.5M) at sT of 50 °C to give the final product with a Ca/P ratio of 2.88 and a contact angle of 8.00°±0.01. The FT-IR spectrum (Figure 3.12.) displays the characteristic phosphate peaks, with a broad O-H stretch of low intensity. The XRD spectrum (Figure 3.13.) displayed the typical HA peaks in the 31°-34° 2θ range. The SEM image of 85C-0/50 (Figure 3.14) displayed nanorod shaped crystals of sizes less than 100 nm coated with the organic content.

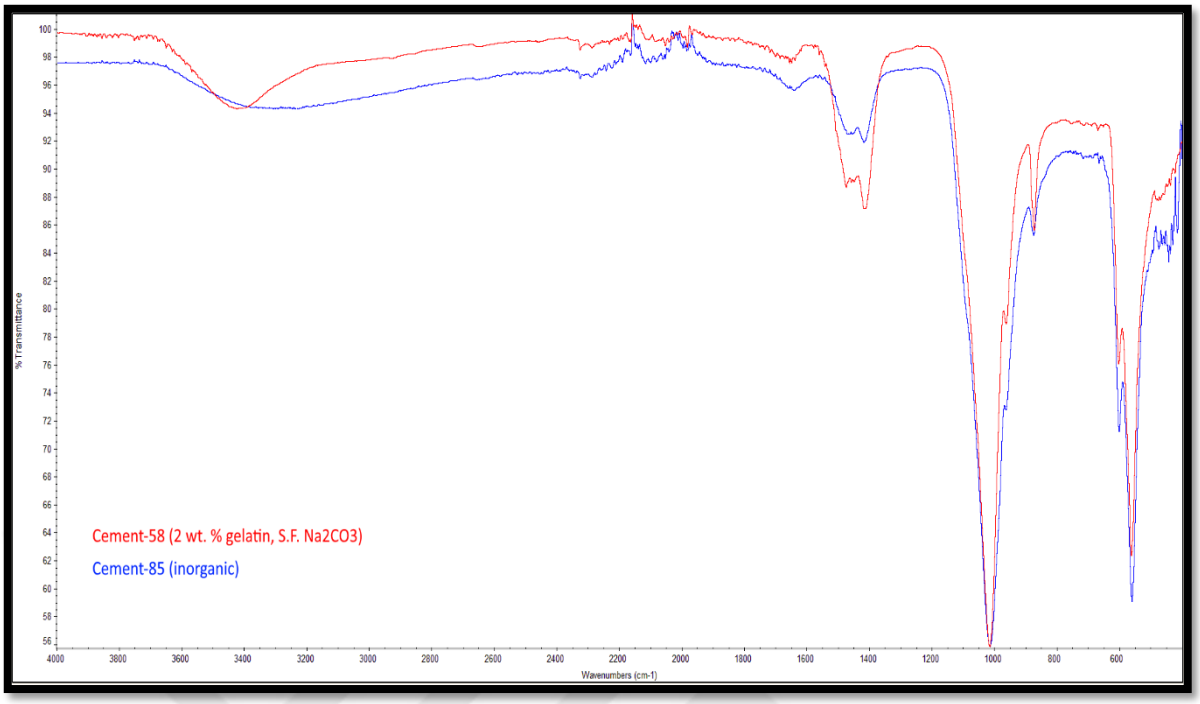

Figure 3.12. The FT-IR spectra of 58C-2/50 (containing Na_2CO_3) and 85C-0/50.

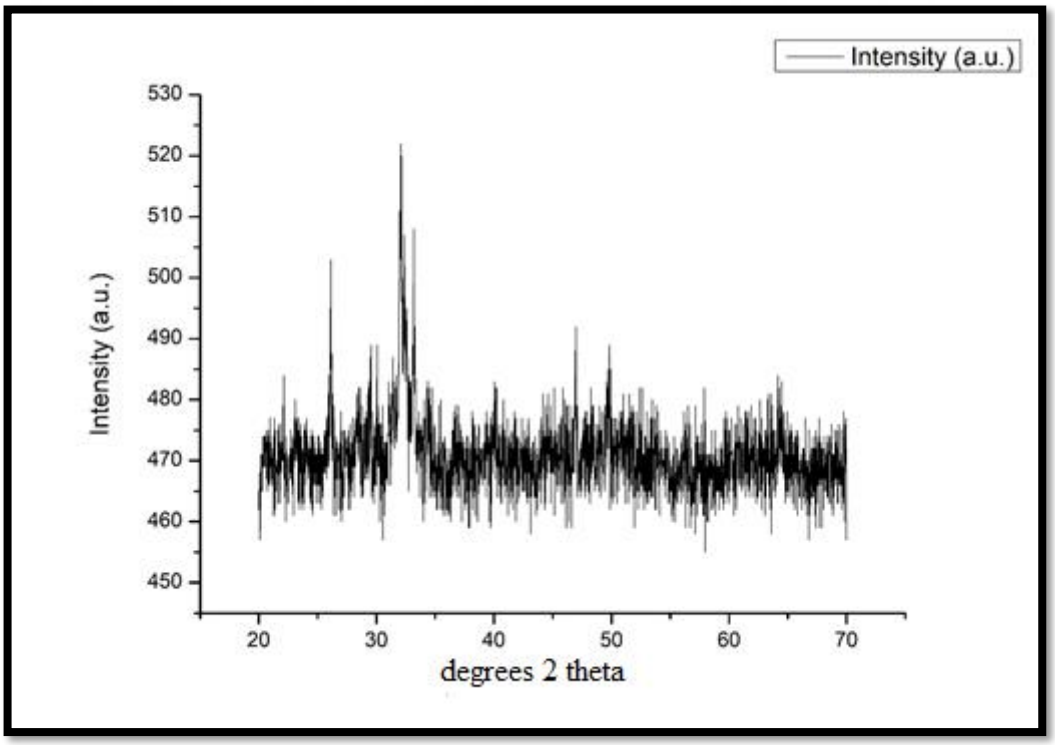

Figure 3.13. The XRD spectrum of 85C-0/50.

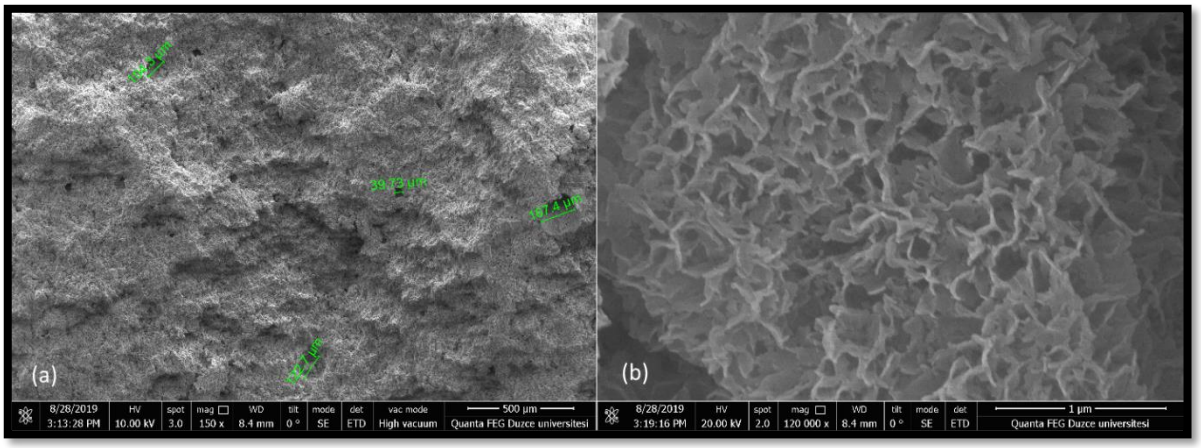

Figure 3.14. The SEM images of 85C-0/50, (a) 500X (b) 120.000X magnification.

3.3.2.2. Inclusion of Gelatin and Silk-fibroin Protein as the Organic Content

58C-2/50 (Ca/P=3.12 , ca. 13.43±4.10°) was prepared to contain 2 wt. percent gelatin and silk-fibroin protein. The FT-IR spectrum (Figure 3.12) for 58C-2/50 displayed typical phosphate peaks as well as an intense carbonate peak at 875 cm^{-1} and an intense O-H stretch in the 3200-3600 cm-1 region due to the organic content and thus increased hygroscopicity of the cements, which is expected as the FT-IR peaks for silk-fibroin are expressed in this region, typically at 3296 cm^{-1} for Amide A, at 1630, 1516, and 1231 cm^{-1} for Amide I, II, and III respectively, while the gelatin peaks can be found at the regions of 3411 cm^{-1} for NH, 2874-2938 cm^{-1} region for CH_2, and 1649 cm^{-1} for Amide I, 1537 cm^{-1} for Amide II, 1243 cm^{-1} for Amide III, 1085 cm^{-1} for CH_3 and 554-607 cm^{-1} range for the C-O-C. The XRD spectrum (Figure 3.15) displayed typical HA peaks and a broader peak than the 31-34 °2θ HA peaks of 85C-0/50. The sizes of nanorod shaped crystals were less than 100 nm (Figure 3.16).

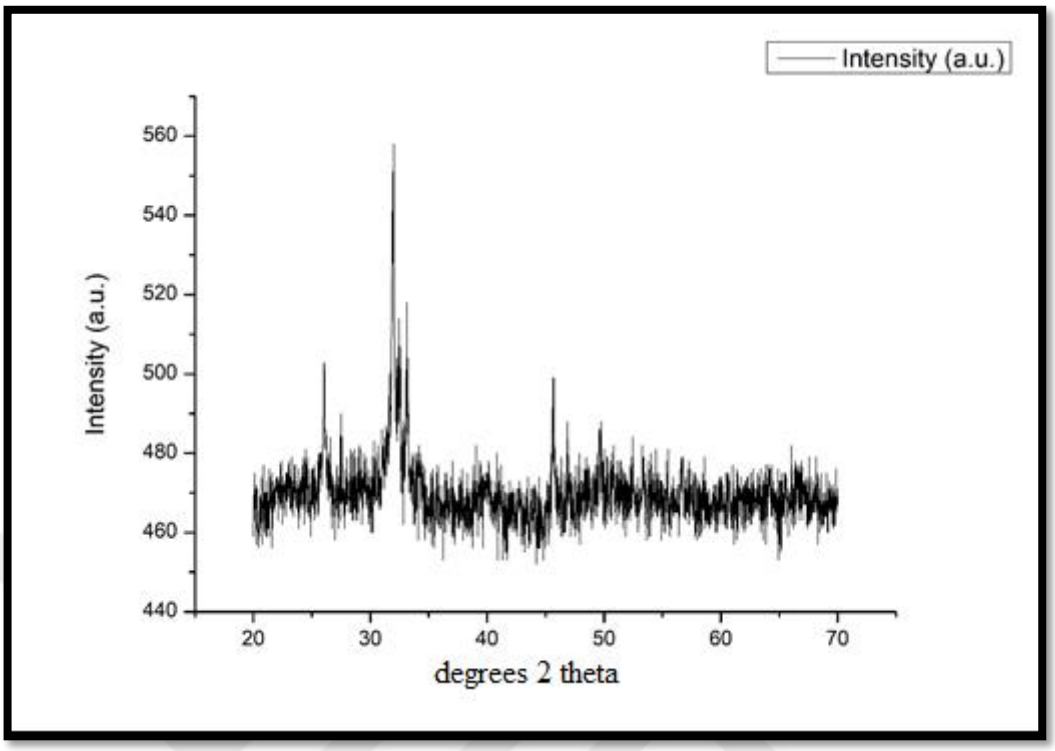

Figure 3.15. The XRD spectrum of 58C-2/50 (containing Na_2CO_3).

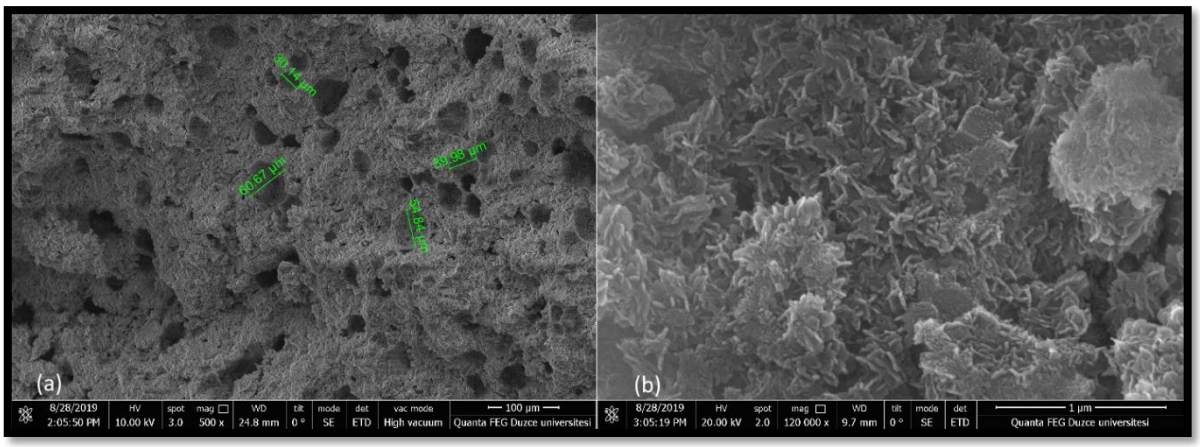

Figure 3.16. The SEM images of 58C-2/50. (a) 500X (b) 120.000X magnification.

3.3.2.3. The Variation in the Concentration of the Organic Component

In the initial phase of this study, the aim was to formulate the cement (C) with the adequate amount of organic content, i.e. gelatin and silk-fibroin protein in the cement (Table 3.1). The FT-IR spectra of the CPC formulations displayed the characteristic HA peaks; while the OH^-

peak, appearing at 3570 cm^{-1}, was overshadowed with a wide O-H stretch indicating both high water and organic component in these formulations. 75C-5/25 (with Ca/P=1.95, ca. 39.67±1.71°) had a higher gelatin content than 79C-3/25 (Ca/P=2.17, ca. 15.44±1.15°). Thus, the water content of the formulation was increased in proportion so that water would not be absorbed by the hydration shell of the organic content and could be used in the dissolution of the inorganic reactants. Similarly, when compared with 80C-3/37 (Ca/P=1.71, ca. 28.8±1.78°), 76C-5/37 (Ca/P=1.76, ca. 48.59±1.08°) was shown to have higher water content and thus higher intensity in the FT-IR spectrum. On the other hand, the cements, 76C-5/37 and 80C-3/37, setting at a higher temperature (37 °C) displayed lower intensity O-H stretch band as more water was expected to evaporate at that temperature (Figures 3.16 and 3.17). An intense O-H stretch in the 3200-3600 cm^{-1} region, which is expected as the FT-IR peaks for gelatin and silk-fibroin in the formulation, increasing the hygroscopicity of the cements, are expressed in this region, for silk-fibroin, typically at 3296 cm^{-1} for Amide A 1630, 1516, and 1231 cm^{-1} for Amide I, II, and III respectively, while the gelatin peaks can be found at 3411 cm^{-1} for NH, 2874-2938 cm^{-1} region for CH_2, 1649 cm^{-1} for Amide I, 1537 cm^{-1} for Amide II, 1243 cm^{-1} for Amide III, 1085 cm^{-1} for CH_3 and 554-607 cm^{-1} range for the C-O-C.

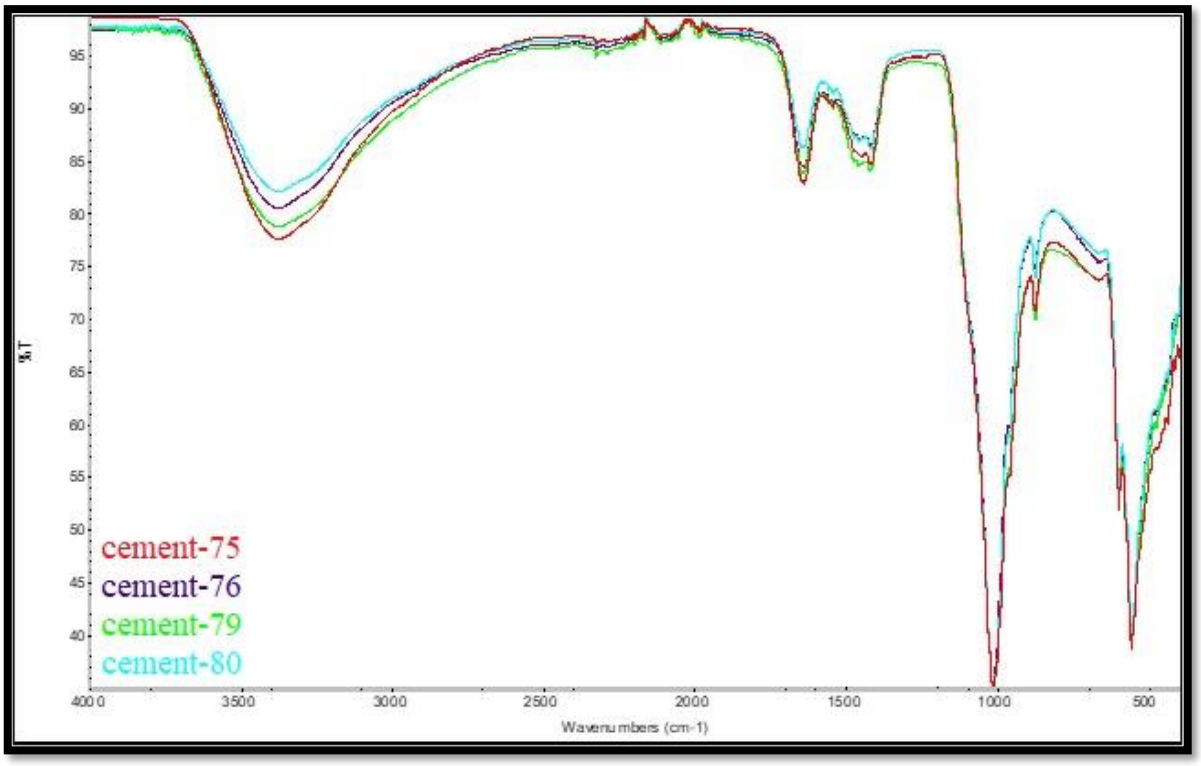

Figure 3.17. The FT-IR spectra of 75C-5/25, 76C-5/37, 79C-3/25 and 80C-3/37.

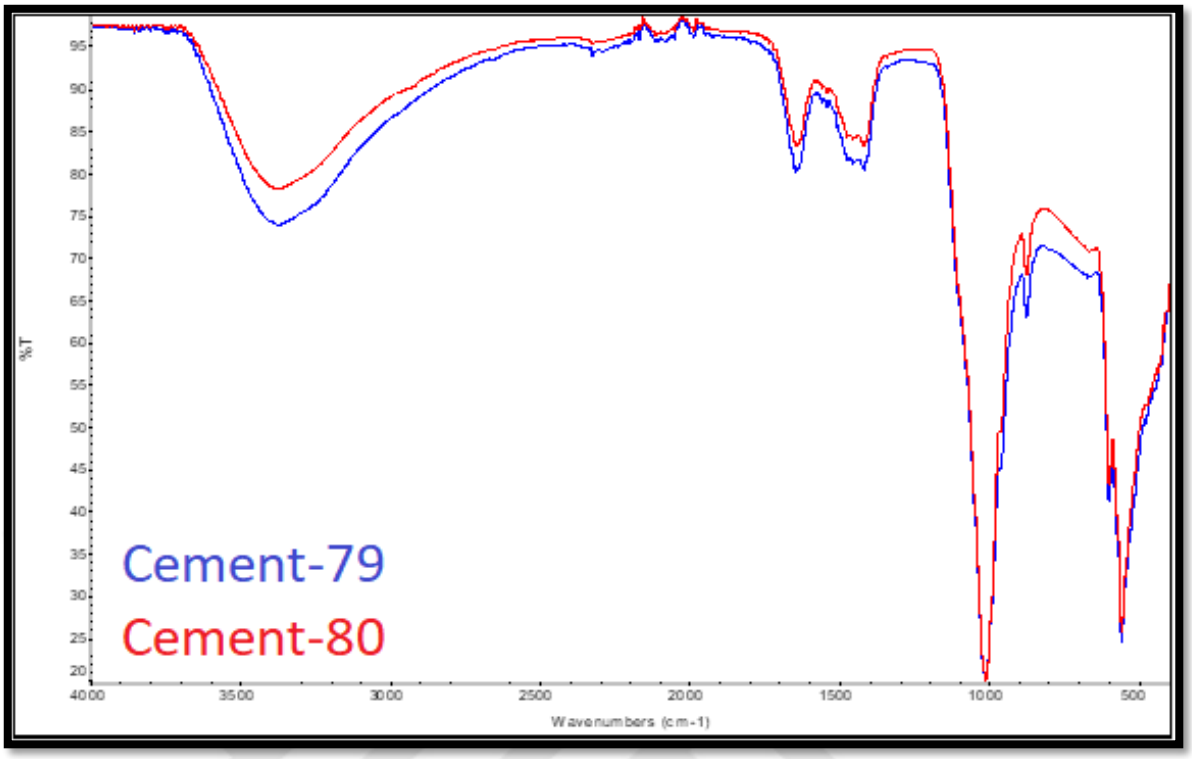

Figure 3.18. The FT-IR spectra of 79C-3/25 and 80C-3/37.

The XRD analysis (Figures 3.19.-.3.22.) displayed typical HA peaks at 25.9°, 28.69°, 29.42° 2θ, the 100 percent intensity peak at 31.7° 2θ in the 30-34° 2θ range, and the 49.5° 2θ peak in the 45-53° 2θ ranges in all the samples. The lower intensity 32.1° 2θ and 32.9° 2θ peaks observed in the broad 31-34° 2θ band in 75C-5/25 and 76C-5/37 may be due to higher gelatin content compared with the slightly sharper peaks in the 31-34° 2θ peak band observed in 79C-3/25 and 80C-3/37. The SEM images of these cements (Figures 3.23-3.26) displayed nanorod shaped Ca-P crystals of sizes less than 100 nm. 79C-3/25 and 80C-3/37 displayed higher attenuation and higher electron density, implying higher calcification at the site of higher attenuation.

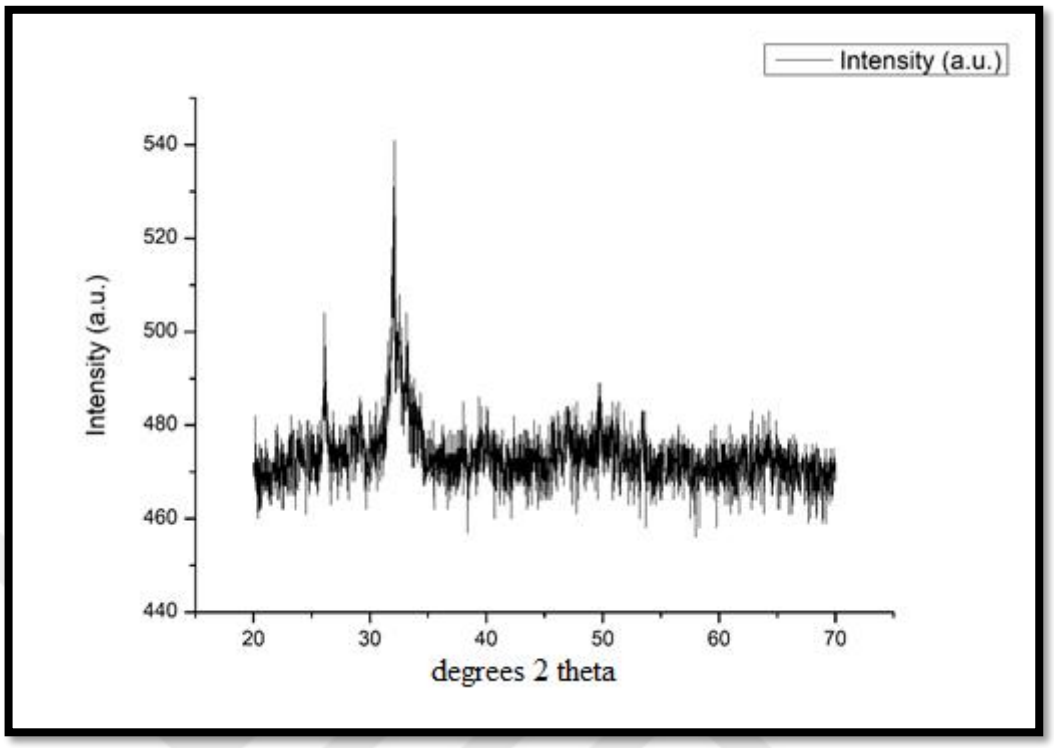

Figure 3.19. The XRD spectrum of 75C-5/25 (25 °C).

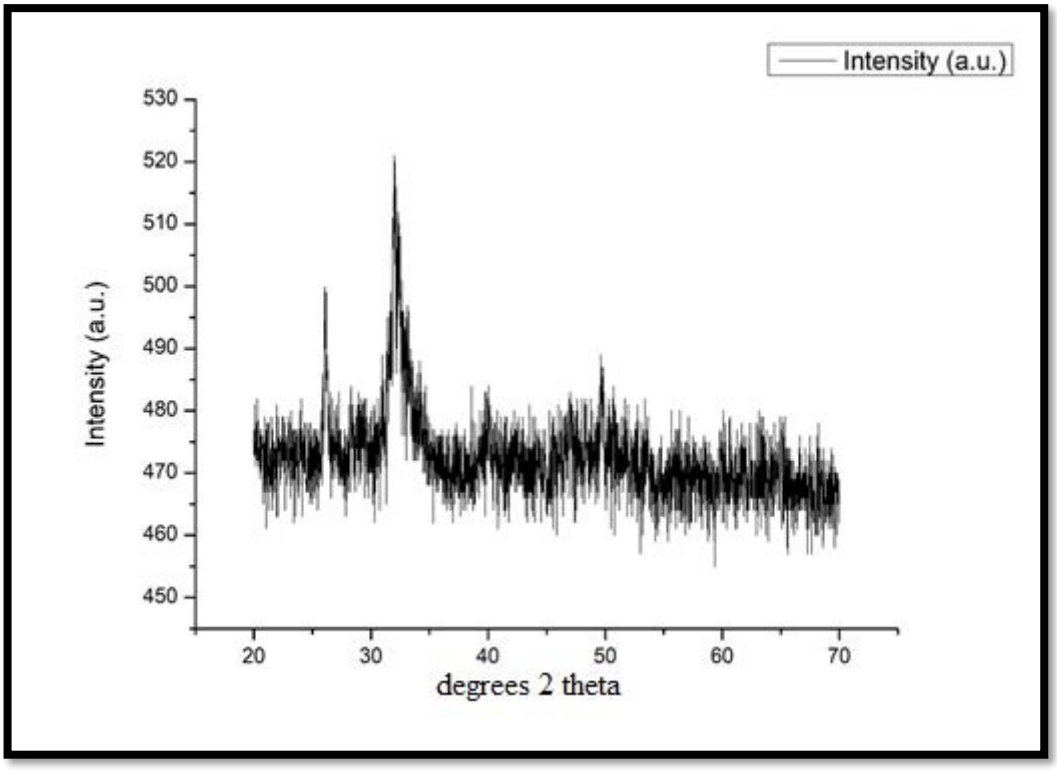

Figure 3.20. The XRD spectrum of 76C-5/37.

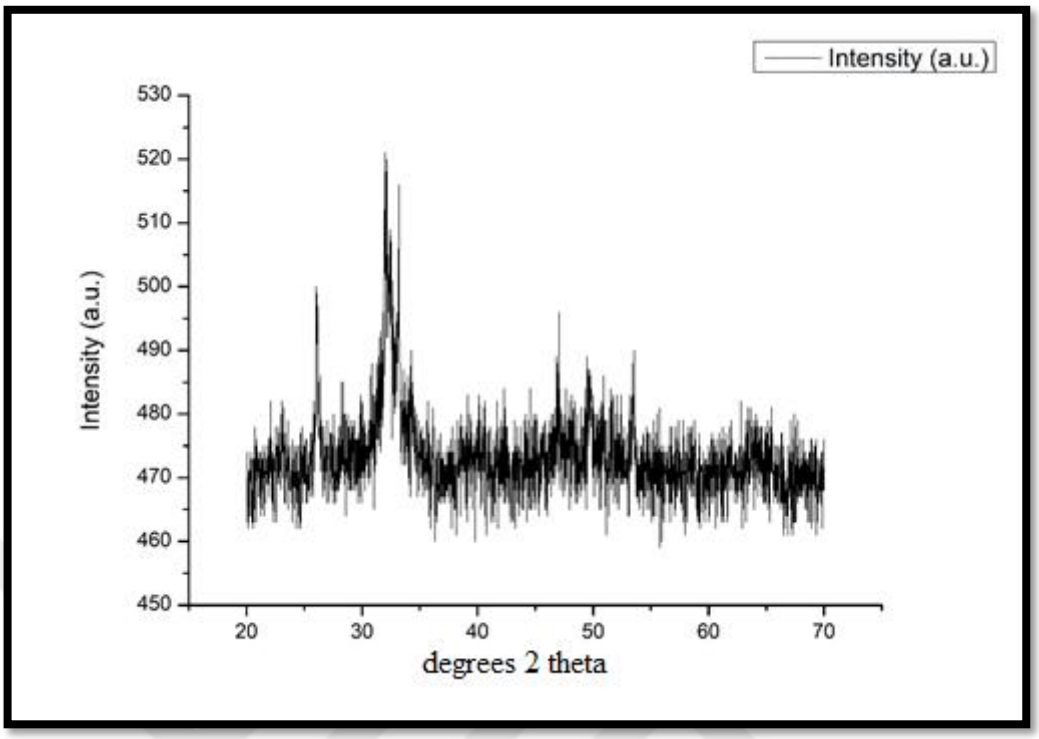

Figure 3.21. The XRD spectrum of 79C-3/25.

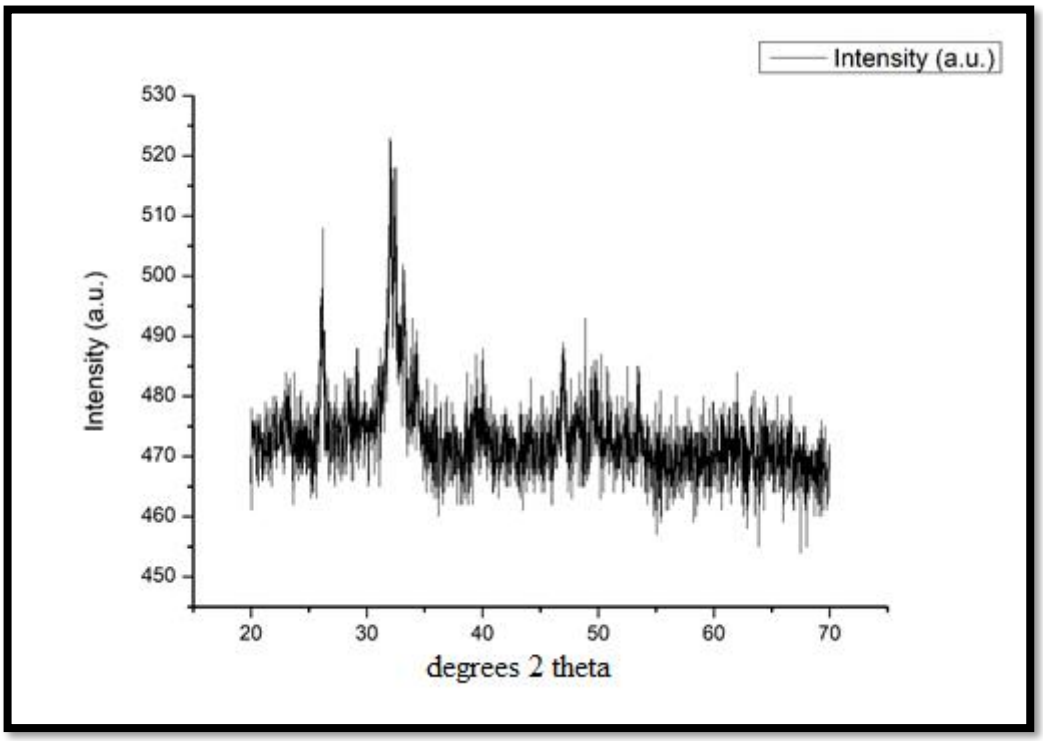

Figure 3.22. The XRD spectrum of 80C-3/37.

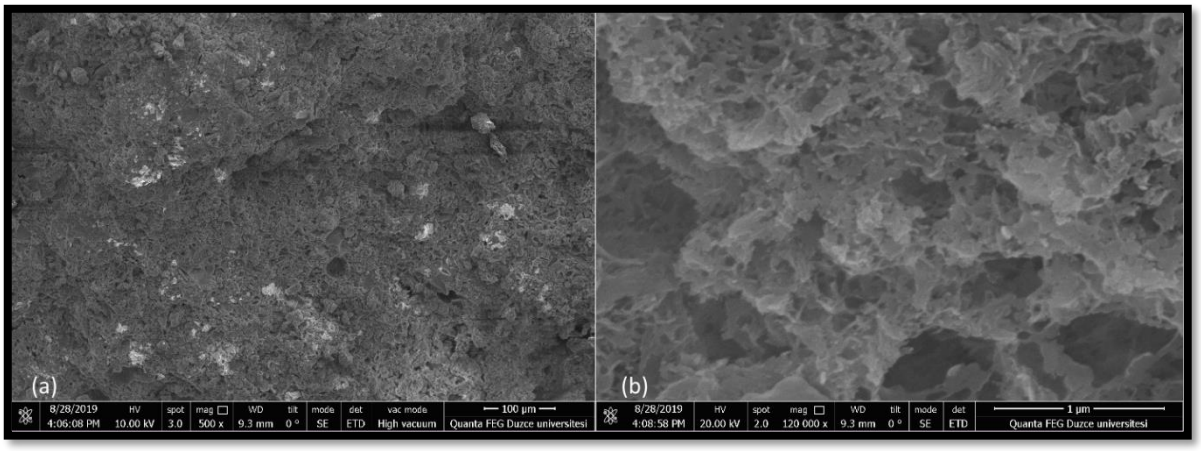

Figure 3.23. The SEM images of 75C-5/25 (Ca/P=1.95). (a) 500X (b) 120.000X magnification.

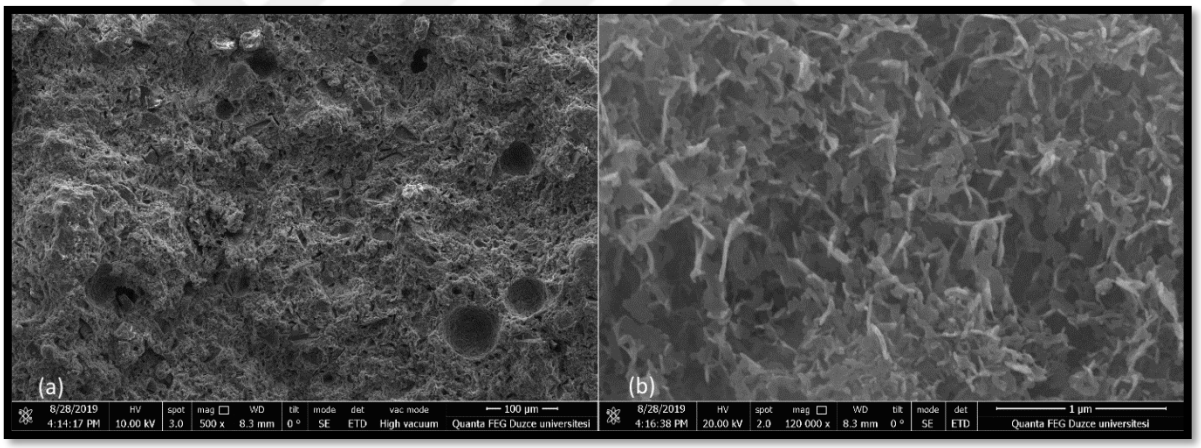

Figure 3.24. The SEM images of 76C-5/37 (Ca/P=1.76). (a) 500X (b) 120.000X magnification.

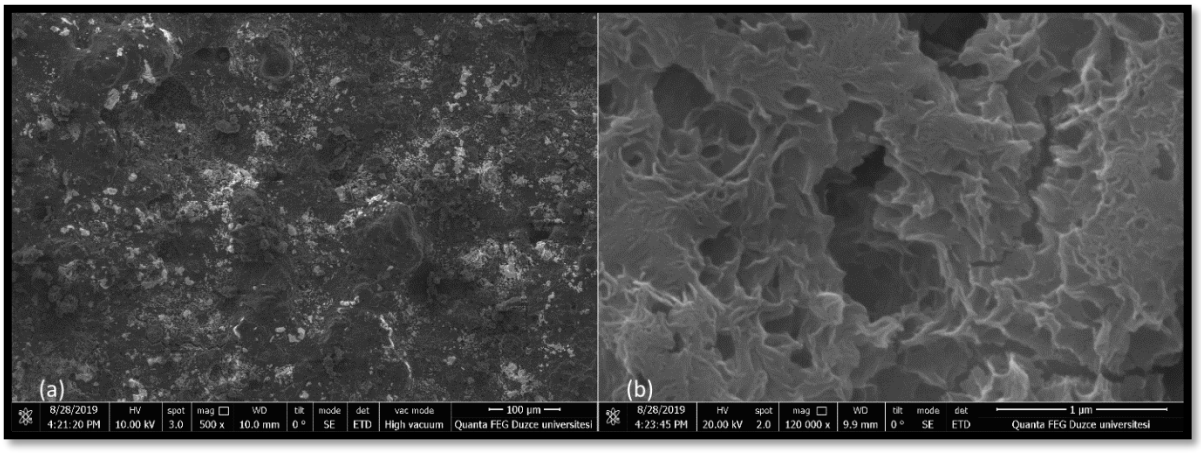

Figure 3.25. The SEM images of 79C-3/25 (Ca/P=2.17). (a) 500X (b) 120.000X magnification.

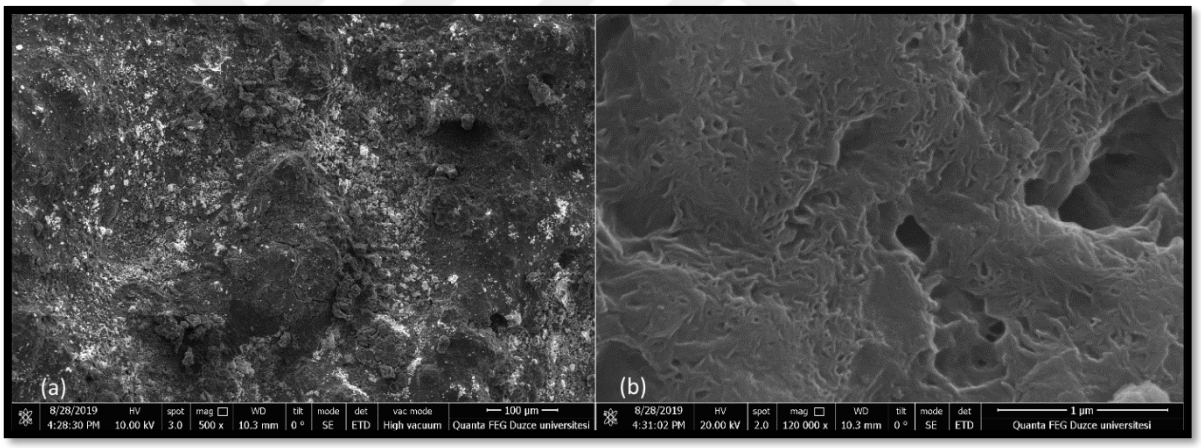

Figure 3.26. The SEM images of 80C-3/37 (Ca/P=1.71). (a) 500X (b) 120.000X magnification.

3.3.2.4. The Effect of Temperature on the Reaction Product

The effect of setting temperature (sT) both on the reaction process and the final product was investigated. The setting temperature was modified as 25 °C, 37 °C, 50 °C, 65 °C and 80 °C, while keeping the gelatin ratio constant at 5 wt. percent and using $CaCO_3$ as the salt. The FT-IR (Figure 3.27.) and the XRD spectra (Figures 3.28.-3.30.) for these cements 75C-5/25 (Ca/P=1.95, ca. 39.67±1.71°), 76C-5/37 (Ca/P=1.76, ca. 48.59±1.08°), 73C-5/50 (Ca/P=2.29, ca. 13.21±6.97°), 69C-5/65 (Ca/P=1.88, ca. 18.98±3.95°), and 70C-5/80 (Ca/P=1.90, ca. 21.52±9.17°) are given in Figures 3.27.-3.30. The FT-IR spectra for the

cements indicated presence of characteristic phosphate, carbonate, amine peaks and an O-H stretch. The cements 70C-5/80 and 73C-5/50 displayed an O-H stretch of lower intensity, probably due to denaturation of the organic content as a result of the increase in temperature, with the exception of 65 °C cement (69C-5/65) which displayed the highest intensity. The XRD spectra of these cements displayed typical HA peaks at 25.9°, 28.69°, 29.42° 2θ, the 100 percent intensity peak at 31.7° 2θ in the 30-34° 2θ range, and the 49.5° 2θ peak in the 45-53° 2θ ranges in all the samples. The lower intensity 32.1° 2θ and 32.9° 2θ peaks observed in the broad 31-34° 2θ band may be due to higher gelatin content. The characteristic HA peaks observed at higher angles were of lower intesity in cement 69C-5/65. The SEM images (Figures 3.31-3.33) displayed nanorod shaped Ca-P crystals of less than 100 nm.

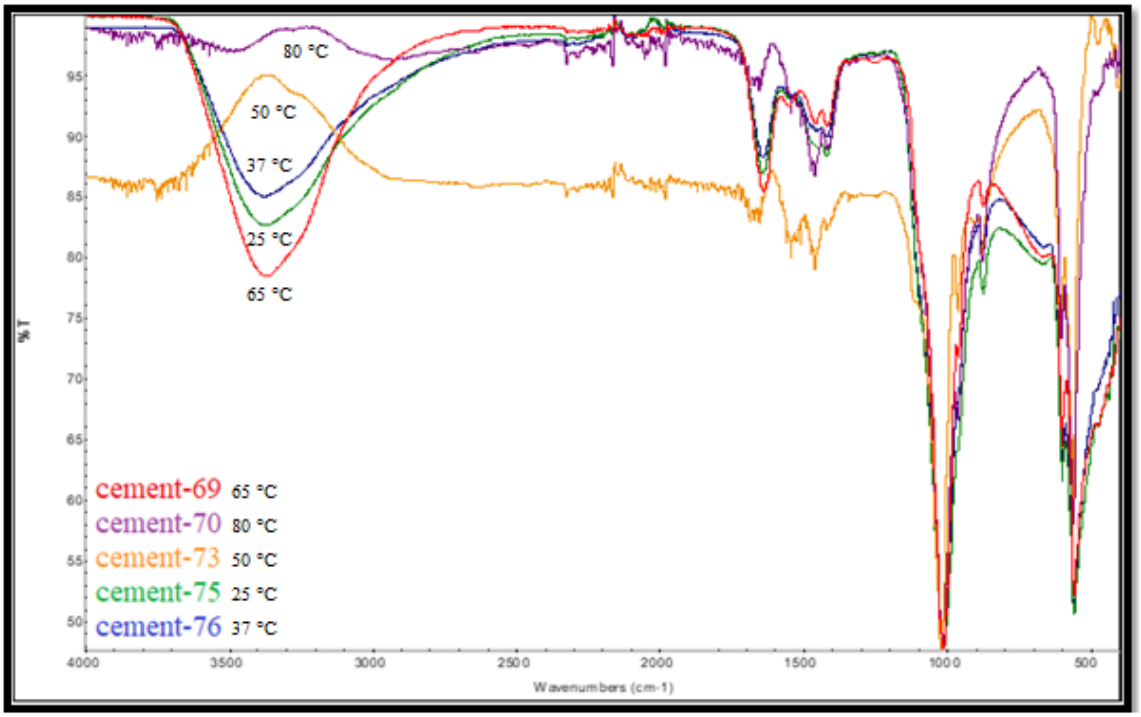

Figure 3.27. The FT-IR spectra of 75C-5/25, 76C-5/37, 73C-5/50, 69C-5/65, 70C-5/80 (containing $CaCO_3$).

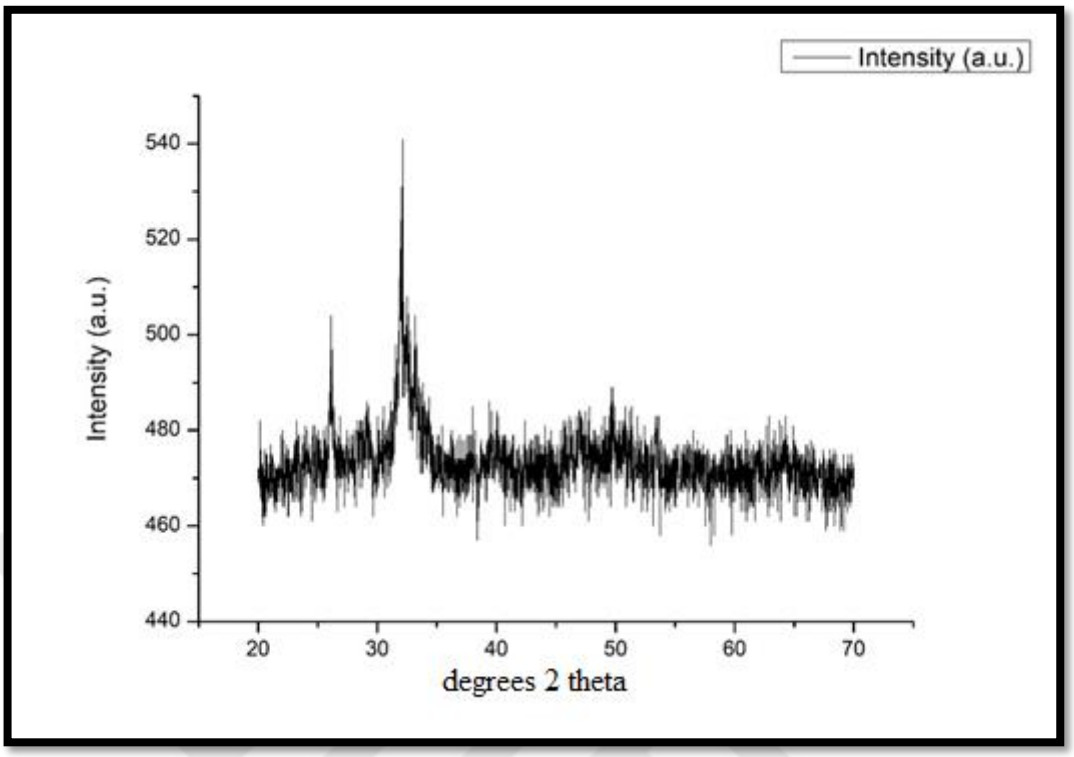

Figure 3.28. The XRD spectrum of 73C-5/50.

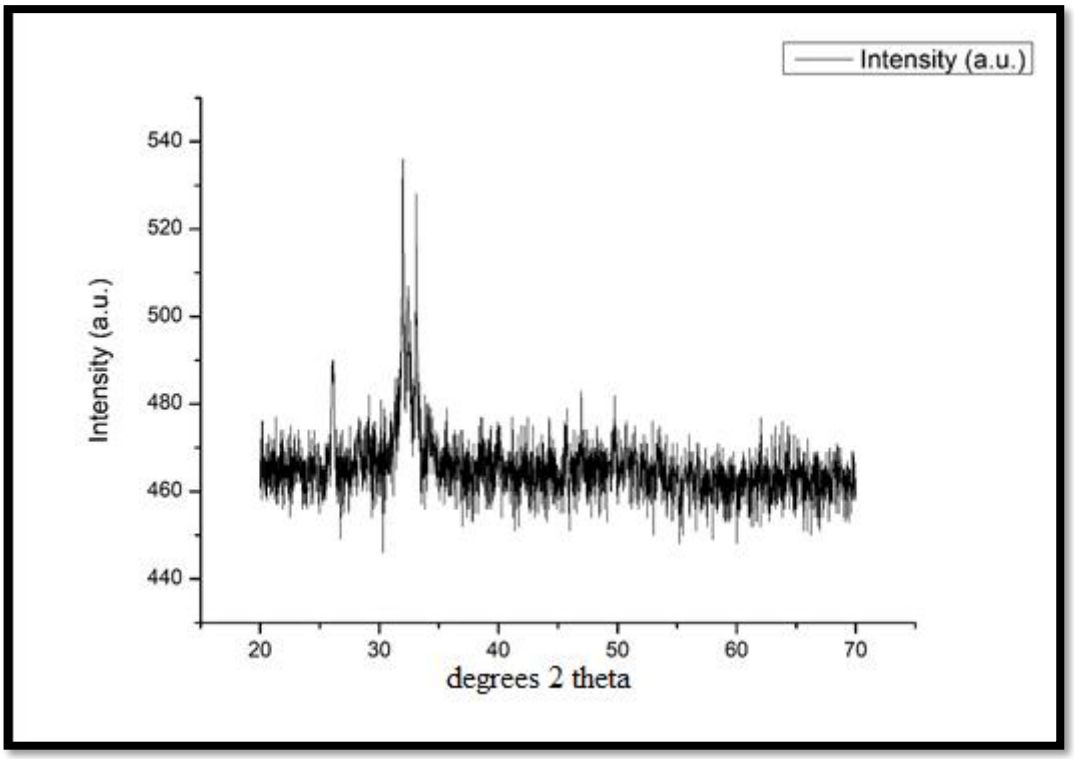

Figure 3.29. The XRD spectrum of 69C-5/65.

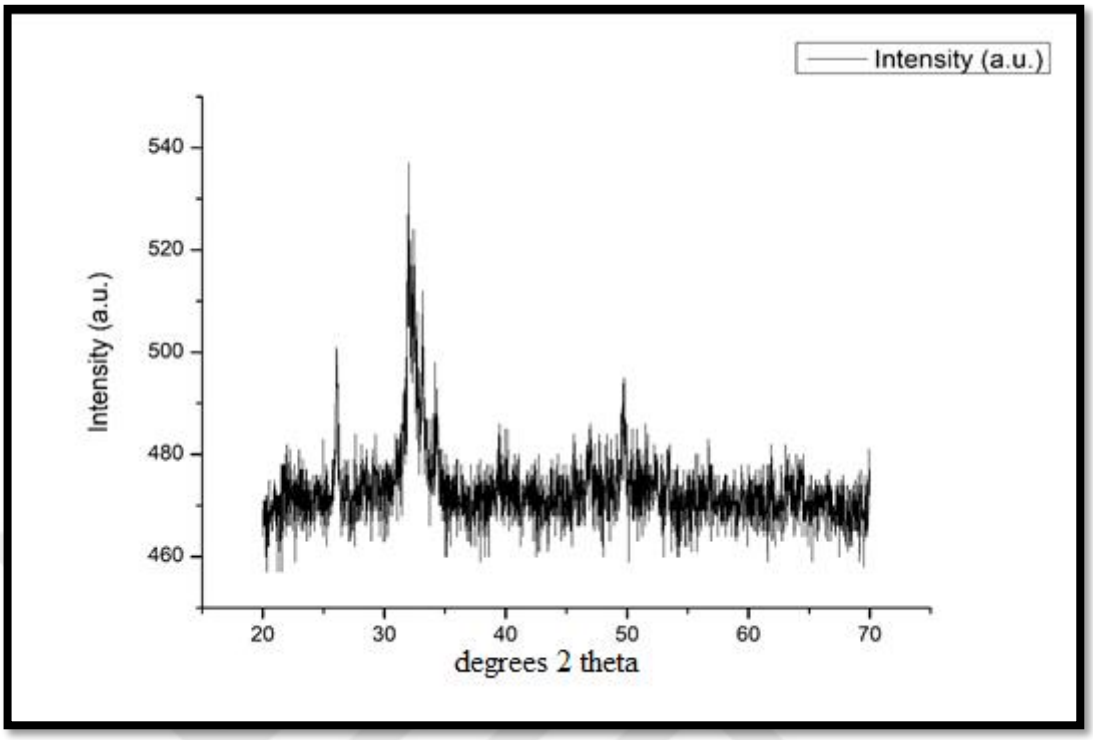

Figure 3.30. The XRD spectrum of 70C-5/80.

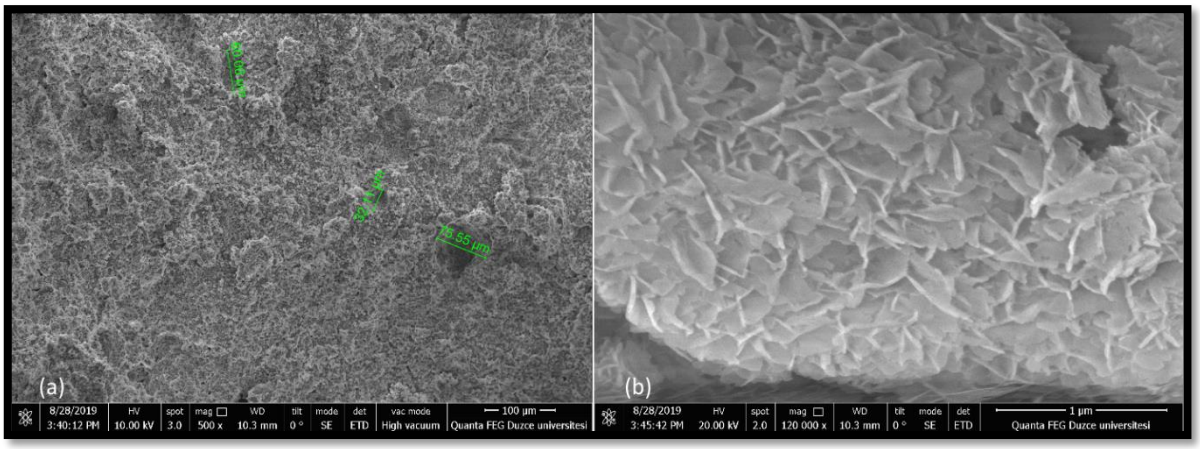

Figure 3.31. The SEM images of 70C-5/80 (Ca/P=1.90). (a) 500X (b) 120.000X magnification.

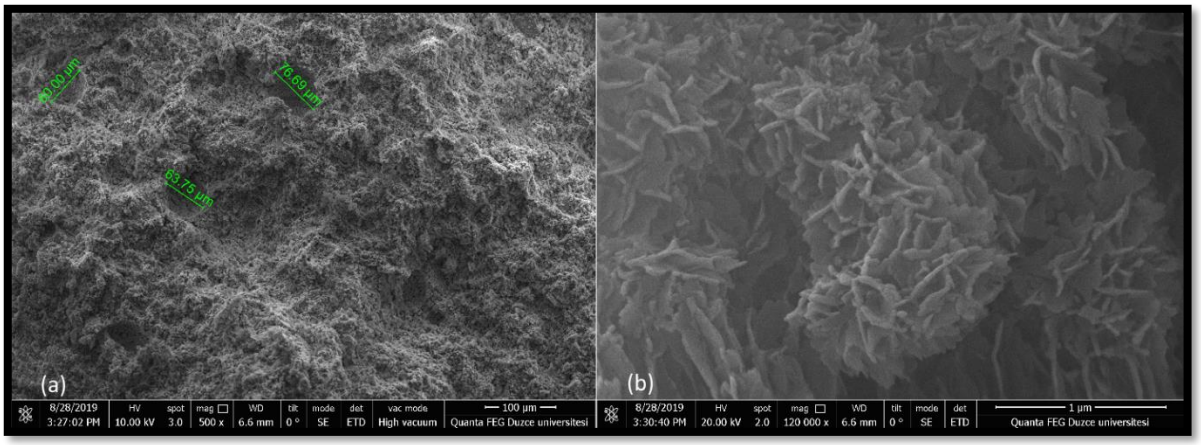

Figure 3.32. The SEM images of 69C-5/65 (Ca/P=1.88). (a) 500X (b) 120.000X magnification.

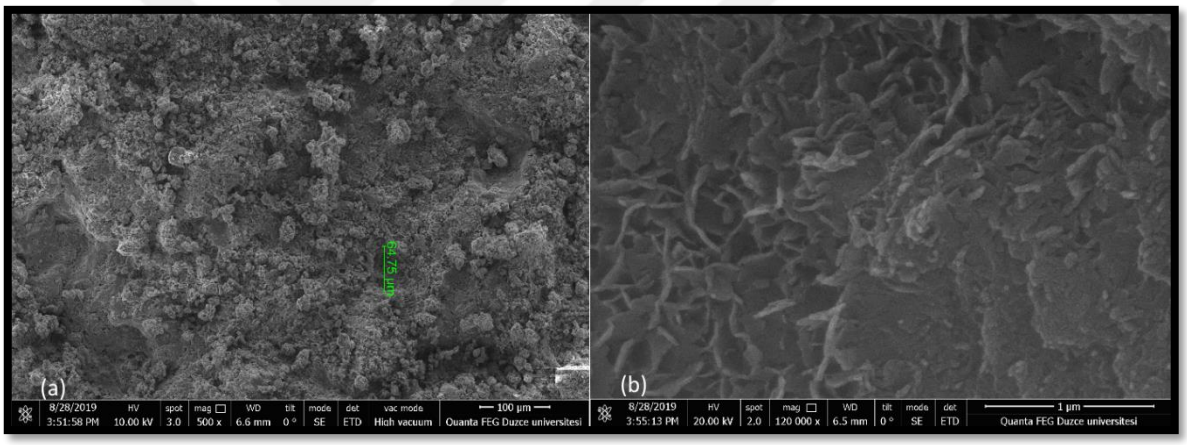

Figure 3.33. The SEM images of 73C-5/50 (Ca/P=2.29). (a) 500X (b) 120.000X magnification.

3.3.2.5. The Effect of Carbonate Cation and Water Content

The effect of carbonate cation on cement was tested using the cement set with two different concentrations of water content (3 wt. percent gelatin and 50 °C setting time) with $CaCO_3$ and Na_2CO_3 (equimolar) or only Na_2CO_3. 81C-3/50NaH (Ca/P=1.72, ca. 23.36°) and 83C-3/50NCH (Ca/P=1.76, ca. 64.46°±0.87°) had a higher water content than 82C-3/50NaL (Ca/P=1.80, ca. 20.86°±12.02°) and 84C-3/50NCL (Ca/P=2.54, ca. 77.72°±9.18°). The FT-IR results (Figure 3.34) indicated presence of phosphate and carbonate peaks as well as the O-H stretch, intensity of which varied as a function of organic content and absorbed water. Although the XRD spectra (Figures 3.35.-3.38) displayed characteristic HA peaks in all

cements, those with a higher water content displayed 28.46° 2θ peak of higher intensity. The SEM images (Figures 3.39-3.42) displayed Ca-P flakes or plate-like crystals.

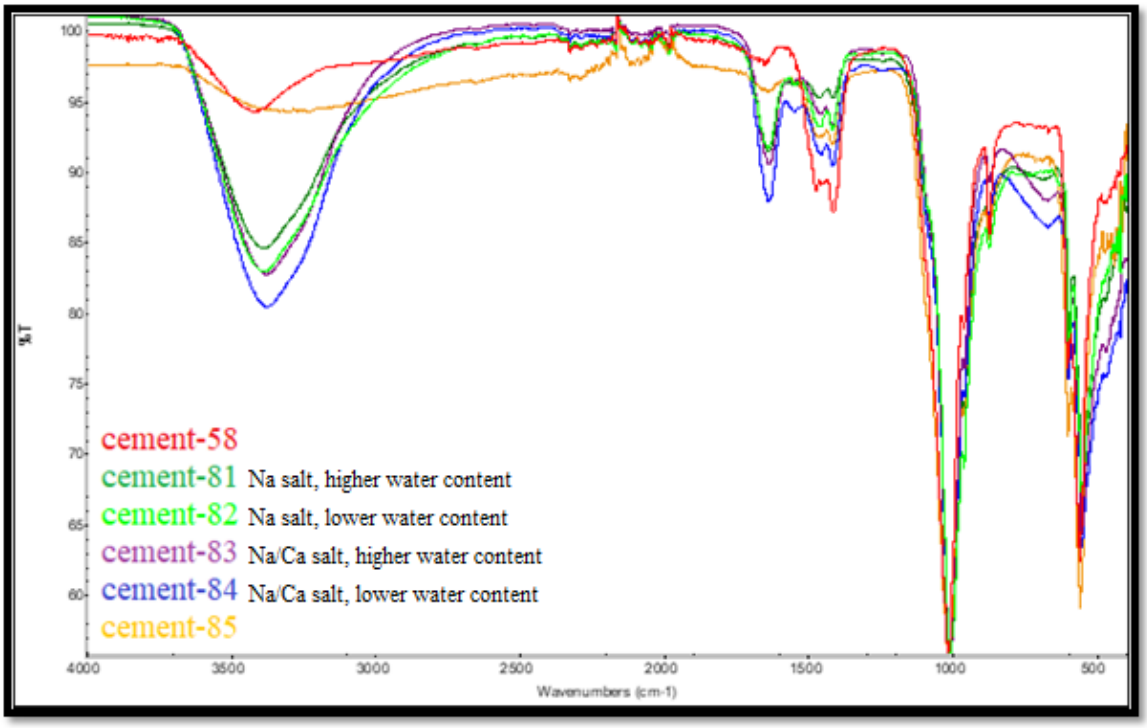

Figure 3.34. The FT-IR spectra of cements set at 50 °C. 81C-3/50NaH, 82C-3/50NaL, 83C-3/50NCH, 84C-3/50NCL, 58C-2/50 and 85C-0/50.

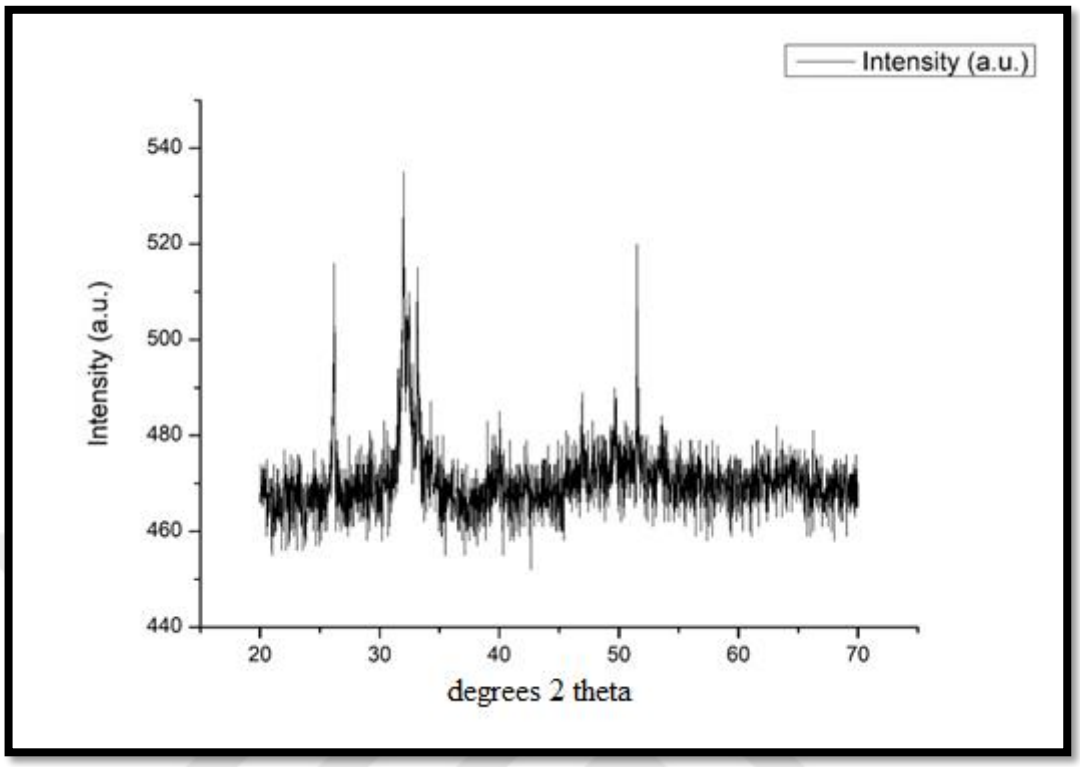

Figure 3.35. The XRD spectrum of 81C-3/50NaH.

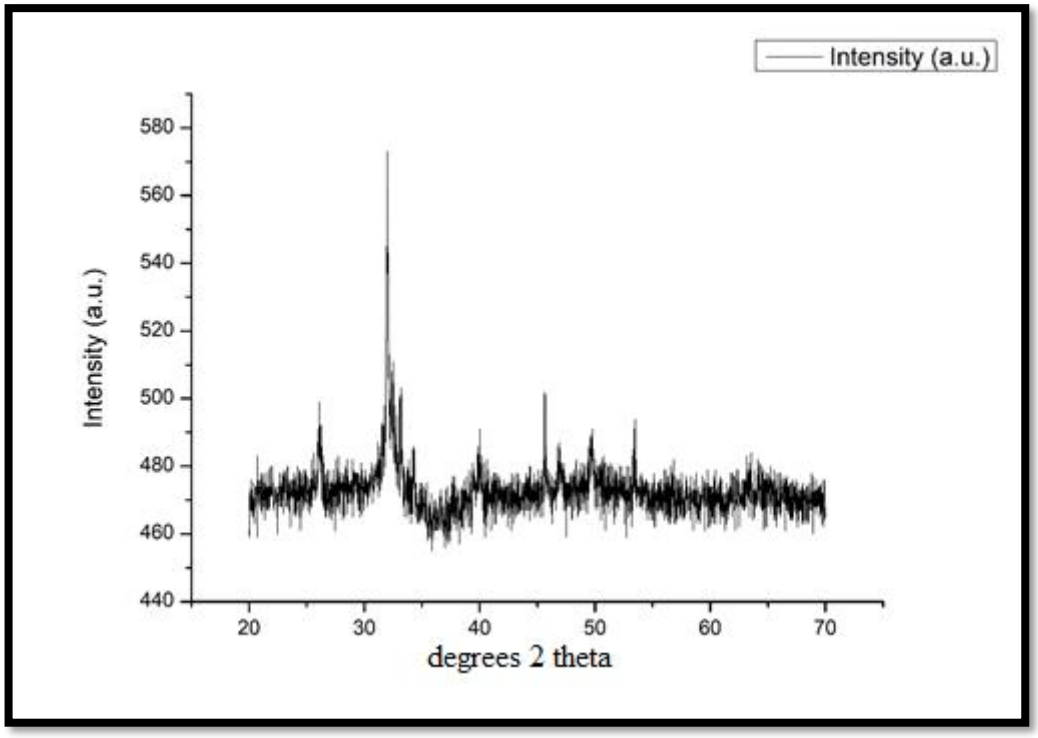

Figure 3.36. The XRD spectrum of 82C-3/50NaL.

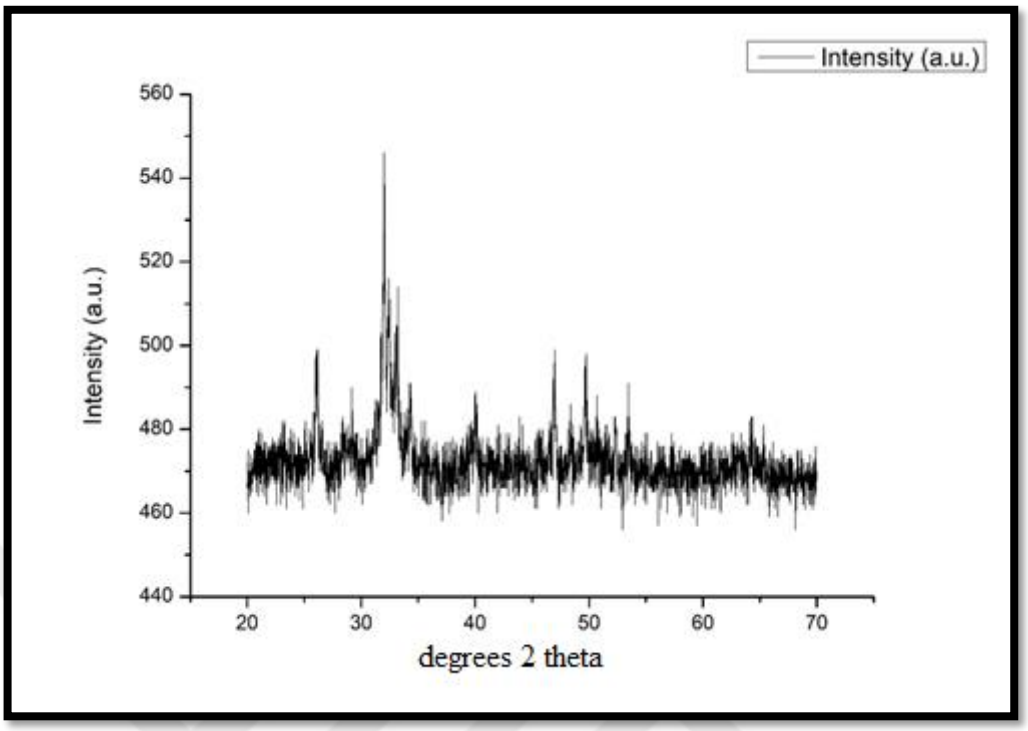

Figure 3.37. The XRD spectrum of 83C-3/50NCH.

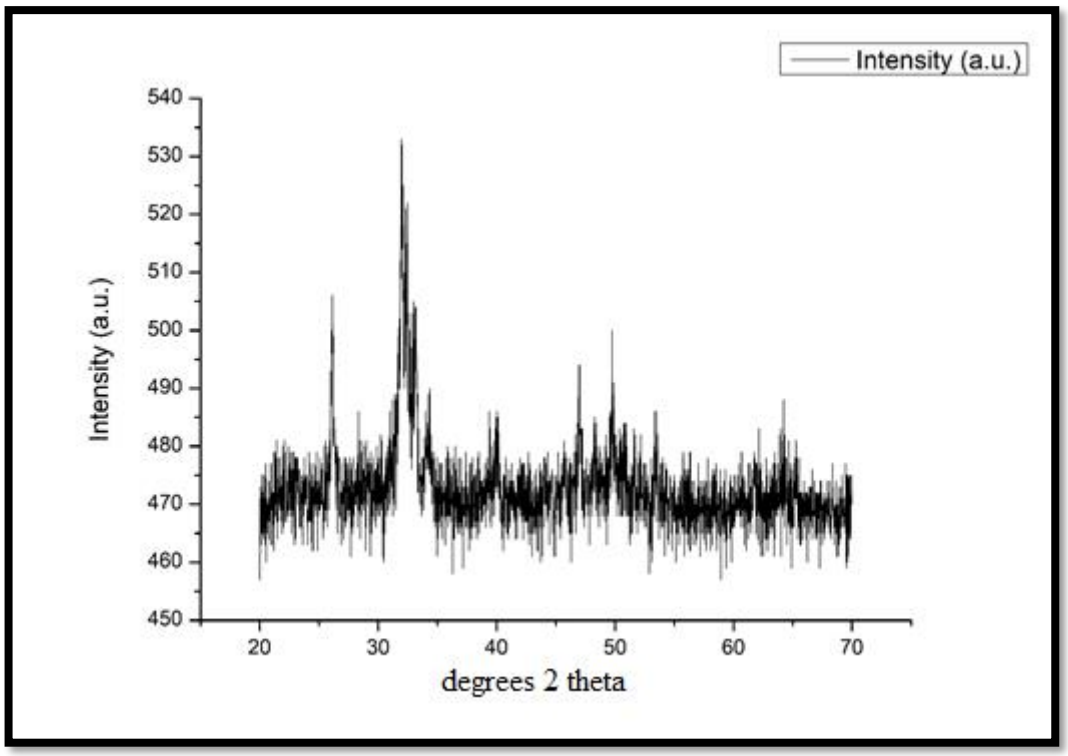

Figure 3.38. The XRD spectrum of 84C-3/50NCL.

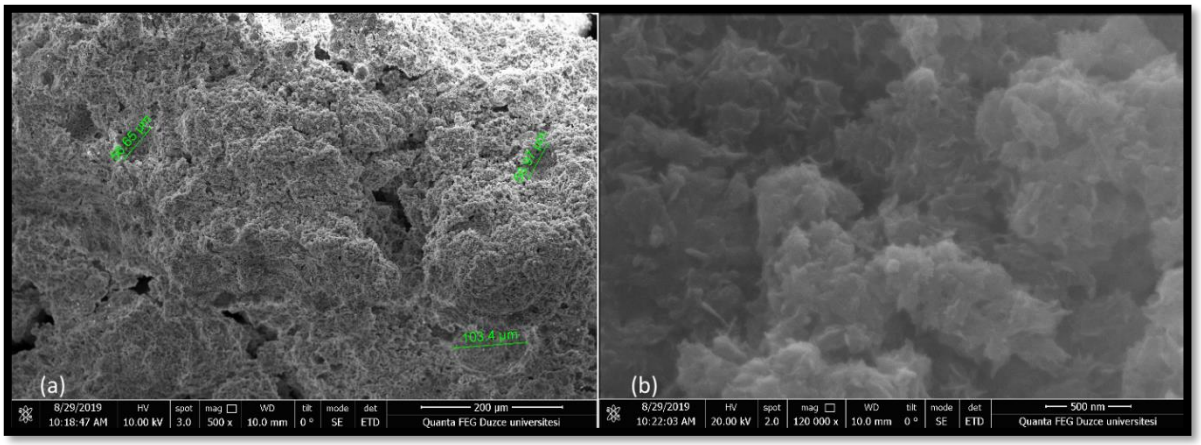

Figure 3.39. The SEM images of 81C-3/50NaH (Ca/P=1.72). (a) 500X (b) 120.000X magnification.

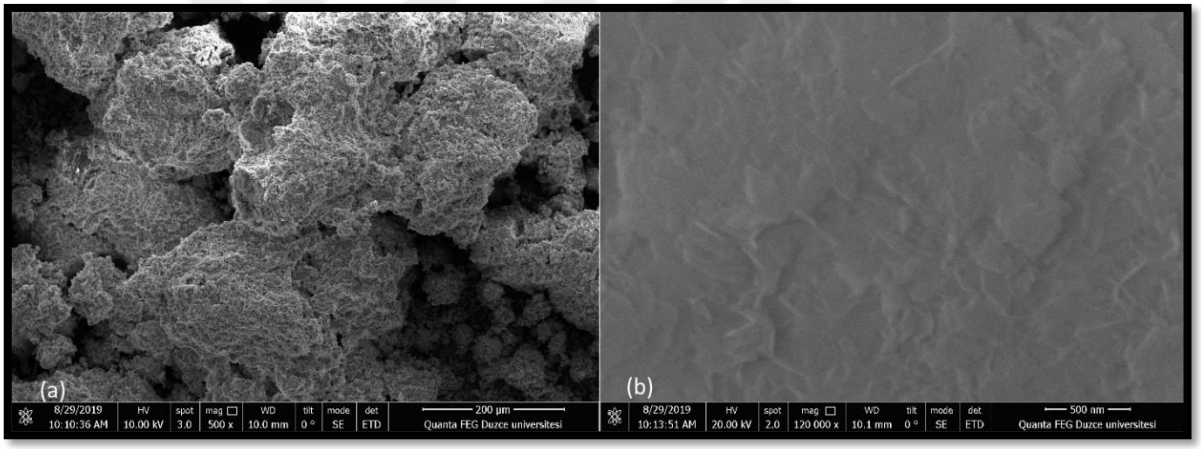

Figure 3.40. The SEM images of 82C-3/50NaL (Ca/P=1.80). (a) 500X (b) 120.000X magnification.

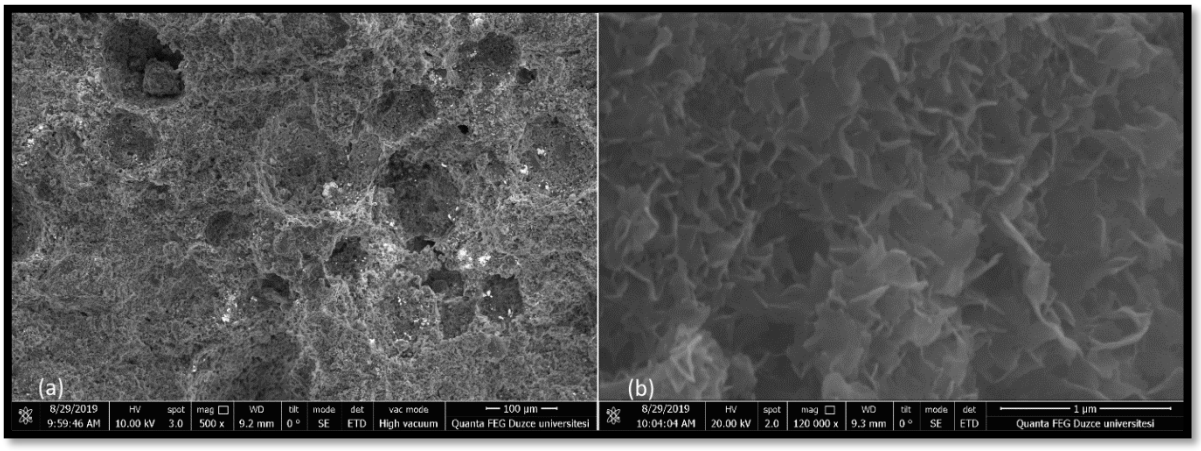

Figure 3.41. The SEM images of 83C-3/50NCH (Ca/P=1.76). (a) 500X (b) 120.000X magnification.

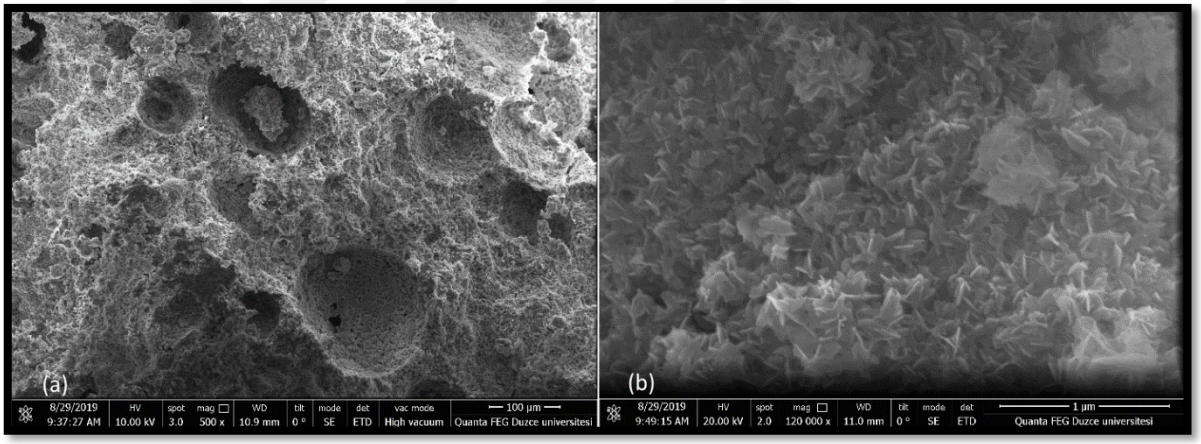

Figure 3.42. The SEM images of 84C-3/50NCL (Ca/P=2.54). (a) 500X (b) 120.000X magnification.

3.3.3. Scanning Electron Microscopic Analysis

Surface morphology and crystal structure of calcium phosphate cements were investigated using the SEM images taken at 500X to 120,000X magnification displaying surface porosity and pore size (Table 3.3). With respect to the SEM images, in terms of pore size and pore distribution, cements 58C-2/50, 76C-5/37, 83C-3/50NCH and 84C-3/50NCL demonstrated higher porosity than other cements.

SEM images indicated variation in cement porosity that differed by the salt type and curing temperature. In cements 75C-5/25, 76C-5/37, 73C-5/50, 69C-5/65 and 70C-5/80 all the chemicals being the same ($CaCO_3$ was used), temperature varied (25 °C, 37 °C, 50 °C, 65 °C and 80 °C respectively). As $CaCO_3$ has the highest solubility at 37 °C [78], with $CaCO_3$ solubility exponentially decreasing with increasing temperatures upto 80 °C, 76C-5/37 had the highest porosity. Thus, water content may be indirectly affecting porosity as demonstrated in the SEM images of 76C-5/37 and 80C-3/37 (Figures 3.24 and 3.26). These cements had different percentages of organic content and thus proportionally differing water content (76C-5/37 was prepared with 280 µl distilled water and 80C-3/37 was prepared with 177 µl distilled water). The proportionality of water content of the cements may have resulted in higher $CaCO_3$ solubility, release of higher amount of CO_3^{2-} ions and thus relatively higher porosity.

On the other hand, 58C-2/50 with Na_2CO_3 content (Figure 3.16) demonstrated higher porosity at 50 °C than 76C-5/37. This may be due to the fact that Na_2CO_3 solubility increases exponentially with temperature until the 40°-50°C range and then slightly decreases with an increase in temperature and becomes stationary. On the contrary, cements 81C-3/50NaH and 82C-3/50NaL (Figure 3.39 and 3.40) with high water content (402, and 281 µl respectively) have displayed low porosity. However, 83C-3/50NCH and 84C-3/50NCL cements, which were prepared with $CaCO_3$ and Na_2CO_3 salts (at 1:1 equal mole ratios) with water content being the only variable (402 and 281 µl respectively) had higher porosity. SEM images indicated that 83-3/50NCH and 84C-3/50NCL cements had different sized pores (micro and macro pores) that probably occurred as a result of using two salts in the cement system. In contrast, 85C-0/50,which was prepared as a basic inorganic cement with a 1:1 equimolar ratio of TTCP:DCPD, and a powder to liquid ratio of 1:2 (0.5 M Na_2HPO_4 as the liquid solution) displayed relatively low (13 percent) and uniform porosity (Figure 3.14).

Table 3.3. Porosity and average pore size of the calcium phosphate cements.

Cement Name	Curing Temperature (°C)	% Porosity	Average Pore Size (µm)
75C-5/25	25	10	37
79C-3/25	25	7	38
80C-3/37	37	6	30
76C-5/37	37	25	44
85C-0/50	50	13	70
58C-2/50	50	60	43
81C-3/50NaH	50	2	20
82C-3/50NaL	50	5	32
83C-3/50NCH	50	58	83
84C-3/50NCL	50	20	64
73C-5/50	50	9	55
69C-5/65	65	3.75	50
70C-5/80	80	6	44

3.3.4. Energy Dispersive X-Ray Spectroscopy (EDS)

Elemental analysis was performed on calcium phosphate cements to determine their element content. Calcium, Carbon, Nitrogen, Oxygen, Phosphorus, Potassium, Sodium and Chloride content was investigated. With respect to elemental analysis, Calcium and phosphate atomic ratios of the calcium phosphate cements were calculated and listed in Table 3.4.

Table 3.4. The Ca/P ratio of the calcium phosphate cements

Cement Name	Curing Temperature (°C)	Ca/P
58C-2/50	50	3.12
75C-5/25	25	1.95
76C-5/37	37	1.76
73C-5/50	50	2.29
69C-5/65	65	1.88
70C-5/80	80	1.90
79C-3/25	25	2.17
80C-3/37	37	1.71
81C-3/50NaH	50	1.72
82C-3/50NaL	50	1.80
83C-3/50NCH	50	1.76
84C-3/50NCL	50	2.54
85C-0/50	50	2.88

3.3.5. Contact Angle Measurements

Contact angle measurements using distilled water were conducted as described in Section 2.3.1. Average contact angle values for each specimen are listed in Table 3.5 (also in Figure 3.43.) with calculations given in Appendix A. All of the specimen were determined to be hydrophilic, satisfying the basic requirements for cell adhesion and proliferation [79].

In the group of cements (75C-5/25, 76C-5/37, 73C-5/50, 69C-5/65, 70C-5/80), where temperature is the only variable, different temperature settings may have an indirect effect on the contact angle value. Higher water evaporation at elevated temperatures reduce the amount of water as well as affecting the solubility of Ca^{+2} and Na^{+} ion compounds in the cement than those cured at lower temperatures. Thus, the cements set at higher temperatures may absorb water more readily and thus have lower contact angles values than those set at physiological and lower temperatures.

Table 3.5. Contact angle measurements of calcium phosphate cement samples (* Initial contact angle (°). Contact angles at later time intervals couldn't be determined because these cements are superhydrophilic).

Sample Name	**Curing Temperature (°C)**	**Mean Contact Angle (°)**
58C-2/50	50	13.43±4.10
75C-5/25	25	39.67±1.71
76C-5/37	37	48.59±1.08
73C-5/50	50	13.21±6.97
69C-5/65	65	18.98±3.95
70C-5/80	80	21.52±9.17
79C-3/25	25	15.44±1.15
80C-3/37	37	28.8±1.78
81C-3/50NaH	50	23.36*
82C-3/50NaL	50	20.86±12.02
83C-3/50NCH	50	64.46±0.87
84C-3/50NCL	50	77.72±9.18
85C-0/50	50	8.00*

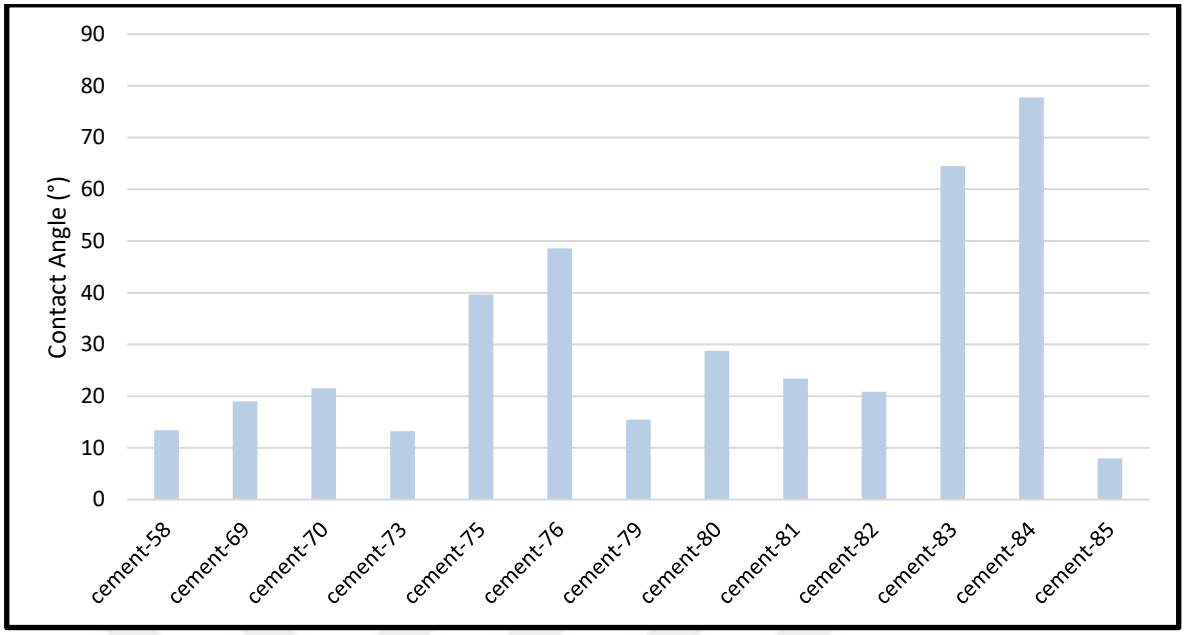

Figure 3.43. The contact angle (°) measurements of the cement samples.

3.3.6. Compression Test

Compressive strength and Young's modulus of the cements are given in Figures 3.41 and 3.42 respectively. Cements with 5 percent gelatin ratio (75C-5/25, 76C-5/37, 73C-5/50, 69C-5/65, 70C-5/80) displayed higher compressive strength (varying between 1.19±0.41 MPa and 3.2±1.12 MPa) and Young's Moduli (varying between 20±14.14 MPa-100±0MPa) than cements with 3 percent gelatin (58C-2/50, 79C-3/25, 80C-3/37, 83C-3/50NCH), with compressive strength varying between 0.31±0.17 MPa and 1.29±0.52 MPa and the Young's moduli varying between 25±7.07 MPa and 70±0 MPa. Compressive strength and the Young's modulus of the control cement 85C-0/50 were determined to be 1.27±0.03 MPa and 100±0 MPa respectively. Additionally, 58C-2/50 containing Na_2CO_3 displayed lower compressive strength (0.65±0.19 MPa) when compared with the cements with $CaCO_3$ salt, probably due to the bivalent and thus chelating nature of calcium ions. The 70C-5/80 cement was not tested as the samples crumbled during the production process. The compressive strength of the cements was evaluated in terms of the variables such as water content (Figure 3.46.), setting temperature (Figure 3.49.), setting time (Figure 3.48.), gelatin content (Figure 3.49.), powder to liquid ratio (P/L ratio) (Figure 3.50.) According to hese results, it may be suggested that higher gelatin content increases both the compressive strength and the elastic modulus.

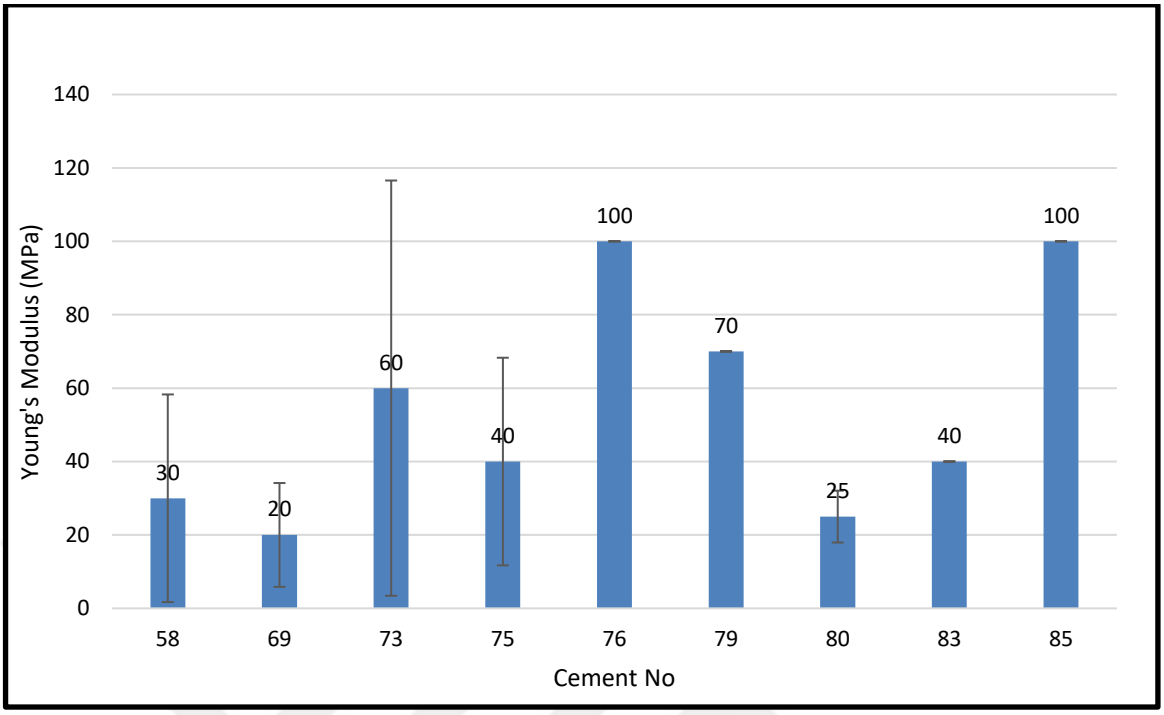

Figure 3.44. The Young's moduli of the cement samples.

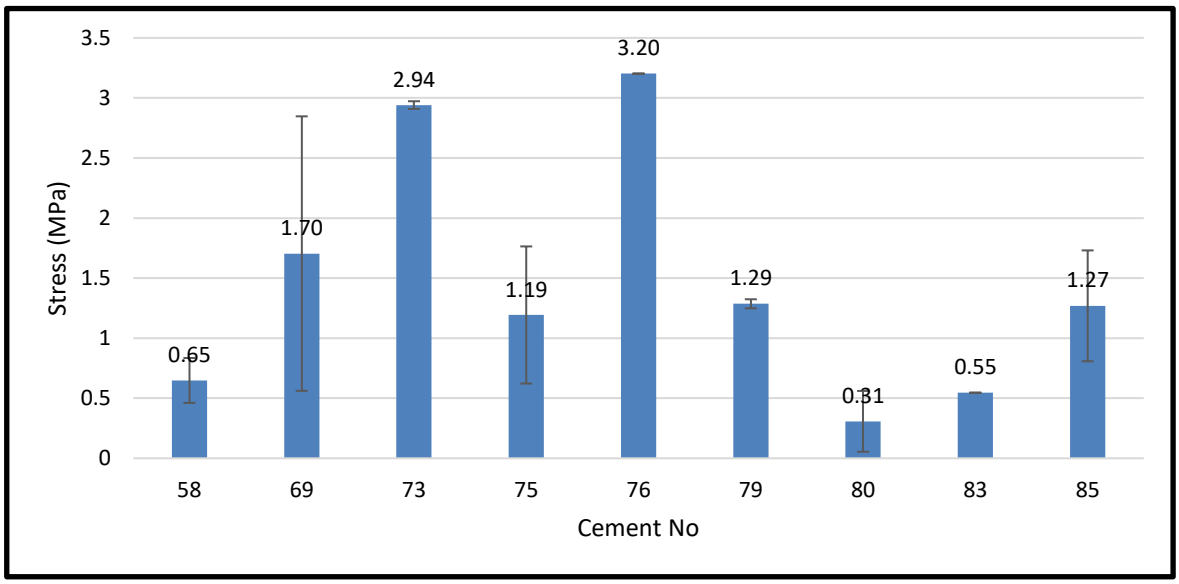

Figure 3.45. The compressive strength of the cement samples.

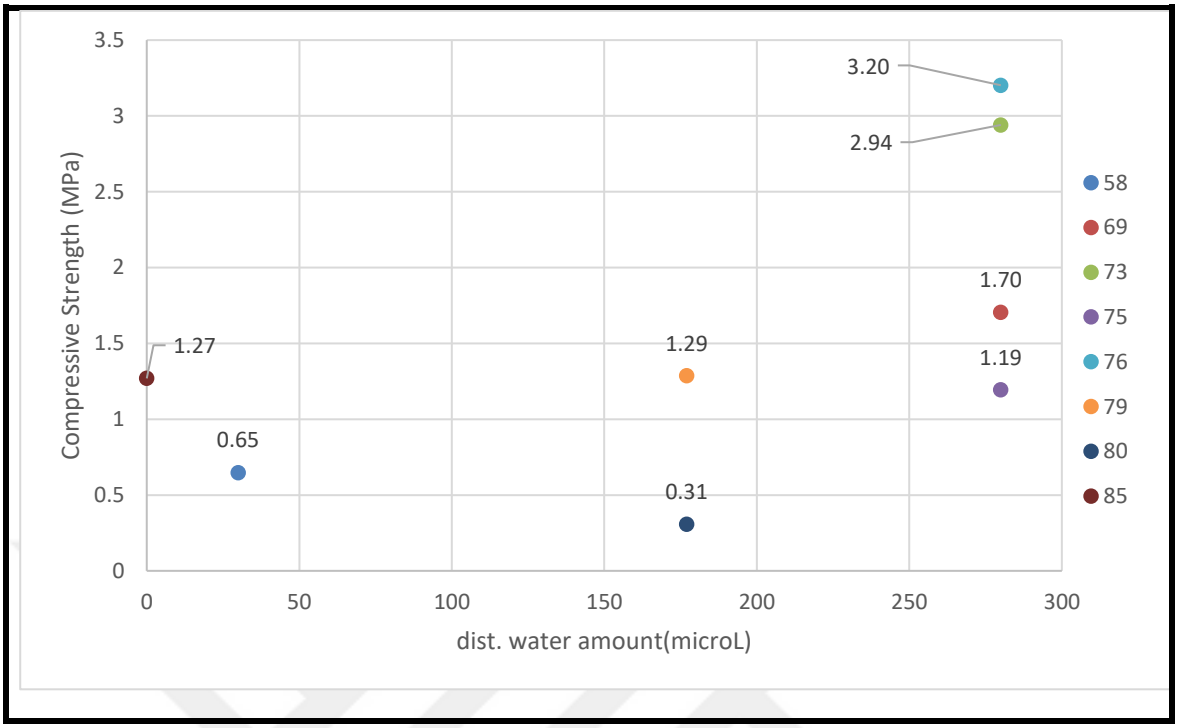

Figure 3.46. The compressive strength of the cement in relation to water content.

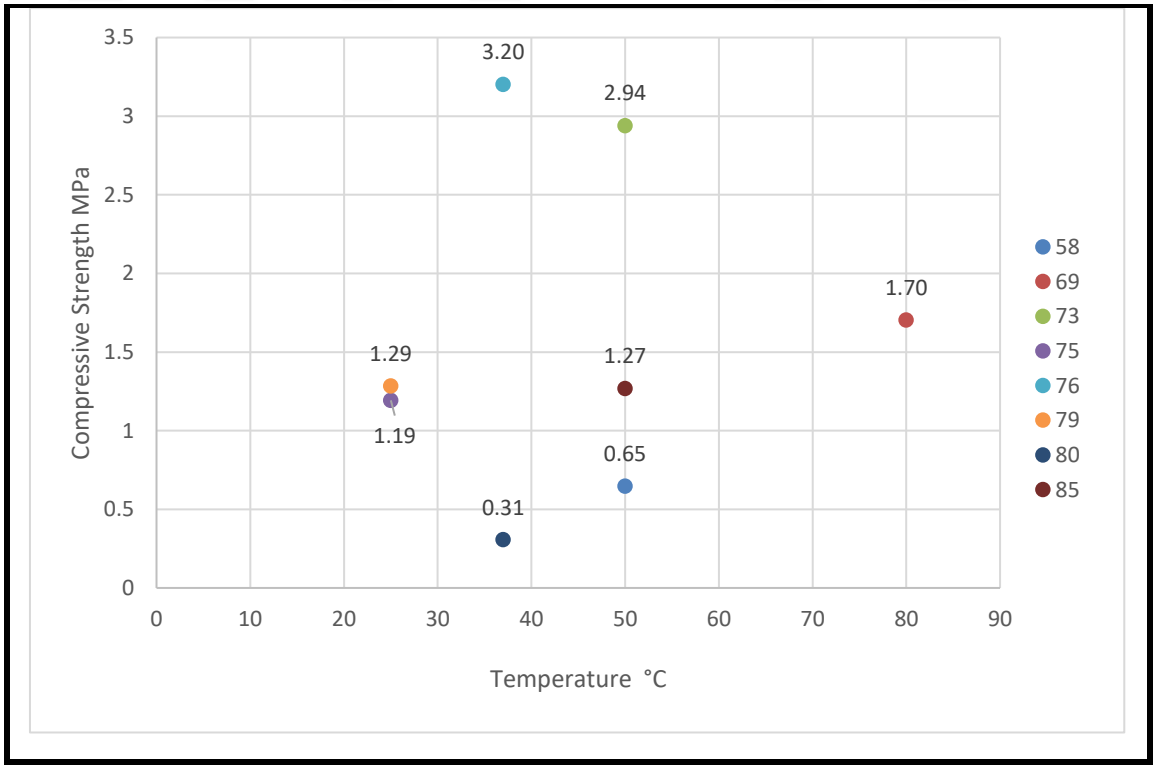

Figure 3.47. The compressive strength of the cements in relation to setting temperature.

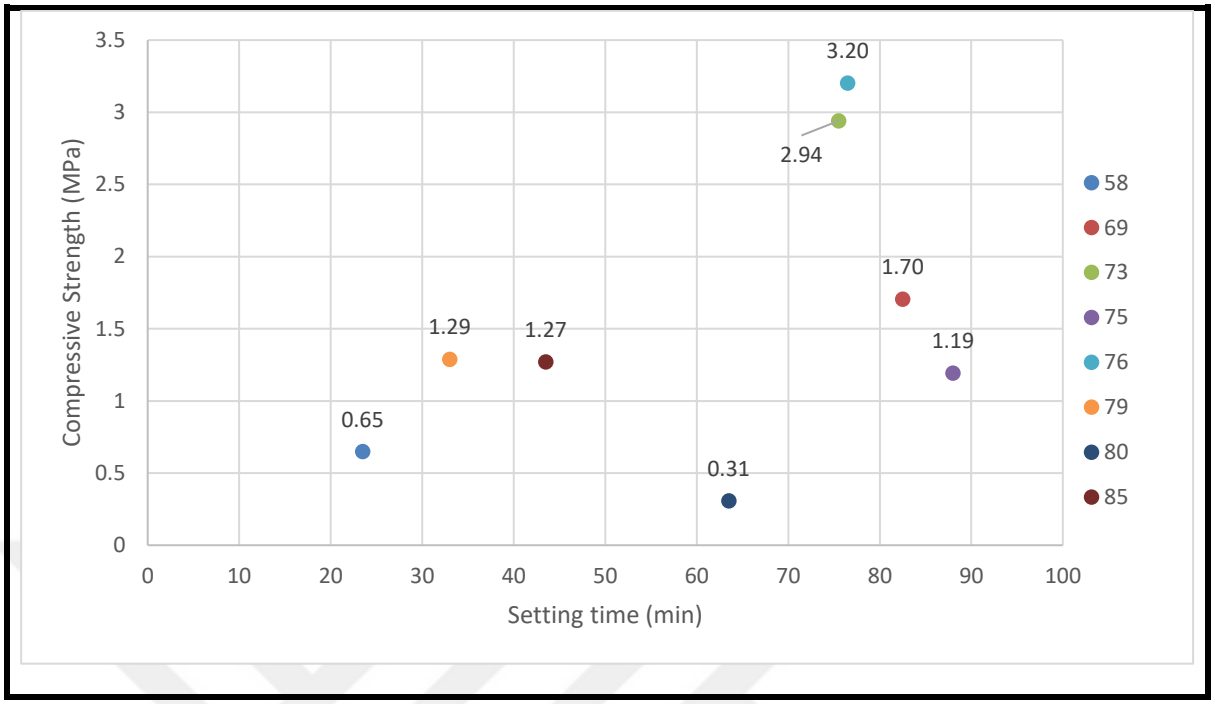

Figure 3.48. The compressive strength of the cements in relation to setting time.

According to Figure 3.49., higher gelatin amount displayed higher compressive strength, indicating that as gelatin content increased, both the compressive strength and elastic moduli increased. Bigi et al. [40] report that addition of gelatin to calcium phosphate cements favors smaller porosities than the control samples. Therefore, this results in better mechanical load distribution, enabling improved compressive strength [40]. Furthermore, Fujishiro et al. [80] reports that compressive strength of calcium phosphate cement increases relative to gelatin content up to 5 wt. percent and further gelatin addition leads to reduced compressive strength [80]. Trials with greater amount of gelatin (10 wt. percent) was also conducted in this study but these trials were eliminated due to their low mechanical strength, high setting time, and non-uniform porosity; thus, correlating with the results of Fujishiro et al. [80].

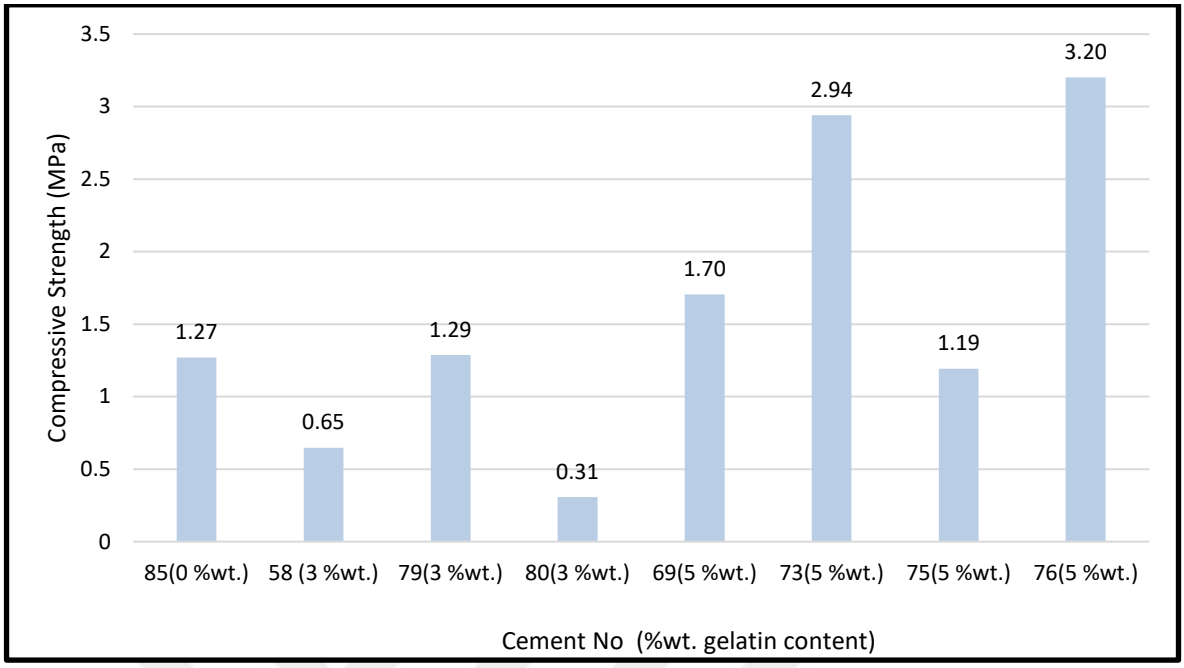

Figure 3.49. The compressive strength of the cements in relation to the gelatin content.

The effect of powder to liquid ratio on the compressive strength of a cement is demonstrated in Figure 3.50. It can be concluded that cements with P/L ratio greater than 2 result in lower compressive strength than cements with P/L ratios lower than 2.

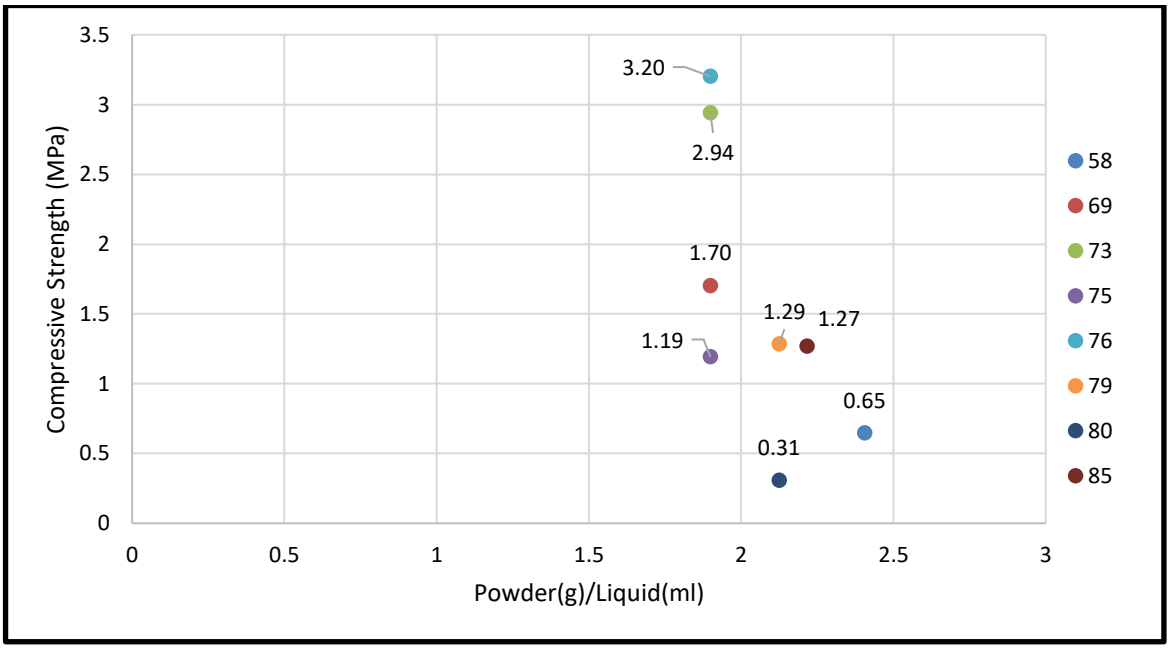

Figure 3.50. The compressive strength of the cements in relation to the powder/liquid ratio.

3.3.7. Setting Time Assesment using the Vicat Test

The setting time of cements were determined using the Vicat test device and listed in Table 3.6. Vicat test was applied according to the ADA standart (American Dental Association No.61) at room temperature and additionally, for 76C-5/37 and 80C-3/37, at 37 °C to demonstrate the effect of temperature on the setting time of the cement. For that purpose, Vicat test device was assembled in the incubator with the temperature set to 37 °C and the test was conducted according to the standart (Table 3.6). Setting time values at 25 °C for cement 76C-5/37 and 80C-3/37 were determined to be 76.5±0.5 and 63.5±0.5 min. respectively, but setting time values at 37 °C for these cements were determined to be 27.5±0.5 and 16.5±0.5 min. respectively. The study of Driessens et al. [58] indicates that higher temperature accelerates cement reaction rate and shorthens the setting time, correlating with our results [58]. Additionally, according to Brown et al., the initial dissolution of DCPA reaches maximum at 38 °C, compared with dissolution rates at 5 °C, 15 °C, and 25 °C which result in completion of reaction in 1.5, 7, 3.5, and 3.5 hours respectively [81].

Table 3.6. Setting times (min.) of cements according to Vicat test (at 25 °C).

(*Setting times (min.) according to Vicat test at 37 °C)

Cement	**Test Temperature (°C)**	**Time (min)**
58C-2/50	25	23.5
69C-5/65	25	82.5
73C-5/50	25	75.5
75C-5/25	25	88
76C-5/37	25	76.5
76C-5/37*	37	27.5

Table 3.6. (Continue'd.)

Cement	Test Temperature (°C)	Time (min)
79C-3/25	25	33
80C-3/37	25	63.5
80C-3/37*	37	16.5
85C-0/50	25	43.5

In calcium phosphate cements, setting time is related to the reaction kinetics of the reactants, which in this case the reaction rate depended on the surface area of DCPA. An increase in hydroxyapatite formation results in a decrease in DCPA, where hydroxyapatite formation is limited with the dissolution of DCPA as well as the diffusion rate of the ions, which thus controls the reaction rate [81]. Addition of distilled water increases the liquid content and solubility; thus, the reaction proceeds more rapidly, decreasing the cement setting time. Therefore, with the aim to increase solubility, reactants were crushed into very fine powder using agate mortar and pestle. As displayed in Figures 3.51 and Figure 3.52, there is an upper and lower limit to the amount of distilled water added. The amount of distilled water increases the setting time, transforming the cement from paste to slurry; on the other hand, at low water content (P/L ratio greater than 3), the cementing reaction takes places more slowly due to decreased solubility.

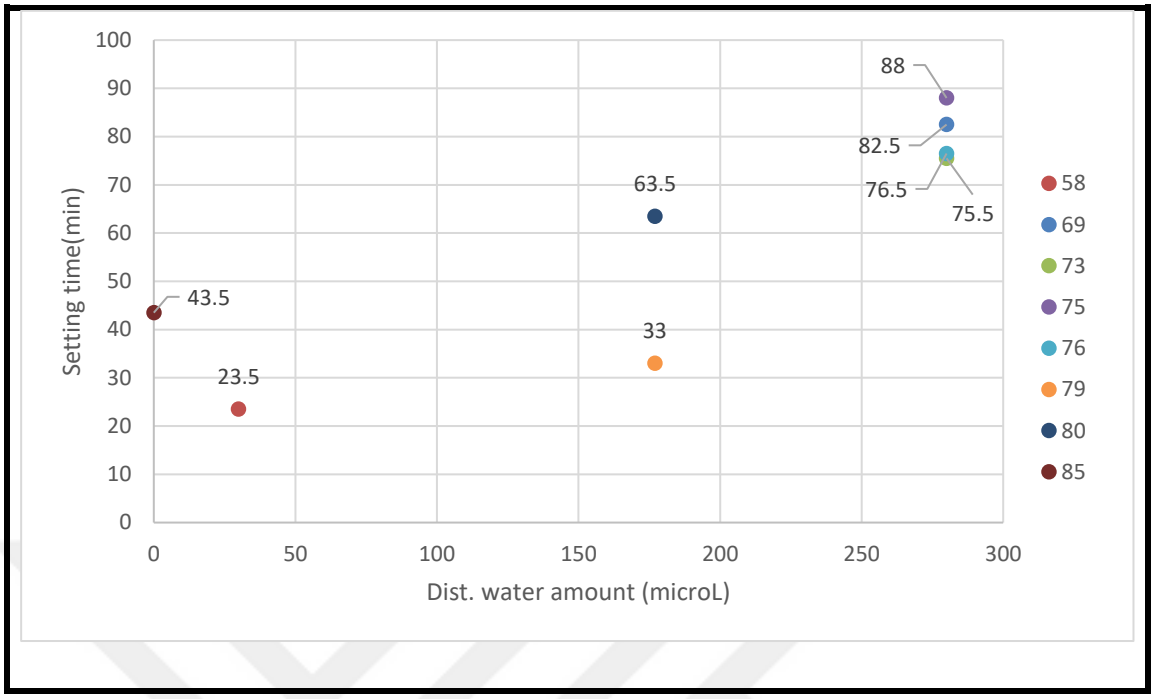

Figure 3.51. The correlation between distilled water volume and mean setting time.

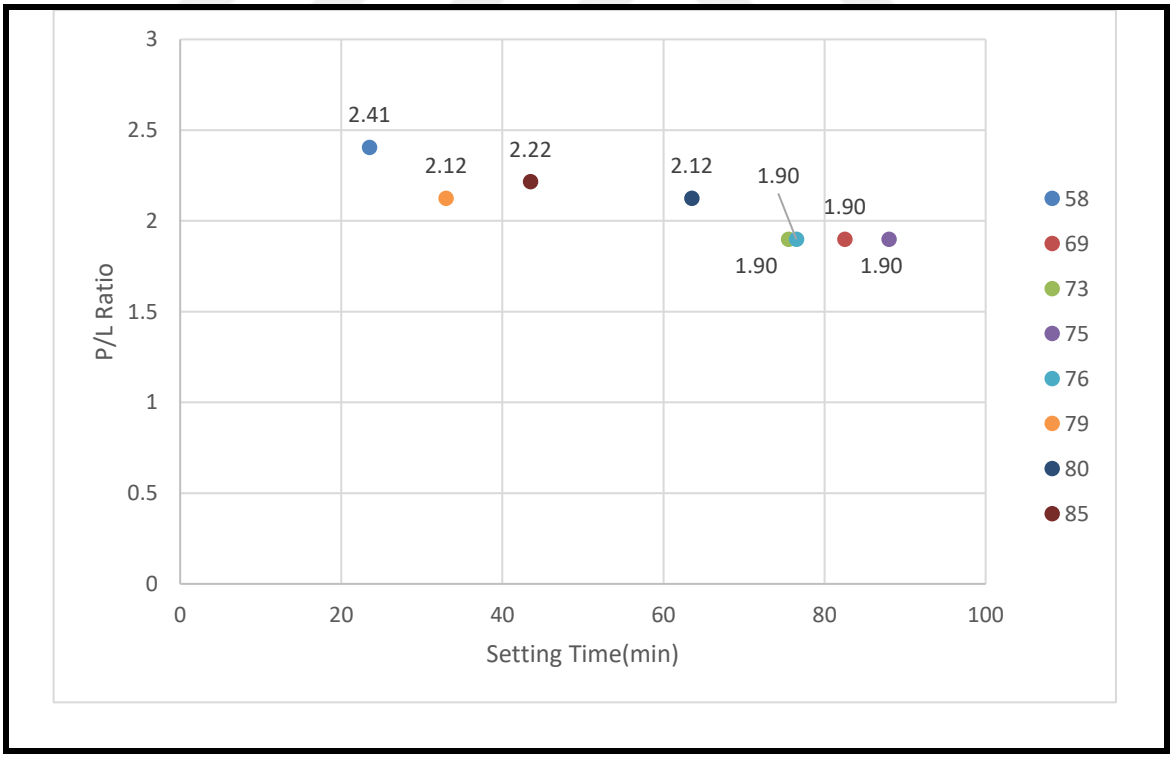

Figure 3.52. The correlation between setting time (at 25 °C) and the P/L ratio.

Following the setting time standart, all measurements were conducted at 25 °C. Cements with the only variable being temperature were expected to have similar setting times. Setting time of cements 75C-5/25, 76C-5/37, 73C-5/50 and 69C-5/65 demonstrated similar values with a difference of 5.8 min. On the other hand, for cements 79C-3/25 and 80C-3/37, the setting times were determined to be quite different from each other with a difference of 21.5 min. This large difference may have occurred as a result of the differences in $CaHPO_4$ dissolution. Differences in the dissolution and gelation may be due to the mechanical grinding process, which may thus vary the particle size of the reaction limiting reactant, i.e. $CaHPO_4$.

3.3.8. Biodegradation of Calcium Phosphate Cements

In order to better understand the chemical processes that take place during the dissolution of cement samples, it would be useful to understand Ca-P solubility which affects their dissolution, precipitation, hydrolysis, and phase transformation. Solubility is defined as the amount of solid dissolved in a volume of solution. A three component Ca-P solution may be comprised of either $Ca(OH)_2$-H_3PO_4-H_2O or CaO-P_2O_5-H_2O system [82]. Solubility is related to compound stability in acidic or basic solutions, e.g. formation of PO_4^{3-}, HPO_4^{2-} or $H_2PO_4^-$ ions depending on solution pH. All calcium phosphate compounds are more soluble as the pH decreases, with solubility changing more slowly for the more acidic salts, DCPD and DCPA, than for the more basic salts,TTCP, HA and the α/β TCPs. Solubility data, using the dissociation constants of $Ca(OH)_2$-H_3PO_4 (Table 3.7.), can be used to calculate the K_{sp} value.

The dissolution reaction of hydroxyapatite may be expressed as

$$Ca_5(PO_4)_3OH\ (solid) \Leftrightarrow 5\ Ca^{+2} + 3\ PO^{-4} + OH \quad (1)$$

$$Ca_5(PO_4)_3OH\ (solid) \Leftrightarrow 5Ca(OH) + 3\ H_3PO_{4-} + 9\ H_2O \quad (2)$$

Table 3. 7. Calcium (ortho) phosphate compounds and their solubility product constants [68,82].

Compound	**Formula**	**Ca/P**	**Log(K_{sp}) at 25° C**	**Log(K_{sp}) at 37° C**
Monocalcium phosphate monohydrate	$Ca(H_2PO_4)_2$	0.5	highly soluble	highly soluble
Monocalcium phosphate anhydrous	$Ca(H_2PO_4)_2$	0.5	highly soluble	highly soluble
Dicalcium phosphate dihydrate	$CaHPO_4 \cdot 2H_2O$	1.0	6.59[3]	6.63
Dicalcium phosphate anhydrous	$CaHPO_4$	1.0	6.90[46]	7.02
Octacalcium phosphate	$Ca_8H_2(PO4)_6 \cdot 5H_2O$	1.33	96.6[47]	95.9
α-Tricalcium phosphate	α-$Ca_3(PO_4)_2$	1.5	25.5[48]	25.5
β-Tricalcium phosphate	β-$Ca_3(PO_4)_2$	1.5	28.9[49]	29.5
Hydroxyapatite	$Ca_6(PO_4)_3OH$	1.67	58.4[50]	58.6
Fluorapatite	$Ca_6(PO_4)_3F$	1.67	60.5[61]	
Tetracalcium phosphate	$Ca_4(PO_4)_2O$	2.0	38[1] to 44[2]	42.4

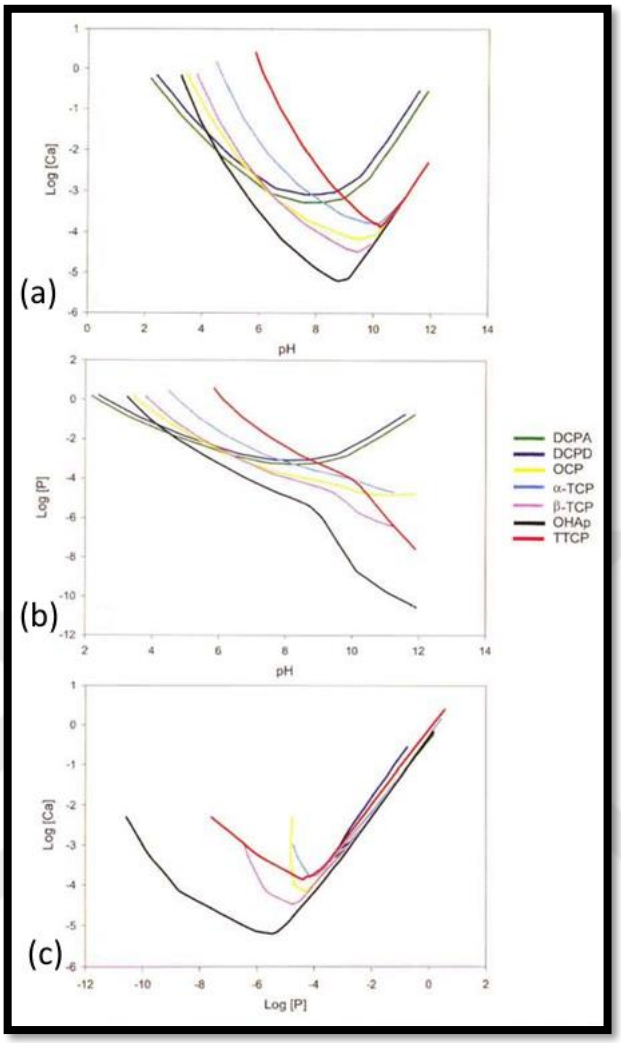

Figure 3.53. The solubility phase diagrams of (a) log [Ca] vs. pH plane; (b) log [P] vs. pH plane, and (c) log [Ca] vs. log [P] plane [82].

In the Ca-P phase diagrams (Figure 3.50), displaying ion content vs. pH, [Ca] increases with increasing pH, while [P] decreases with increasing pH except for DCPA and DCPD compounds [82]. The phase diagrams indicate that HA is the least soluble among all salts until the pH falls below approximately 4.2 where DCPA becomes the least soluble. Similarly, TTCP is the most soluble salt for pH below 3.5; above that, DCPD is the most soluble.

In this study, the cement samples were incubated in SBF for 28 days to determine the change in calcium and phosphate ion concentration (Figure 3.53a,b, Table 3.7) and their ratios (Figure 3.53c, Table 3.7). Calcium concentration [Ca] of the calcium phosphate cements are given in Figure 3.50a. As seen, initial calcium concentrations were on the increase during the 2 days for all cements except for 58. All cements include DCPD in their structure, but

with the use of DCPA instead of DCPD in 58C-2/50, the [Ca] of 58C-2/50 was increased after 2 days. As seen in the Figure 3.54a. [Ca] was decreased after 2 days, which may explained with change in the local supersaturation. DCPD in the cement system may have affected the supersaturation because of rapid resorption of DCPD and the release of Ca ions into solution. Among all the cements, 76C-5/37 and 80C-3/37 released highest [Ca] at 77.16 and 73.96 μg/ml respectively. Additionally, cement 58C-2/50 and 85C-0/50 showed the lowest [Ca] at 2.98 and 3.55 μg/ml respectively.

Phosphate concentration [P] of the cements can be divided into two groups according to their initial dissolution rate (Figure 3.54b). In the first group of cements (58C-2/50, 75C-5/25, 76C-5/37, 80C-3/37) [P] was increased as a function of a time, on the other hand, the [P] of the group two cements (69C-5/65, 73C-5/50, 79C-3/25) was either decreased or did not fluctuate on day 2. Even though those cements consisted of similar reactants there are some chemical and morphological differences between them. After day 7, the increase in [P] of the cements may indicate supersaturation of solution for DCPD. After day 14, [P] of the cements were decreased except for 58C-2/50 and 75C-5/25. Among all, 85C-0/50 demonstrated highest phosphate concentration (0.79 μg/ml) and 80C-3/37 was the lowest (0.04 μg/ml).

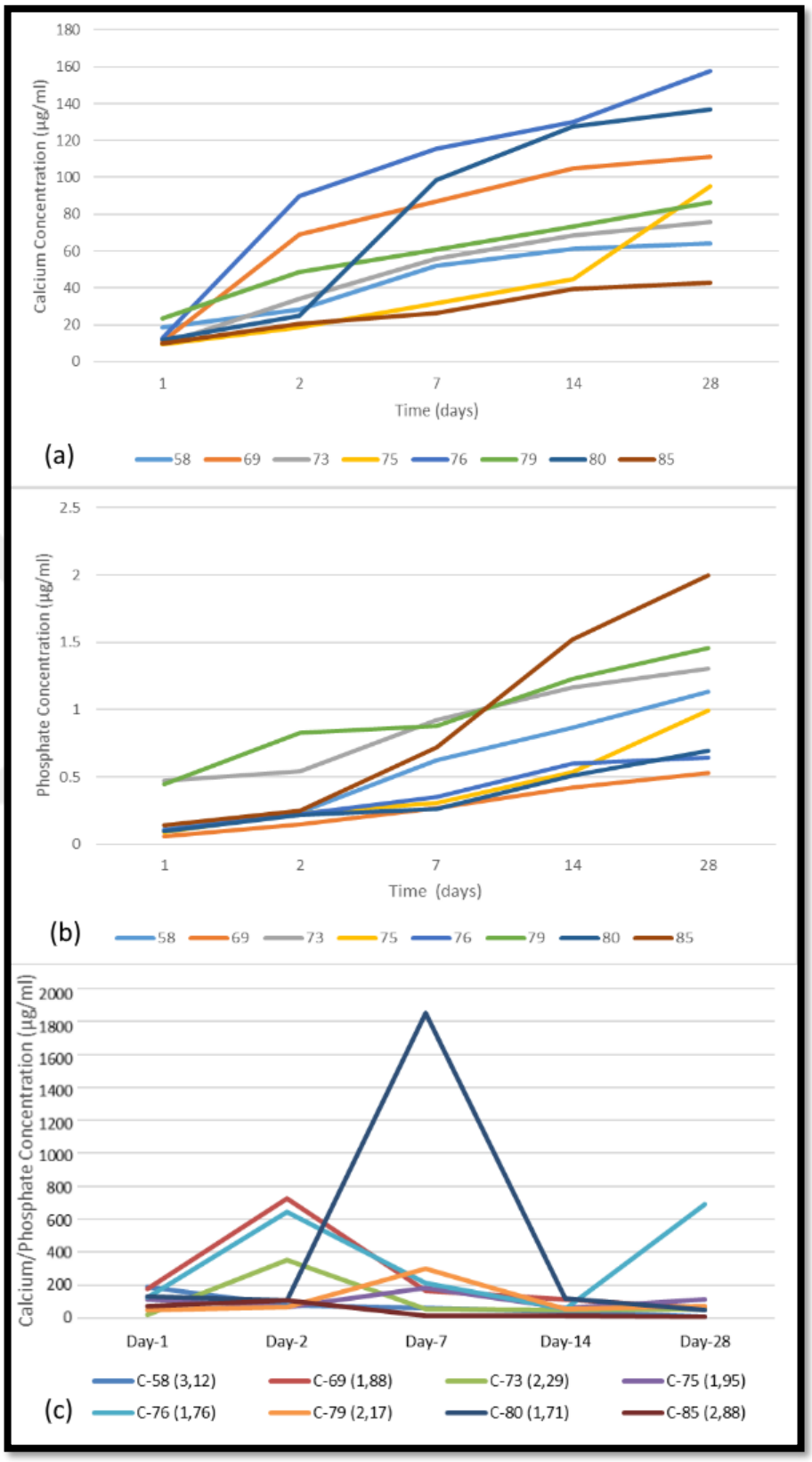

Figure 3.54 (a) Calcium concentration, (b) Phosphate concentration, and (c) Calcium/Phosphate ratios of cement samples with 28 day incubation at 37 °C.

Table 3.8. Calcium and phosphate concentration of cement samples.

Cement	**Incubation Length**				
58C-2/50 (Ca/P: 3.12)	**Day-1**	**Day-2**	**Day-7**	**Day-14**	**Day-28**
Calcium Concentration(µg/ml)	18.71	9.76	23.4	9.11	2.98
Phosphate Concentration(µg/ml)	0.10	0.12	0.39	0.23	0.26
Ca/P Ratio (concentration)	187.1	81.3	60	39.6	11.4
69C-5/65 (Ca/P: 1.88)					
Calcium Concentration(µg/ml)	10.77	58.26	18.12	17.51	6.42
Phosphate Concentration(µg/ml)	0.06	0.08	0.11	0.15	0.10
Ca/P Ratio (concentration)	179.5	728.5	164.7	116.7	64.2
73C-5/50 (Ca/P: 2.29)					
Calcium Concentration(µg/ml)	9.12	24.76	21.77	12.67	7.35
Phosphate Concentration(µg/ml)	0.47	0.07	0.38	0.24	0.13
Ca/P Ratio (concentration)	19.4	353.7	57.2	52.7	56.5
75C-5/25 (Ca/P: 1.95)					
Calcium Concentration(µg/ml)	9.12	9.435	13.02	13.31	50.18
Phosphate Concentration(µg/ml)	0.08	0.14	0.07	0.22	0.45
Ca/P Ratio (concentration)	114	67.3	186	60.5	111.5
76C-5/37 (Ca/P: 1.76)					
Calcium Concentration(µg/ml)	12.8	77.16	25.69	14.58	27.55
Phosphate Concentration(µg/ml)	0.10	0.12	0.12	0.25	0.04
Ca/P Ratio (concentration)	128	643	214	58.3	688.7
79C-3/25 (Ca/P: 2.17)					
Calcium Concentration(µg/ml)	23.23	25.31	11.96	12.76	13.21
Phosphate Concentration(µg/ml)	0.44	0.383	0.04	0.24	0.18
Ca/P Ratio (concentration)	52.7	66	299	53.1	73.3
80C-3/37 (Ca/P: 1.71)					
Calcium Concentration(µg/ml)	11.99	12.68	73.96	28.9	9.48
Phosphate Concentration(µg/ml)	0.09	0.12	0.04	0.24	0.18
Ca/P Ratio (concentration)	133.2	105.6	1849	120.4	52.6

Table 3.8. (Continue'd.)

Cement	**Incubation Length**				
85C-0/50 (Ca/P: 2.88)	**Day-1**	**Day-2**	**Day-7**	**Day-14**	**Day-28**
Calcium Concentration(μg/ml)	9.705	10.74	6.04	12.88	3.55
Phosphate Concentration(μg/ml)	0.13	0.10	0.47	0.79	0.47
Ca/P Ratio (concentration)	74.6	107.4	12.8	16.3	7.55

In the dissolution study of Piyala et al., the pH value fluctuates around neutrality. At day 2, the solution pH starts from 7.4, varies between 7.35 and 7.55 upto day 12, after then a sharp decrease in solution pH is observed in all samples, fluctuating between 7.15 and 7.3 till day 28 and stabilizing at pH 7.2 [77]. In our study as well, the pH fluctuated around neutrality during the course of 28 days.

As expected, the addition of SBF ions destabilized the cement sample at the beginning of the dissolution test, displaying the expected increase in [Ca] and [P] observed at sample-based differing time points, leading to the solution saturation as a function of time. The large Ca/P ratio obtained was reasoned to be due to the dissolution of HA and formation of DCPD ions around the point of neutrality. The dissolution of HA, formation of HPO_4^{-2} ions, will lead to the formation of DCPD, one of the main components of our cement system by affecting the pH and thus solution supersaturation for DCPD as well as CDHA, where, at a specific pH, presence of the respective ions may supersaturate the solution for the formation or prevention of apatite formation [82,83].

In addition, as substitutional ions, such as H^+, Na^+, Mg^{2+}, Cl^-, F^-, and CO_3^{2-} can be structurally incorporated in HA in significant amounts, leading structural imperfections and variations in solubility. Being an essential ion in the body, HCO_3^- and CO_3^{-2} are incorporated in hard tissues. Presence of carbonate in carbonated apatite dissolution kinetics were found to be governed by not the carbonate content, but by HA surface complex, the crystallinity of the mineral and crystal microstrain obtained using the Rietveld method [82].

The variation in ion composition and thus the solubility of synthetic carbonated apatites and biological apatites may be explained by the two approaches explaining the solid-solution equilibrium: (a) metastable equilibrium solubility (MES), where the rapid dissolution of a crystalline material, leading to a solution composition where dissolution does not occur,

despite the degree of saturation being significantly below that required for crystal growth, (b) dissolution-governing surface complex, which is formed at the crystal surface in contact with the ions in solution, determining the functional form of the dissolution driving force [82].

From the point of view of chronomatching of implant dissolution with mineral deposition, HA solubility can be used to modulate mineralization of tooth enamel, where the dissolution of HA would make the solution super saturated with respect to DCPD, and DCPD would precipitate, increasing the solution pH from the initial value of 2.1 to a higher value of 3.5, thus lowering the [Ca] and [P] in solution and producing a net increase in mineral content on the enamel surface [82].

In the study of Cerruti et.al., changes in the material/liquid ratio are expected to modify apatite formation. Any changes in the experimental settings could prove a change in the outcome of the results [84]. For our case, cements were prepared with different ratios, different curing temperatures, different liquid to powder ratios. As a result of that variety of samples, its not suprise to get unexpected datas. The SBF ions have destabilized the system, leading to the dissolution of the cements, and formation of new compounds with lower Ca/P ratio, and thus presence of a considerably high [Ca^{+2}]concentration. Ion concentration of the SBF have been given in section 2.1.4.

As a final note on this subject, the Ca/P ratio is a rational indicator of the rate of dissolution of bone cement to be used for dissolution-deposition chronomatched implantation. As early and fast resorption of cement would lead to fibrous tissue formation and absence of osteoinduction by the nanocrystalline HA of the implant, from this perpective, 75C-5/25, 79C-3/25 and 80C-3/37 demonstrate delayed dissolution; while 69C-5/65, 73C-5/50 and 76C-5/37 early dissolution. 76C-5/37 displays a second wave of disolution at the end of the experiment on day 28 (Figure 3.54c).

There may be various factors that affect the ion concentration as a result of dissolution, such as the container type which may lead to apatite nucleation, changes in the SBF medium supersaturation, incubation conditions and variety of samples. According to the study of Bohner et al. bioglass containers may increase alkalinity by releasing Ca^{+2} ions when introduced to SBF and leading to apatite nucleation. Additionally, experimental dynamics may take a role on the reaction kinetics. According to study of Vallet et al. [85] using a

dynamic incubation rather than the static incubation postpones the apatite formation. In this study, laboratory experiment was conducted with a static incubator. Additionally, Vallet states that rough and scratched surfaces may provoke apatite formation [85]. In this study, although plastic round bottom falcon tubes were used, the tube surfaces may not be smooth on the bottom, leading to nucleation, which may have affected our results [86].

3.3.9. Histological Evaluation

The results of this pilot in-vivo implantation study indicate that the cement samples, 76C-5/37 and 80C-3/37, have been able to induce satisfactory bone formation at the end of the 8-week study (Table 3.9).

Table 3. 9. Histological scores of all test subjects

Group (Subject)	Side-cement	Fibrous tissue	Cartilage	Newly formed bone	Total Score
Control 4 wk (1)	L-autograft	9	0	0	9
	R-autograft	9	0	0	9
Control 8 wk (3)	L-autograft	7	0	1	8
	R-autograft	7	0	2	9
Test 4 wk (4)	L-76C-5/37	9	0	2	11
	R-80C-3/37	9	0	1	10
Test 4 wk (5)	L-76C-5/37	8	1	1	10
	R-80C-3/37	8	0	1	9
Test 8 wk (2)	L-76C-5/37	9	1	0	10
	R-58C-2/50	9	1	1	11
Test 8 wk (6)	L-76C-5/37	7	3	5	15
	R-80C-3/37	9	4	6	19

The H&E stained histological images of the 4-week control animal are given in Figures 3.55 and 3.56, where osteogenesis around the defect has progressed to the point of fibrous tissue formation with capillary budding.

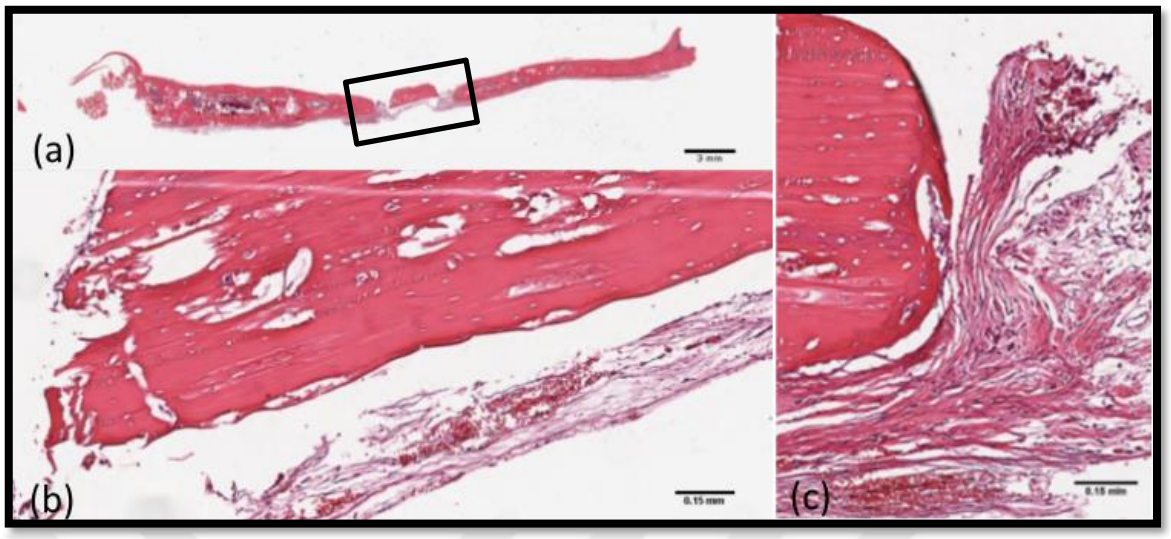

Figure 3.55. Control-1 (Subject-1, L, 4-wk) (a) the calvarial tissue, the rectangular frame marks the 3 mm. cranial bone defect site, (b-c) larger images of the defect.

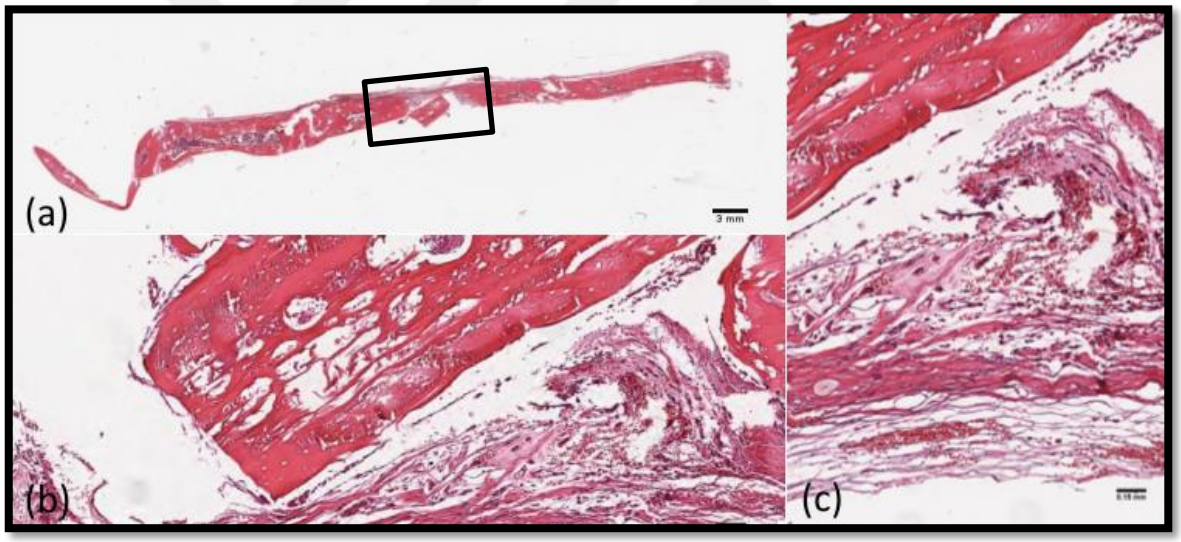

Figure 3.56. Control-1 (Subject-1, R, 4-wk) (a) the calvarial tissue, the rectangular frame marks the 3 mm. cranial bone defect site, (b-c) larger images of the defect.

The H&E stained histological images of the 8-week control animal are given in Figures 3.57. and 3.58, where osteogenesis has progressed from fibrous tissue to new bone formation via endochondral ossification.

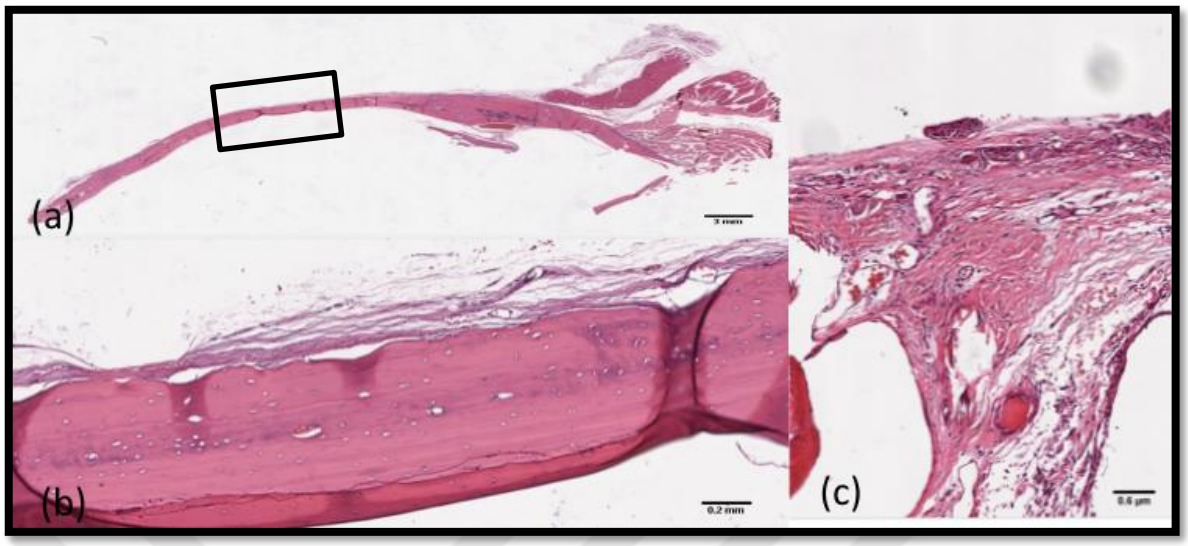

Figure 3.57. Control-2 (Subject-3, L, 8-week) (a) the calvarial tissue, the rectangular frame marks the 3 mm. cranial bone defect site, (b-c) larger images of the defect.

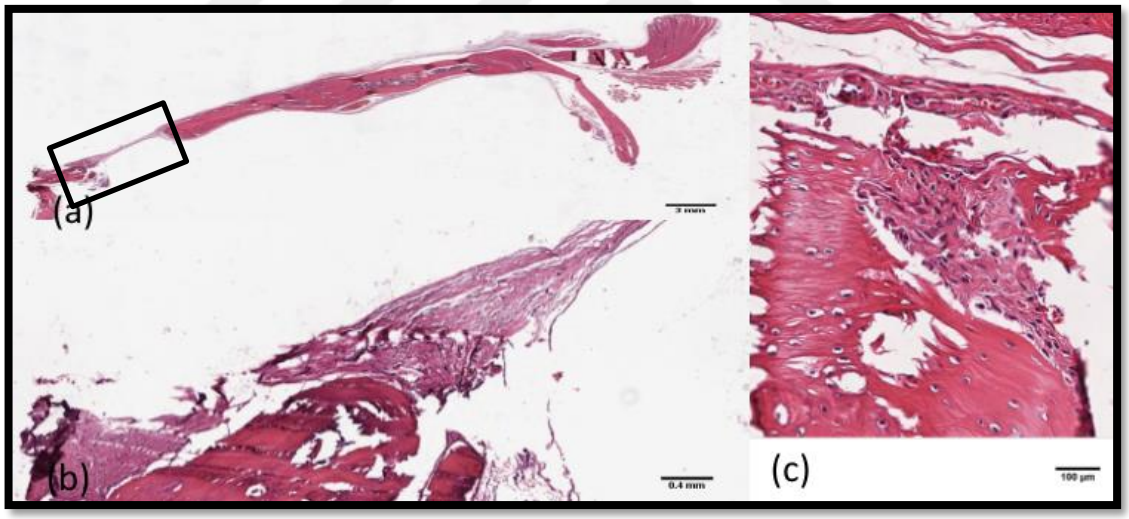

Figure 3.58. Control-2 (Subject-3, R, 8-wk) (a) the calvarial tissue, the rectangular frame marks the 3 mm. cranial bone defect site, (b-c) larger images of the defect.

The H&E stained histological images of the 4-week test animal are given in Figures 3.59. and 3.60, where osteogenesis has progressed from fibrous tissue formation, via endochondral ossification to new bone tissue formation.

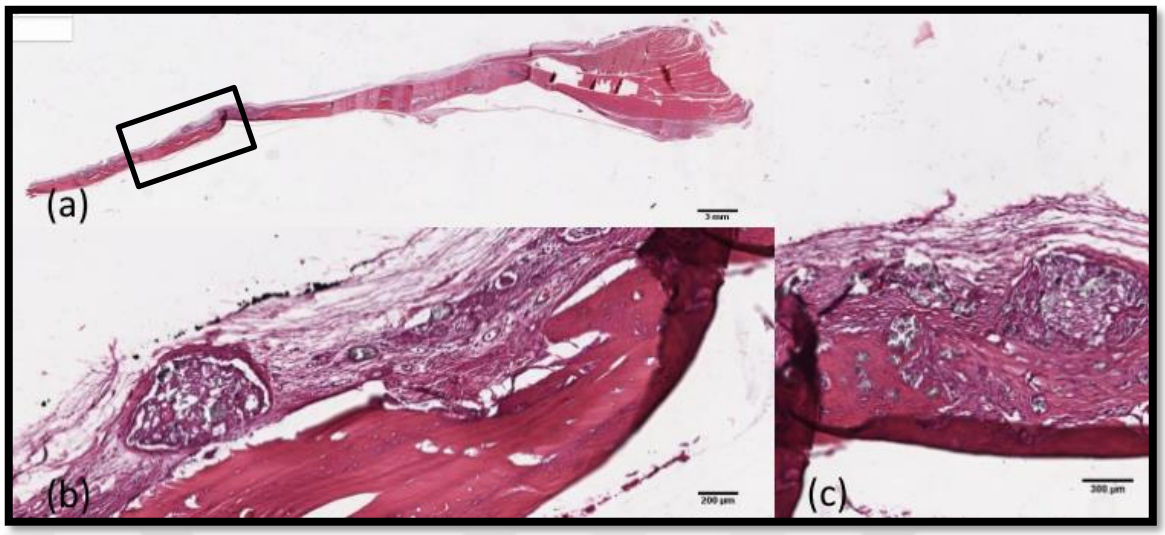

Figure 3.59. Test Subject-4 (76C-5/37, L, 4-wk) (a) the calvarial tissue, the rectangular frame marks the 3 mm. cranial bone defect site, (b-c) larger images of the defect.

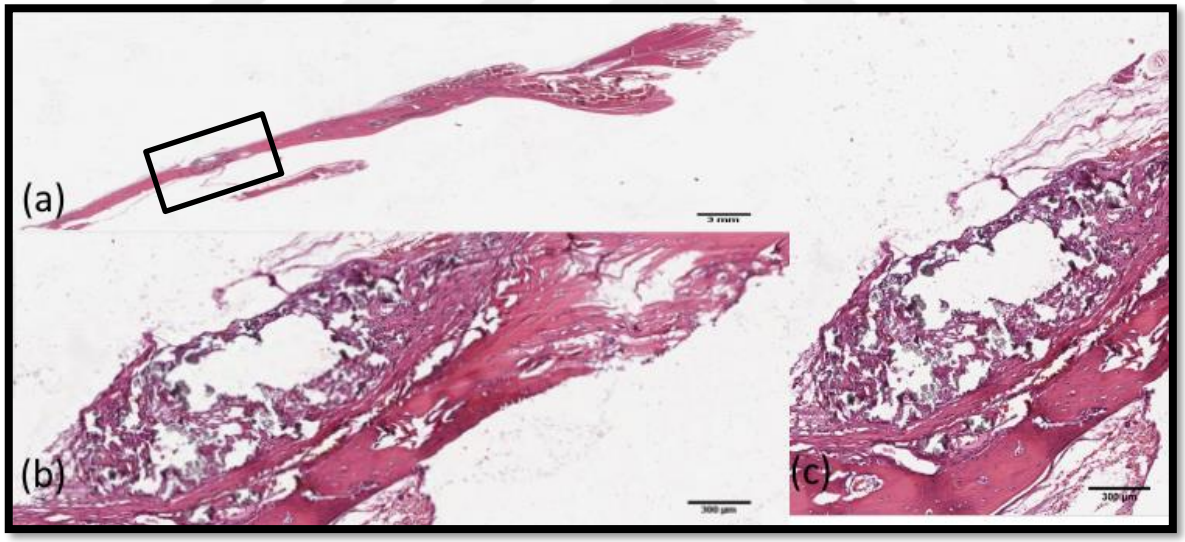

Figure 3.60. Test Subject-4 (80C-3/37, R, 4-wk) (a) the calvarial tissue, the rectangular frame marks the 3 mm. cranial bone defect site, (b-c) larger images of the defect.

The H&E stained histological images of the 4-week test animal are given in Figures 3.61. and 3.62, where osteogenesis has progressed from fibrous tissue formation via endochondral ossification to new bone tissue formation.

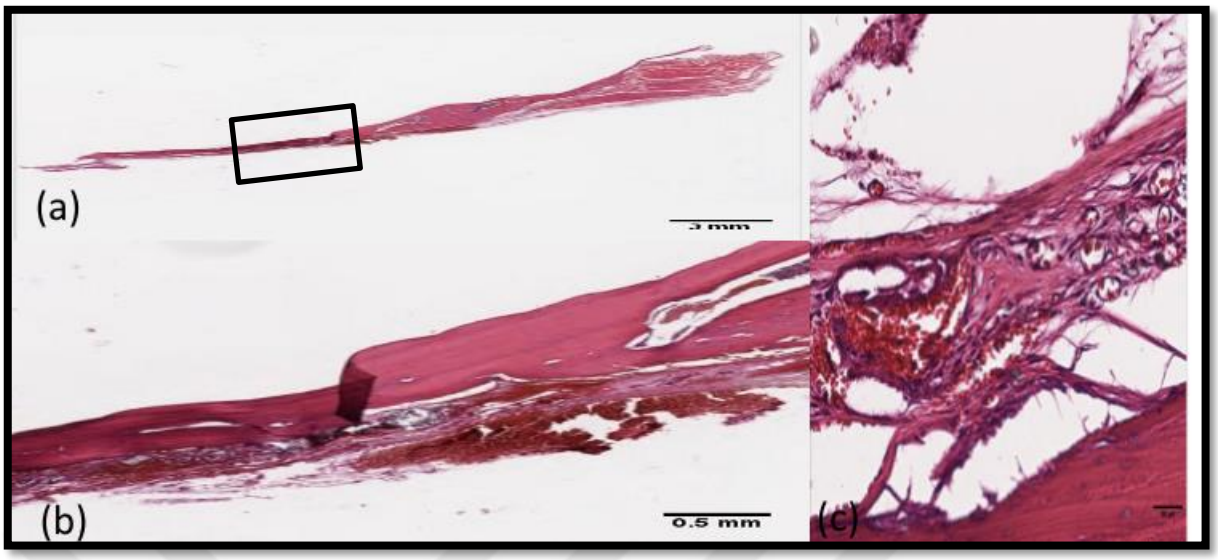

Figure 3.61. Test Subject-5 (76C-5/37, L, 4-wk) (a) the calvarial tissue, the rectangular frame marks the 3 mm. cranial bone defect site, (b-c) larger images of the defect.

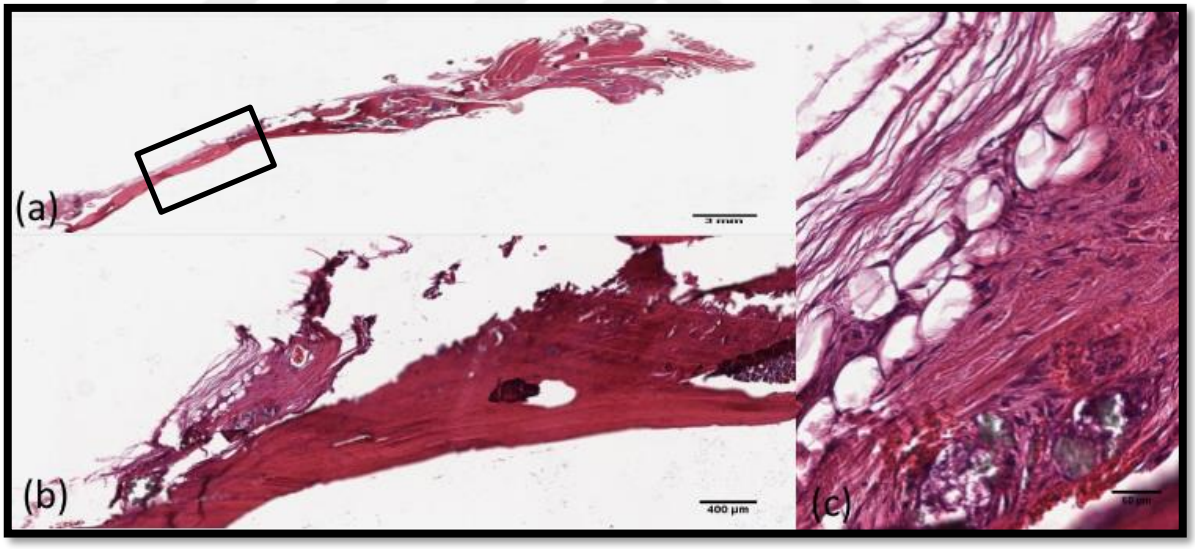

Figure 3.62. Test Subject-5 (80C-3/37, R, 4-wk) (a) the calvarial tissue, the rectangular frame marks the 3 mm. cranial bone defect site, (b-c) larger images of the defect.

The H&E stained histological images of the 8-week test animal are given in Figures 3.63. and 3.64, where osteogenesis has progressed from fibrous tissue formation via endochondral ossification to new bone tissue formation.

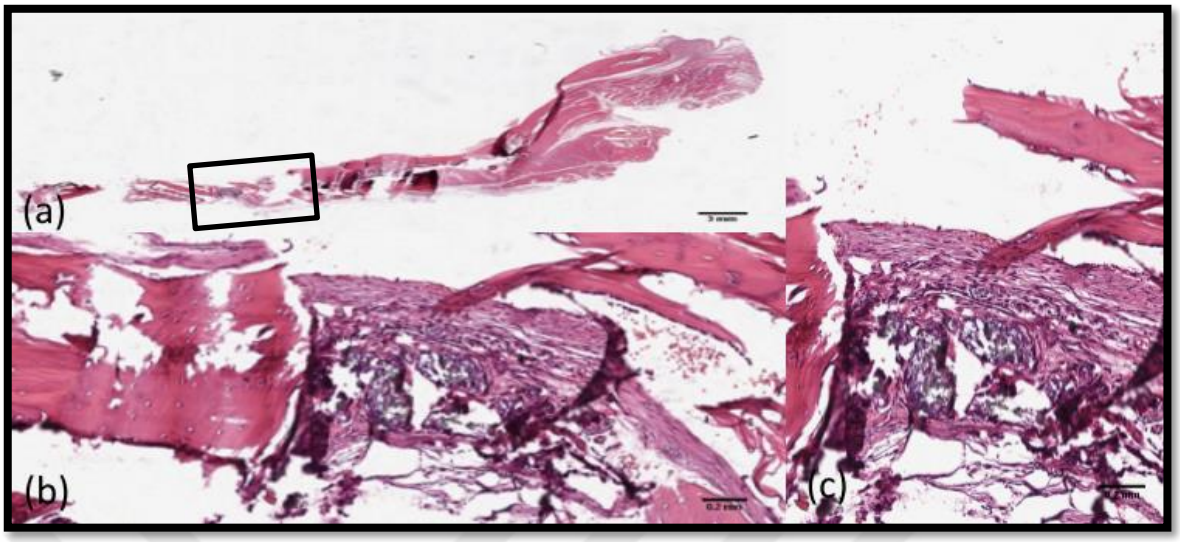

Figure 3.63. Test Subject-2 (76C-5/37, L, 8-wk) (a) the calvarial tissue, the rectangular frame marks the 3 mm. cranial bone defect site, (b-c) larger images of the defect.

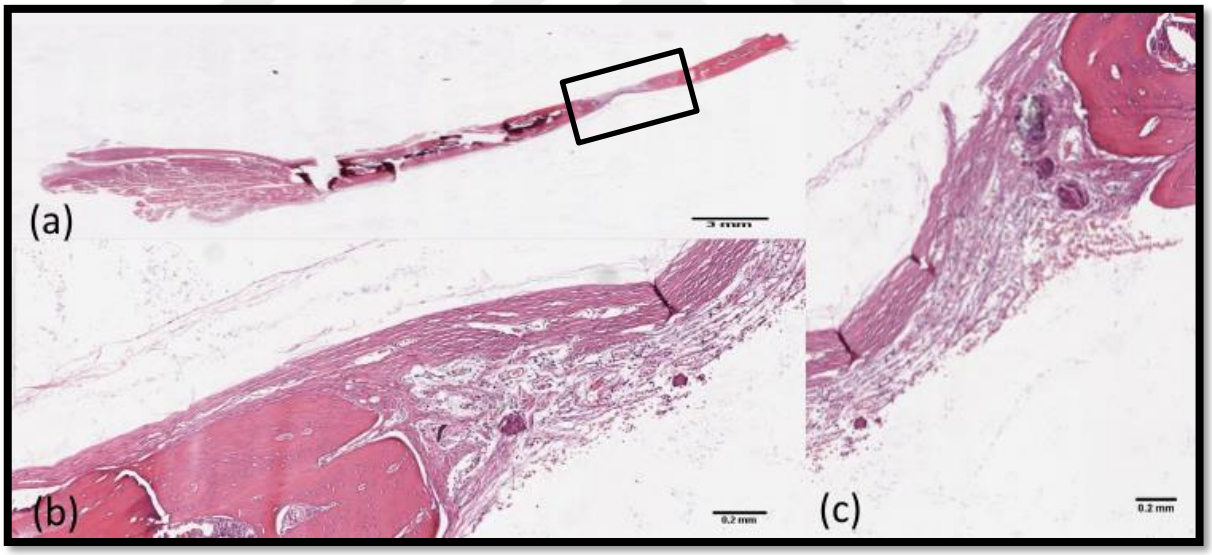

Figure 3.64. Test Subject-2 (58C-2/50, R, 8-wk) (a) the calvarial tissue, the rectangular frame marks the 3 mm. cranial bone defect site, (b-c) larger images of the defect.

The H&E stained histological images of the 8-week test animal are given in Figures 3.65. and 3.66, where osteogenesis has progressed from fibrous tissue formation via endochondral ossification to new bone tissue formation.

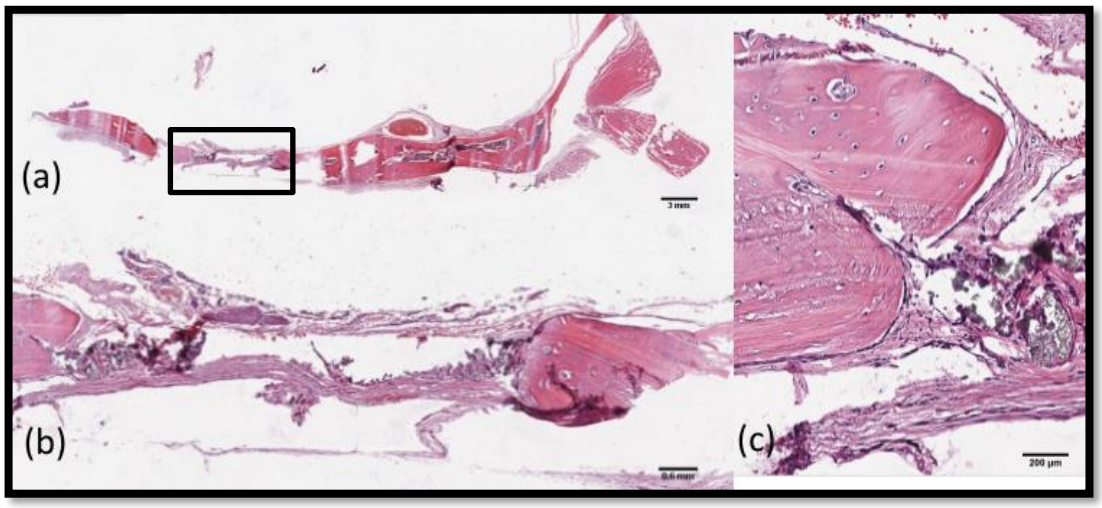

Figure 3.65. Test Subject-6 (76C-5/37, L, 8-wk) (a) the calvarial tissue, the rectangular frame marks the 3 mm. cranial bone defect site, (b-c) larger images of the defect.

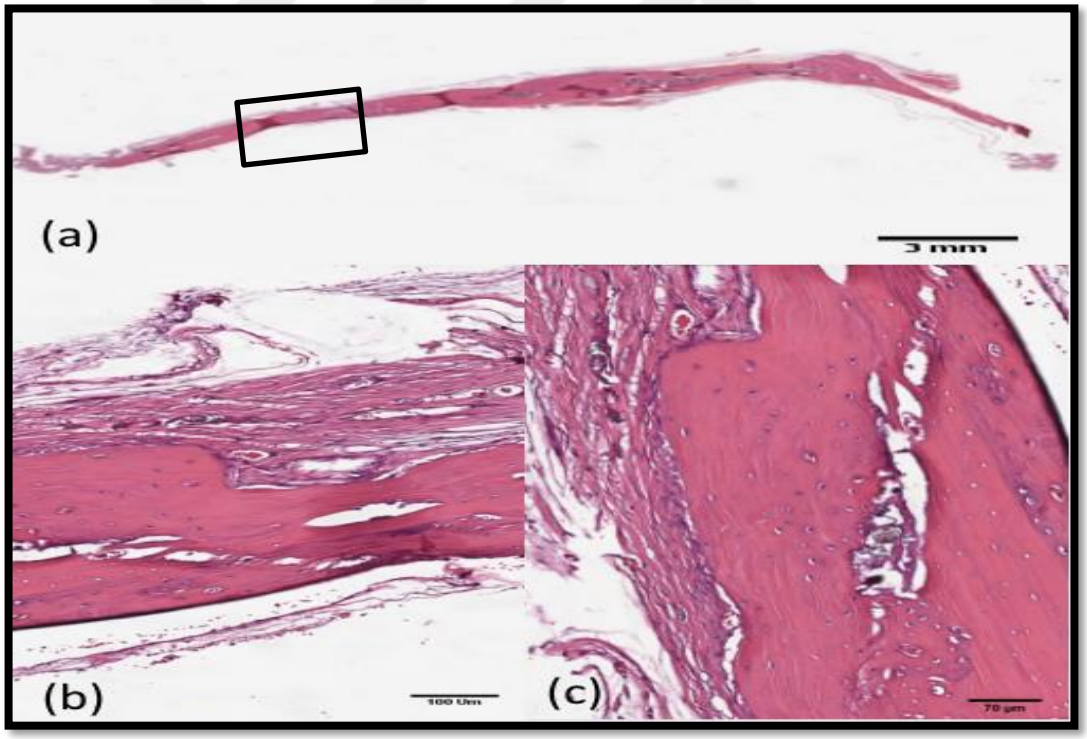

Figure 3.66. Test Subject-6 (80C-3/37, R, 8-wk) (a) the calvarial tissue, the rectangular frame marks the 3 mm. cranial bone defect site, (b-c) larger images of the defect.

4. CONCLUSIONS

In this study, gelatin and silk-fibroin based calcium phosphate cements for the treatment of non-load bearing bones in orthopedic and craniofacial defects were fabricated. For that purpose, cements were prepared with different ratios 1:1 and 1:2 molar ratio of TTCP and DCPD. Additionally, variables like temperature, cation type, gelatin ratio, and water ratio were studied in different formulations. The cements were produced, characterized and correlated with the effects of these variables.

FTIR and XRD analyses were perfomed to investigate HA formation in the cement systems. According to these results, CDHA formation was observed in all the cement systems but in 75C-5/25, 79C-3/25, 81C-3/50NaH, 83C-3/50NCH, and 85C-0/50 TTCP and DCP traces were found as well. It can be concluded as, HA formation in these cements were not fully completed.

Contact angle values of the cements were found in the range of 8.0°-77.72°, and all the cements were hydrophilic. 85C-0/50 was the most hydrophilic cement among the all while 84C-3/50NCL4 was the most hydrophobic.

Cements 75C-5/25, 76C-5/37, 73C-5/50, 69C-5/65, and 70C-5/80, were prepared with same formulation but at different temperatures at 25°, 37 °C, 50 °C, 65 °C, and 80 °C respectively. Considering the effect of temperature on the porosity of the cements, 37 °C was the most suitable temperature for the cements that prepared with $CaCO_3$ salt because of the effect of temperature on the solubility of a salt. Cements with different salts were also studied and that was verified again different temperatures are required for different salts due to their solubility. For instance, Na_2CO_3 has better solubility at the range of 40-50 °C on the other hand, $CaCO_3$ has better solubility at 37 °C [78].

Cements with different water content but with same formulations indicates that, porosity of the cements with a high water content that prepared with $CaCO_3$ has better porosity. Water content of the cements with Na_2CO_3 salt showed different results than the cements with $CaCO_3$ salt. 58C-2/50 with low water content (30 µl) showed better porosity (60 percent) rather than the 81C-3/50NaH and 82C-3/50NaL (2 and 5 percent, respectively) with high water content (402 and 281 µl respectively). Minimum acceptable porosity of the calcium

phosphate cement is around 25 percent and 58C-2/50, 76C-5/37 and 83C-3/50NCH fullfills the requirement for the miniumum porosity [87].

The compressive strength and Young's Modulus values of the CPC's were in the range of 0.31±0.17–3.2±1.12 MPa and 25-70 MPa respectively. Cement 76C-5/37 was demonstrated highest compressive strength while cement 80C-3/37 was the lowest. Compressive strength of the cranium is around 70MPa [88]. These compressive strength values are low when compared the compressive strength of the cranium but it can accepted for the low-load bearing implantations and substition materials for the implants.

Setting time measurements were conducted at 25 °C and for cement 76C-5/37 and 80C-5/37 it was also measured at 37 °C. Setting time of the cements were varied in the range of 23.5-88 minutes at 25 °C. Setting time of 76C-5/37 and 80C-3/50 at 37° were found 27.5 and 16.5 minutes respectively, while they set in 76.5 and 63.5 minutes at 25 °C. Increase on the temperature leads higher initial dissolution rate of $CaHPO_4$ and reaction takes place more rapidly [81]. With respect to that setting time of the cements shortens.

Samples selection were performed considering the setting time, Ca/P ratio, biodegradation rate, contact angle, compressive properties of the cements. Therefore, 76C-5/37, and 80C-5/37 was picked for the implantation in-vivo. According to histological scoring 4 week cements 76C-5/37 and 80C-5/37 were gathered 9 for fibrous tissue formation and 2 for new bone formation and 9 for fibrous tissue, and 1 for new bone formation respectively. Additionly 8-week 76C-5/37 and 80C-5/37 were gathered 1 point for fibrous tissue formation, 3 points for cartilage formation, and 5 points for new bone formation, and 1 point for fibrous tissue, 4 points for cartilage formation and 6 points for new bone formation respectively. In-vivo experiments were indicated the cements 76C-5/37 and 80C-5/37 were not toxic and supporting the new bone formation in the bone tissue.

5. FUTURE WORK

As a future study, a syringe can be designed to ease the application and mixing process. For such a invention a sprial shaped mechanism can be inserted into syringe and mixing can be completed mechanically inside the syringe. Additionally, studies on the rheological properties and injectability of the cement can be conducted as future study. The cement can be studied on a larger group of animals such that the statistical analysis can be carried out.

REFERENCES

1. Reznikov N, Shahar R, Weiner S. Bone hierarchical structure in three dimensions. *Acta Biomaterialia*. 2014;10(9):3815–26.

2. Mbuyi-Muamba JM, Dequeker J. Biochemical anatomy of human bone: Comparative study of compact and spongy bone in femur, rib and iliac crest. *Acta Anatomica*. 1987;128(3):181–7.

3. Khurana JS. Bone pathology. *Bone Pathology*. 2009:1–416.

4. Trueta J.. Studies of the Development and Decay of the Human Frame. *Osteogenesis* 1968: 2–11.

5. Ratner BD, Hoffman AS, Schoen FJ, Lemons JE. A History of Biomaterials Artificial Hearts and Organ Perfusion. *Biomaterials Science*. 2013:10-11.

6. Boskey AL. Mineralization of bones and teeth. *Elements*. 2007;3(6):385–91.

7. Shoulders MD, Raines RT. Collagen structure and stability. *Annual Review of Biochemistry*. 2009;78:929-958.

8. Ma XL, Li R, Ru L, Xu GW, Huang YP. Effect of polyaspartic acid on hydroxyapatite deposition in silk fibroin blend films. *Express Polymer Letters*. 2010;4(5):321–7.

9. Fedarko NS. Osteoblast/Osteoclast development and function in osteogenesis imperfecta: a translational approach to brittle bone disease. *Osteogenesis Imperfecta.* 2013: 45–56.

10. Gilbert SF. Principles of development in biology. *Developmental Biology.* 2007:243-7.

11. Markatos K, Tsoucalas G, Sgantzos M. Hallmarks in the history of orthopaedic implants for trauma and joint replacement. *Acta Medico-Historica Adriatica : AMHA.* 2016;14(1):161–76.

12. Precheur H V. Bone Graft Materials. *Dental Clinics of North America.*

2007;51(3):729–46.

13. Seth Greenwald A, Boden SD, Goldberg VM, Khan Y, Cato Laurencin MT, Rosier RN. This material was first published, in slightly different form. *The Journal of Bone and Joint Surgery*. 2001;83:98–103.

14. Eppley BL, Pietrzak WS, Blanton MW. Allograft and alloplastic bone substitutes: A review of science and technology for the craniomaxillofacial surgeon. *Journal of Craniofacial Surgery*. 2005;16(6):981–9.

15. Craig CL, Riekel C. Comparative architecture of silks, fibrous proteins and their encoding genes in insects and spiders. *Comparative Biochemistry and Physiology - B Biochemistry and Molecular Biology*. 2002;133(4):493–507.

16. Acharya C, Ghosh SK, Kundu SC. Silk fibroin protein from mulberry and non-mulberry silkworms: Cytotoxicity, biocompatibility and kinetics of L929 murine fibroblast adhesion. *Journal of Materials Science: Materials in Medicine*. 2008;19(8):2827–36.

17. Rudzinska MA, Vickerman K. The Fine Structure. *Special Topics and General Characteristics*. 1968;(3):217–306.

18. Keten S, Buehler MJ. Nanostructure and molecular mechanics of spider dragline silk protein assemblies. *Journal of the Royal Society Interface*. 2010;7(53):1709–21.

19. Zhang X, Bao H, Donley C, Liang J, Yang S, Xu S. Thiolation and characterization of regenerated Bombyx mori silk fibroin films with reduced glutathione. *BMC Chemistry*. 2019;13(3):1–9.

20. Meinel L, Betz O, Fajardo R, Hofmann S, Nazarian A, Cory E, et al. Silk based biomaterials to heal critical sized femur defects. *Bone*. 2006;39(4):922–31.

21. Lefèvre T, Rousseau ME, Pézolet M. Protein secondary structure and orientation in silk as revealed by Raman spectromicroscopy. *Biophysical Journal*. 2007;92(8):2885–95.

22. Minoura N, Tsukada M, Nagura M. Fine structure and oxygen permeability of silk fibroin membrane treated with methanol. *Polymer*. 1990;31(2):265–9.

23. Vepari C, Kaplan DL. Silk as a biomaterial. *Progress in Polymer Science (Oxford)*. 2007;32(8–9):991–1007.

24. Lawrence BD. Processing of Bombyx mori silk for biomedical applications. *Silk Biomaterials for Tissue Engineering and Regenerative Medicine.* 2014:78–99.

25. Gosline JM, Guerette PA, Ortlepp CS, Savage KN. The mechanical design of spider silks: From fibroin sequence to mechanical function. *Journal of Experimental Biology*. 1999;202(23):3295–303.

26. Bronzino JD. Biomedical engineering fundamentals. *Biomedical Engineering Fundamentals.* 2014:39-8.

27. Giesa T, Arslan M, Pugno NM, Buehler MJ. Nanoconfinement of spider silk fibrils begets superior strength, extensibility, and toughness. *Nano Letters*. 2011;11:5038-5046.

28. Du N, Yang Z, Liu XY, Li Y, Xu HY. Structural origin of the strain-hardening of spider silk. *Advanced Functional Materials*. 2011;2:772-778.

29. Gotoh K, Izumi H, Kanamoto T, Tamada Y, Nakashima H. Sulfated fibroin, a novel sulfated peptide derived from silk, inhibits human immunodeficiency virus replication in vitro. *Bioscience, Biotechnology and Biochemistry*. 2000;2:1664-1670.

30. Seo YK, Choi GM, Kwon SY, Lee HS, Park YS, Song KY, et al. The biocompatibility of silk scaffold for tissue engineered ligaments. In: Key Engineering Materials. 2007;7:73-76.

31. Vollrath F, Barth P, Basedow A, Engström W, List H. Local tolerance to spider silks and protein polymers in vivo. *In Vivo*. 2002;16(4):229-34.

32. Nair LS, Laurencin CT. Biodegradable polymers as biomaterials. *Progress in Polymer Science.* 2007;9:762-798.

33. Arai T, Freddi G, Innocenti R, Tsukada M. Biodegradation of bombyx mori silk fibroin fibers and films. *Journal of Applied Polymer Science*. 2004;91(4):2383–90.

34. Zuo B, Dai L, Wu Z. Analysis of structure and properties of biodegradable

regenerated silk fibroin fibers. *Journal of Materials Science*. 2006;4:3357-3361.

35. Maniglio D, Bonani W, Bortoluzzi G, Servoli E, Motta A, Migliaresi C. Electrodeposition of silk fibroin on metal substrates. *Journal of Bioactive and Compatible Polymers*. 2010;25(5):441–54.

36. Sofia S, McCarthy MB, Gronowicz G, Kaplan DL. Functionalized silk-based biomaterials for bone formation. *Journal of Biomedical Materials Research*. 2001;9:139-148.

37. Bigi A, Panzavolta S, Rubini K. Relationship between triple-helix content and mechanical properties of gelatin films. *Biomaterials*. 2004;25(25):5675–80.

38. Ward AG. The Chemical Structure and Physical Properties of Gelatin. *The Journal of Photographic Science*. 1955;3(2):60–7.

39. Yang G, Xiao Z, Long H, Ma K, Zhang J, Ren X, et al. Assessment of the characteristics and biocompatibility of gelatin sponge scaffolds prepared by various crosslinking methods. *Scientific Reports*. 2018;8(1):1–13.

40. Bigi A, Bracci B, Panzavolta S. Effect of added gelatin on the properties of calcium phosphate cement. *Biomaterials*. 2004;25(14):2893–9.

41. Hossan J, Gafur MA, Kadir MR, Mainul M. Preparation and Characterization of Gelatin- Hydroxyapatite Composite for Bone Tissue Engineering. *Bangladesh Journal of Scientific and Industrial Research.* 2014;57(01):113–22.

42. Arephin M, Islam A, Rahman AFMM, Iftekhar S, Salem KS, Sultana N, et al. Morphology, Thermal Stability, Electrical, and Mechanical Properties of Graphene Incorporated Poly(vinyl alcohol)-Gelatin Nanocomposites. *International Journal of Composite Materials*. 2016;6(6):172–82.

43. Kommareddy S, Shenoy DB, Amiji MM. Gelatin Nanoparticles and Their Biofunctionalization. *Nanotechnologies for the Life Sciences*. 2005:330-353.

44. Moreira-Gonzalez A, Jackson IT, Miyawaki T, Barakat K, DiNick V. Clinical Outcome in Cranioplasty: Critical Review in Long-Term Follow-Up. *Journal of Craniofacial Surgery*. 2003;14(2):144–53.

45. Murphy AR, Kaplan DL. Biomedical applications of chemically-modified silk fibroin. *Journal of Materials Chemistry*. 2009;19(36):6443–50.

46. Schmitz JP, Hollinger JO, Milam SB. Reconstruction of bone using calcium phosphate bone cements: A critical review. *Journal of Oral and Maxillofacial Surgery*. 1999;57(9):1122–6.

47. Jang JH, Shin S, Kim HJ, Jeong J, Jin HE, Desai MS, et al. Improvement of physical properties of calcium phosphate cement by elastin-like polypeptide supplementation. *Scientific Reports*. 2018;8(1):1–11.

48. Lim TH, Brebach GT, Renner SM, Kim WJ, Kim JG, Lee RE, et al. Biomechanical evaluation of an injectable calcium phosphate cement for vertebroplasty. *Spine*. 2002;27(12):1297–302.

49. Boger A, Wheeler KD, Schenk B, Heini PF. Clinical investigations of polymethylmethacrylate cement viscosity during vertebroplasty and related in vitro measurements. *European Spine Journal*. 2009;18(9):1272–8.

50. Gómez E, Martín M, Arias J, Carceller F. Clinical applications of Norian SRS (calcium phosphate cement) in craniofacial reconstruction in children: Our experience at Hospital la Paz since 2001. *Journal of Oral and Maxillofacial Surgery*. 2005;63(1):8–14.

51. Mahr MA, Bartley GB, Bite U, Clay RP, Kasperbauer JL, Holmes JM. Norian craniofacial repair system bone cement for the repair of craniofacial skeletal defects. *Ophthalmic Plastic and Reconstructive Surgery*. 2000;16(5):393–8.

52. Cohen MS, Whitman K. Calcium phosphate bone cement--the Norian skeletal repair system in orthopedic surgery. *AORN journal*. 1997;65(5):958–62.

53. Shie MY, Chen DCH, Wang CY, Chiang TY, Ding SJ. Immersion behavior of gelatin-containing calcium phosphate cement. *Acta Biomaterialia*. 2008;4(3):646–55.

54. Laurence CC, Takagi S, Ishikawa K. Formation of Hydroxyapatite in Cement Systems. In: Hydroxyapatite and Related Materials. *CRC Press*; 2017. p. 127–37. 1367-8

55. Driessens FCM, Boltong MG, Bermúdez O, Planell JA, Ginebra MP, Fernández E. Effective formulations for the preparation of calcium phosphate bone cements. *Journal of Materials Science: Materials in Medicine*. 1994;5(3):164–70.

56. Society B, Journal A. Absorption of Moisture by Gelatin in a Saturated Atmosphere Author (s): Charles A . Shull and S . P . Shull Published by : Botanical Society of America , Inc . Stable .2018;7(8):318–26.

57. Pleass WB. The absorption of water by gelatin. *Biochemical Journal*. 1931;25(6):1943–8.

58. Driessens FCM, Boltong MG, De Maeyer EAP, Verbeeck RMH, Wenz R. Effect of temperature and immersion on the setting of some calcium phosphate cements. *Journal of Materials Science: Materials in Medicine*. 2000;11(7):453–7.

59. Spicer PP, Kretlow JD, Young S, Jansen JA, Kasper FK, Mikos AG. Evaluation of bone regeneration using the rat critical size calvarial defect. *Nature Protocols*. 2012;7(10):1918–29.

60. Losee JE, Karmacharya J, Gannon FH, Slemp AE, Ong G, Hunenko O, et al. Reconstruction of the immature craniofacial skeleton with a carbonated calcium phosphate bone cement: interaction with bioresorbable mesh. *Journal of Craniofacial Surgery*. 2003;14(1):933.

61. Kirschner RE, Karmacharya J, Ong G, Gordon AD, Hunenko O, Losee JE, et al. Repair of the immature craniofacial skeleton with a calcium phosphate cement: Quantitative assessment of craniofacial growth. *Annals of Plastic Surgery*. 2002;49(1):33–8.

62. Jalota S, Tas AC, Bhaduri SB. Synthesis of HA-seeded TTCP (Ca 4(PO 4) 2O) powders at 1230°C from Ca(CH 3COO) 2·H 2O and NH 4H 2PO 4. *Journal of the American Ceramic Society*. 2005;88(12):3353–60.

63. Cüneyt Tas A. Synthesis of biomimetic Ca-hydroxyapatite powders at 37°C in synthetic body fluids. *Biomaterials*. 2000;21(14):1429–38.

64. Boehm A V., Meininger S, Tesch A, Gbureck U, Müller FA. The mechanical properties of biocompatible apatite bone cement reinforced with chemically

activated carbon fibers. *Materials*. 2018;11:192.

65. Data T. D8 Advance. *Office*. 2003;1–26.

66. Schneider CA, Rasband WS, Eliceiri KW. NIH Image to ImageJ: 25 years of image analysis. Nature Methods. 2012.

67. Astm. Standard specification for acrylic bone cement. *ASTM International*. 2010;F2118-10.

68. Prussia K, Dougherty E. American National Standards Institute/American Dental Association Specification No. 61 for zinc polycarboxylate cement. Council on Dental Materials, Instruments, and Equipment. *Journal of the American Dental Association (1939)*. 1980;101(4):669–71.

69. Grover LM, Knowles JC, Fleming GJP, Barralet JE. In vitro ageing of brushite calcium phosphate cement. *Biomaterials*. 2003;24(23):4133–41.

70. Colourimetric determination of phosphate [Internet]. [cited 2020 Apr 8]. Available from: http://wwwchem.uwimona.edu.jm/lab_manuals/c10expt36.html

71. Han Z, Bhavsar M, Leppik L, Oliveira KMC, Barker JH. Histological Scoring Method to Assess Bone Healing in Critical Size Bone Defect Models. *Tissue Engineering - Part C: Methods*. 2018;24(5):272–9.

72. Takagi S, Chow LC, Ishikawa K. Formation of hydroxyapatite in new calcium phosphate cements. *Biomaterials*. 1998;19(17):1593-1599.

73. Liao J, Duan X, Li Y, Zheng C, Yang Z, Zhou A, et al. Synthesis and mechanism of tetracalcium phosphate from nanocrystalline precursor. *Journal of Nanomaterials*. 2014;2014.

74. Wang HY, Zhang YQ. Processing and characterisation of a novel electropolymerized silk fibroin hydrogel membrane. *Scientific Reports*. 2014;4:1–11.

75. Utku FS, Seckin E, Goller G, Tamerler C, Urgen M. Carbonated hydroxyapatite deposition at physiological temperature on ordered titanium oxide nanotubes using pulsed electrochemistry. *Ceramics International*. 2014;40(10):15479–87.

76. Berzina-Cimdina L, Borodajenko N. Research of Calcium Phosphates Using Fourier Transform Infrared Spectroscopy. *Infrared Spectroscopy - Materials Science, Engineering and Technology*. 2012;4.

77. Wilcock CJ, Gentile P, Hatton P V., Miller CA. Rapid mix preparation of bioinspired nanoscale hydroxyapatite for biomedical applications. *Journal of Visualized Experiments*. 2017;2017(120):1–7.

78. Coto B, Martos C, Peña JL, Rodríguez R, Pastor G. Effects in the solubility of CaCO 3: Experimental study and model description. *Fluid Phase Equilibria*. 2012;324:1–7.

79. Ferrari M, Cirisano F, Morán MC. Mammalian Cell Behavior on Hydrophobic Substrates: Influence of Surface Properties. *Colloids and Interfaces*. 2019;3(2):48.

80. Fujishiro Y, Takahashi K, Sato T. Preparation and compressive strength of alpha-tricalcium phosphate/gelatin gel composite cement. *Journal of biomedical materials research*. 2001 Mar;54(4):525—530.

81. Brown PW, Fulmer M. Kinetics of Hydroxyapatite Formation at Low Temperature. *Journal of the American Ceramic Society*. 1991;74(5):934–40.

82. Zhang Y, Yokogawa Y, Kameyama T. Bimodal porous bi-phasic calcium phosphate ceramics and its dissolution in SBF solution. *Key Engineering Materials*. 2007;330-332 I:91–4.

83. Priya A, Nath S, Biswas K, Basu B. In vitro dissolution of calcium phosphate-mullite composite in simulated body fluid. *Journal of Materials Science: Materials in Medicine*. 2010;21(6):1817–28.

84. Cerruti MG, Greenspan D, Powers K. An analytical model for the dissolution of different particle size samples of Bioglass® in TRIS-buffered solution. *Biomaterials*. 2005;26(24):4903–11.

85. A. RaH mila MV-R, Departamento. Static and dynamic in vitro study of a sol-gel glass bioactivity. *Biomaterials*. 2000;22:2301–6.

86. Bohner M, Lemaitre J. Can bioactivity be tested in vitro with SBF solution?

Biomaterials. 2009;30(12):2175–9.

87. Ishikawa K, Asaoka K. Estimation of ideal mechanical strength and critical porosity of calcium phosphate cement. *Journal of Biomedical Materials Research*. 1995;29(12):1537–43.

88. Melvin JW, Haynes RR, Roberts VL, Alemt NM. Mechanical properties of cranial bone. *J. Biomech.*1970;3(5):495-511.

APPENDIX A: CALCULATIONS

1 M Na_2HPO_4 solution in 100 ml distilled water:

$$M = \frac{n}{v} = 1 = \frac{n}{0.1\ l} = 0.1\ mol$$

$$n = \frac{m}{m_a} = 0.1 = \frac{m}{141.96\ g} = 14.196\ grams$$

1:1 molar ratio TTCP:DCPD

$$m_{aTTCP} = 366.25 \frac{g}{mol}\ , m_{aDCPD} = 168.51 \frac{g}{mol}$$

For 0.673 grams of TTCP;

$$n = \frac{0.673\ g}{366.25\ g/mol} = 0.0018\ mol$$

0.0018 moles of DCPD;

$$0.0018 = \frac{m}{168.51} = 0.316\ grams\ of\ DCPD$$

1:2 molar ratio TTCP:DCPD

$$m_{aTTCP} = 366.25 \frac{g}{mol}\ , m_{aDCPD} = 168.51 \frac{g}{mol}$$

For 0.673 grams of TTCP;

$$n = \frac{0.673\ g}{366.25\ g/mol} = 0.0018\ mol$$

0.0036 moles of DCPD;

$$0.0036 = \frac{m}{168.51} = 0.632\ grams\ of\ DCPD$$

APPENDIX B: MECHANICAL TESTING RESULTS

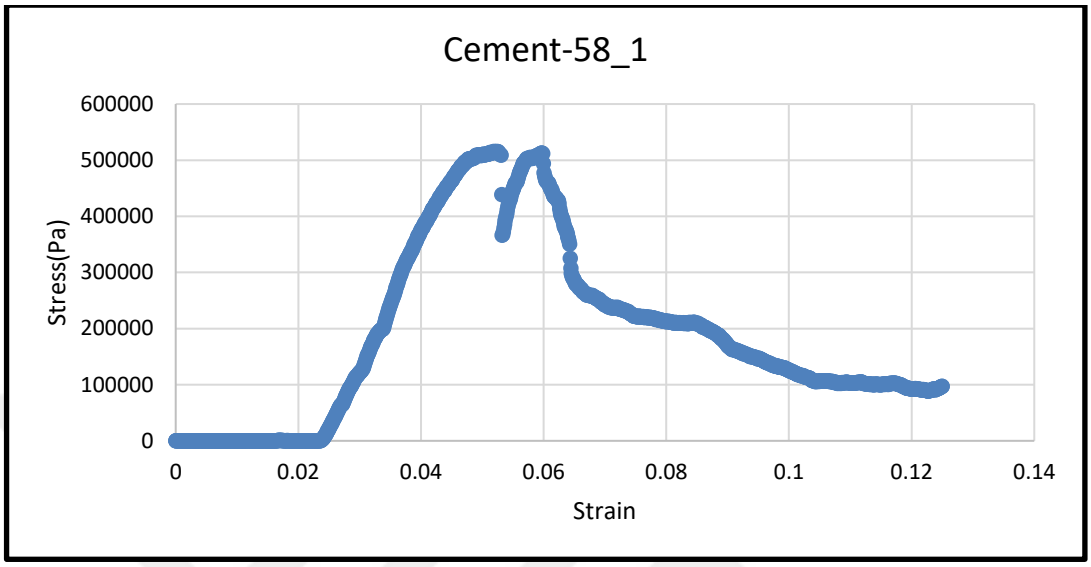

Figure B.1. Stress-Strain curve of cement-58_1

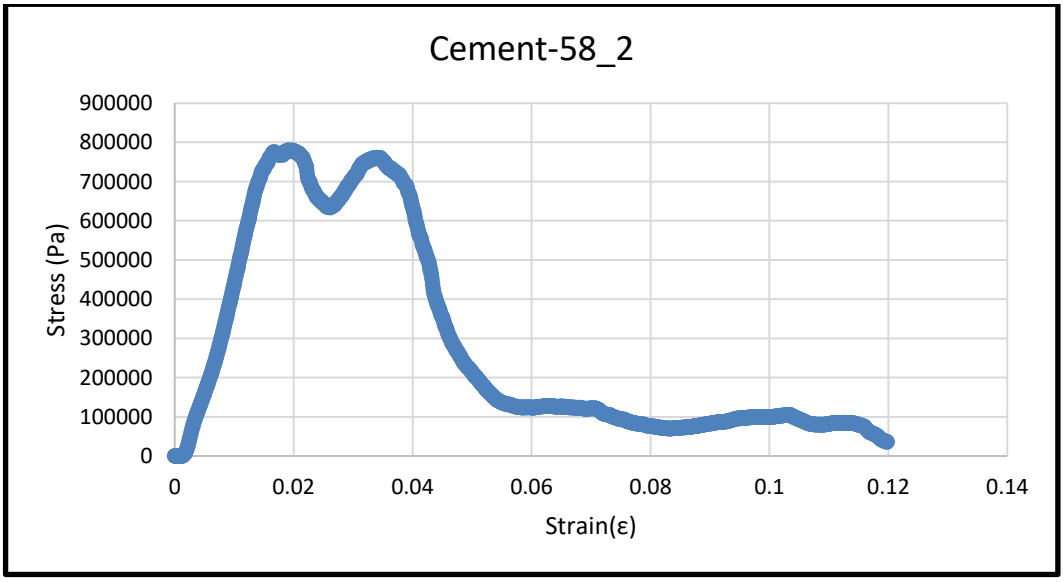

Figure B.2. Stress-Strain curve of cement-58_2

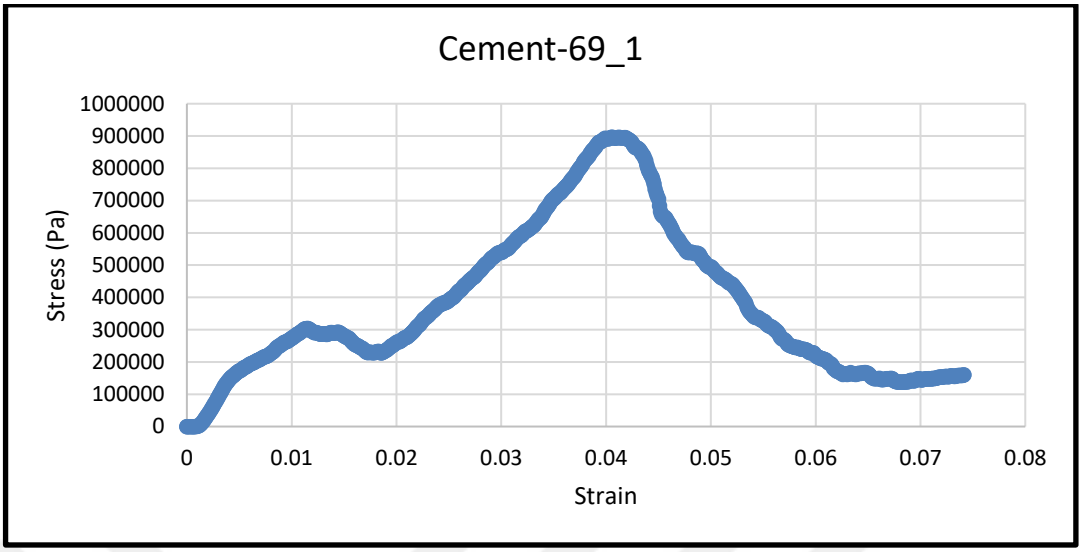

Figure B.3. Stress-Strain curve of cement-69_1

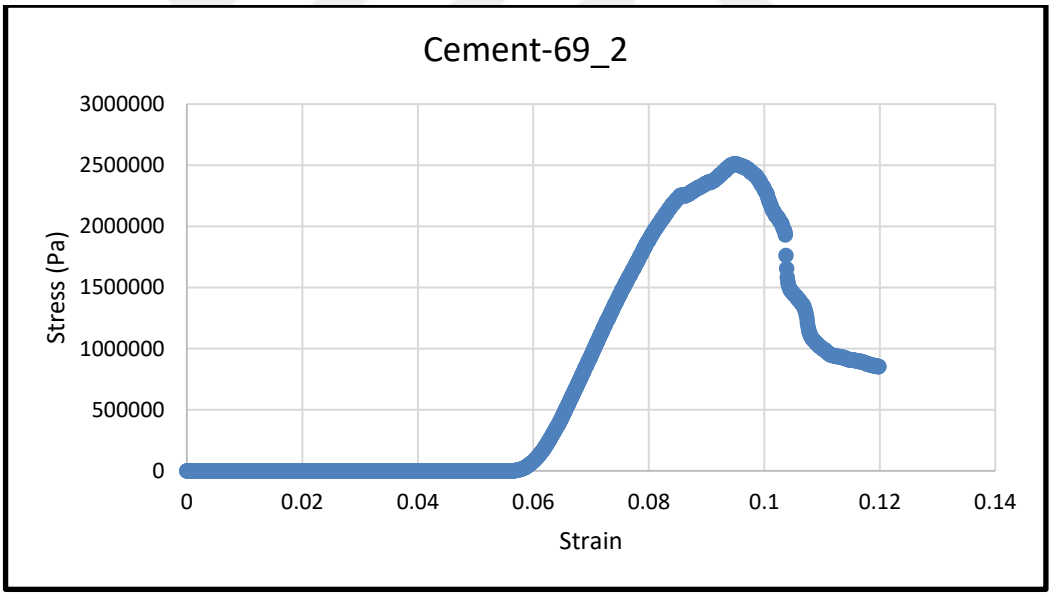

Figure B.4. Stress-Strain curve of cement-69_2

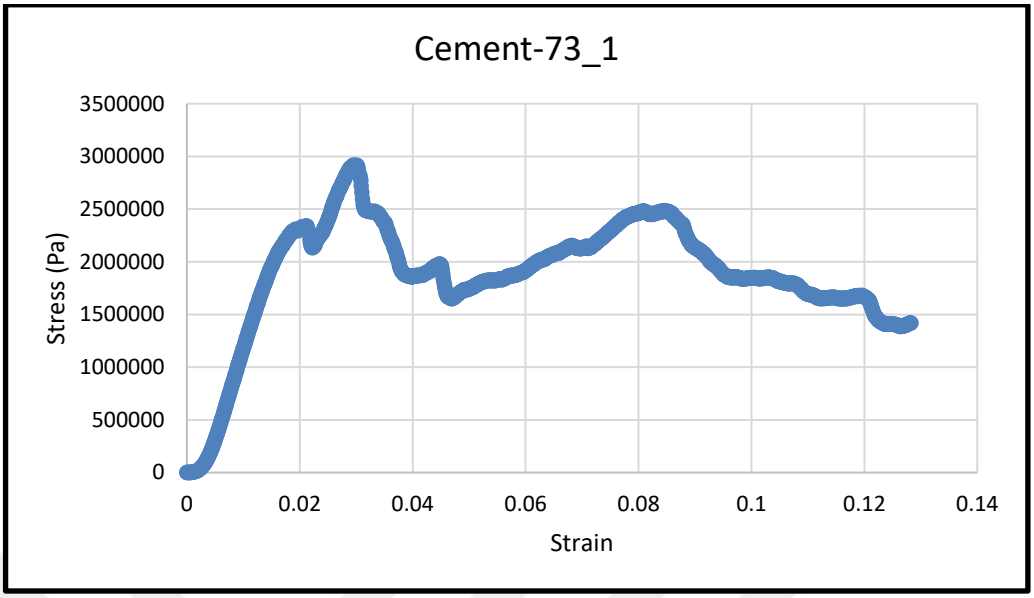

Figure B.5. Stress-Strain curve of cement-73_1

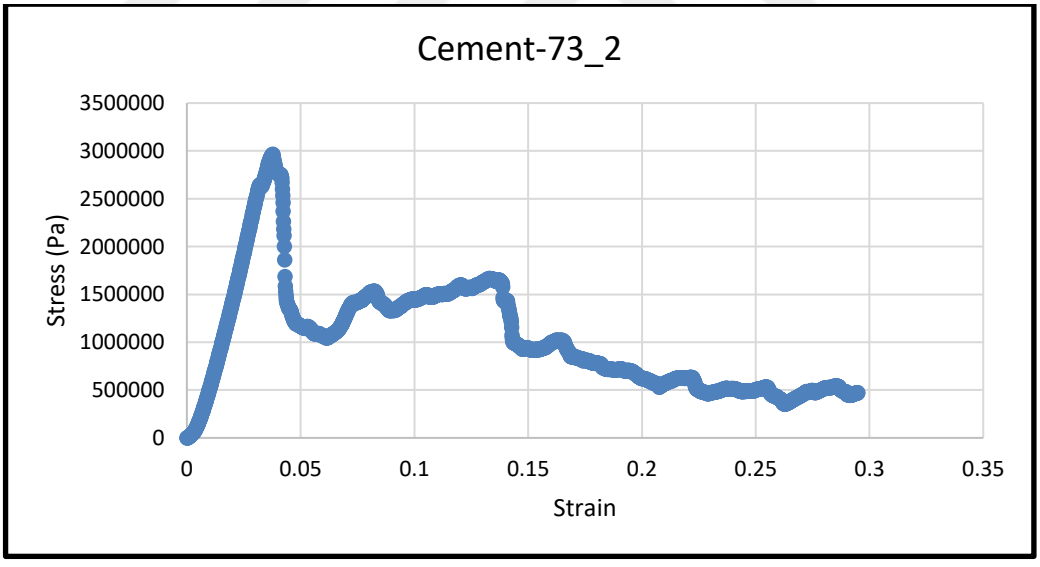

Figure B.6. Stress-Strain curve of cement-73_2

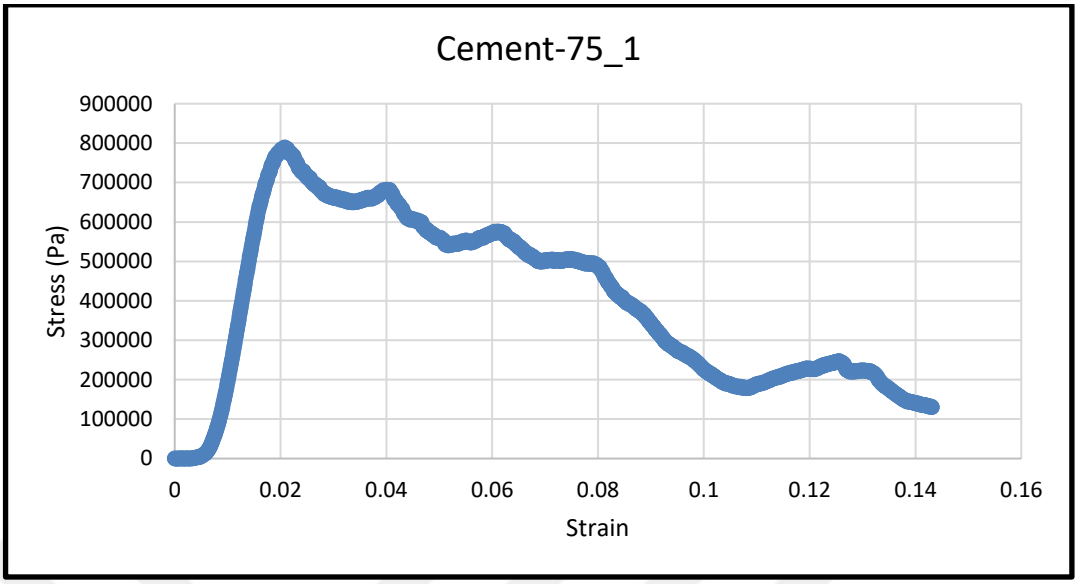

Figure B.7. Stress-Strain curve of cement-75_1

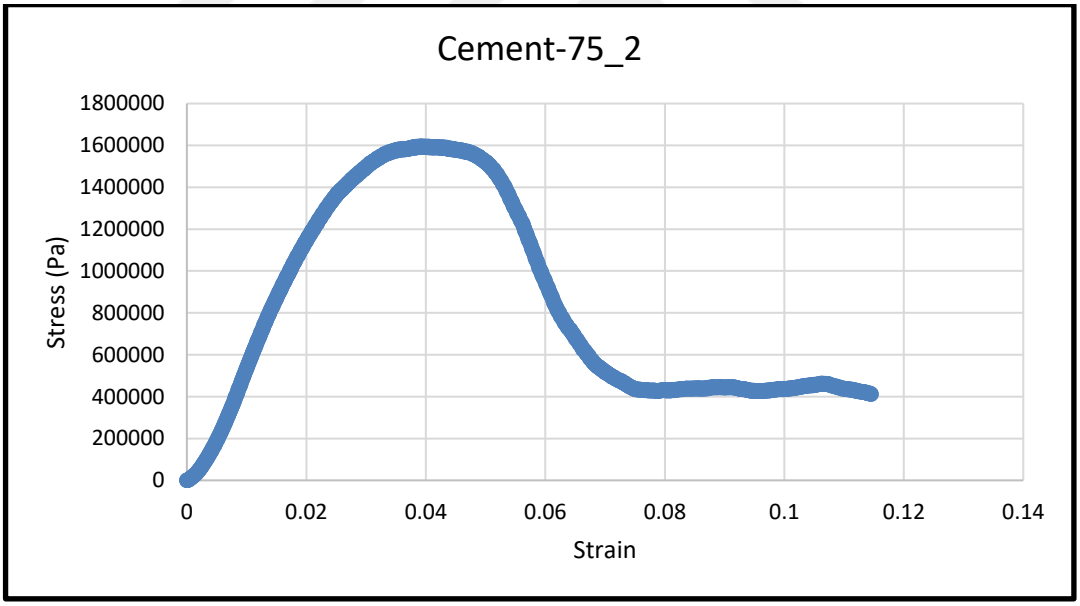

Figure B.8. Stress-Strain curve of cement-75_2

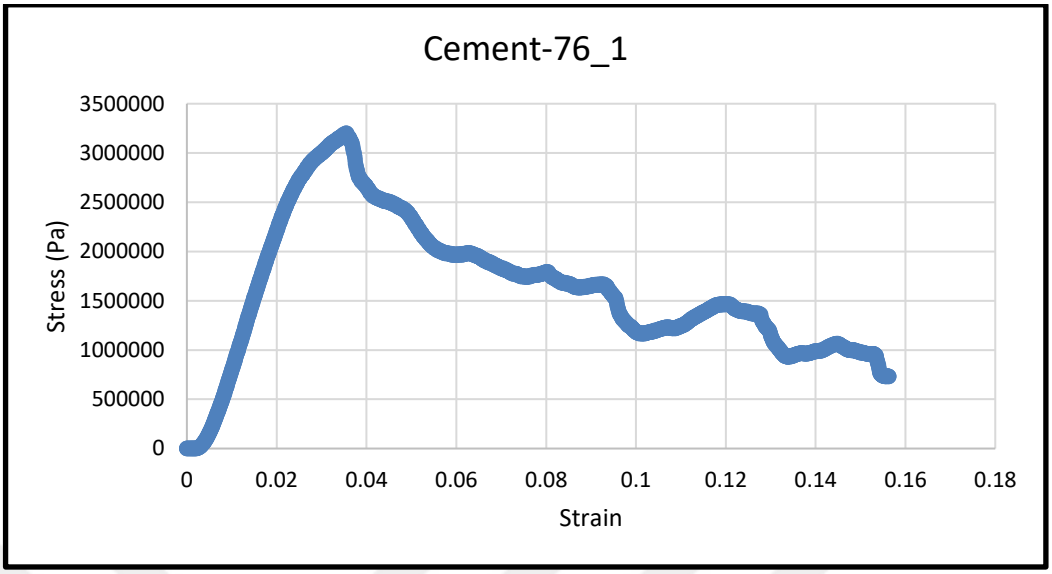

Figure B.9. Stress-Strain curve of cement-76C-5/37_1

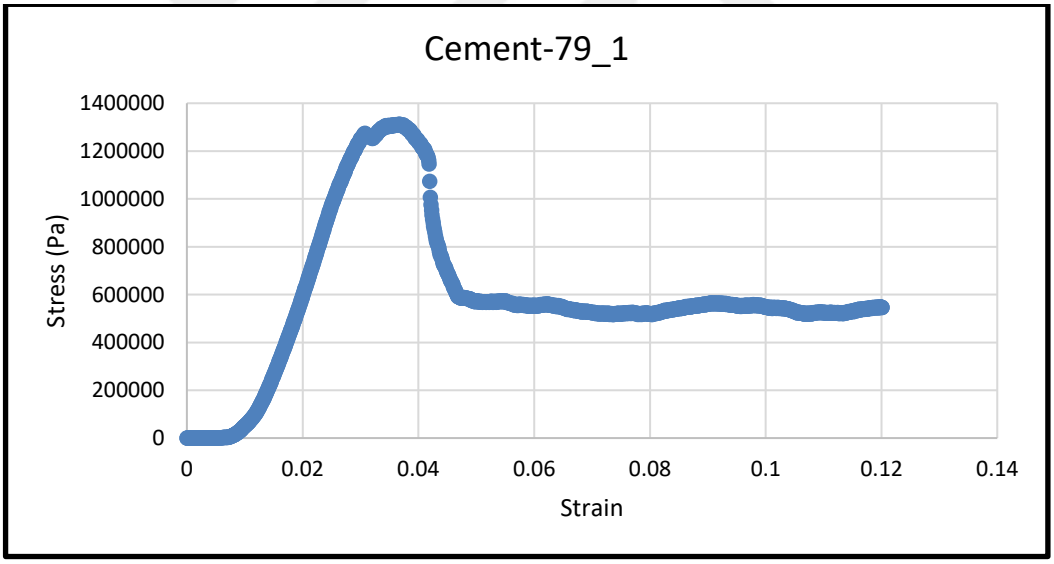

Figure B.10. Stress-Strain curve of Cement-79C-3/25_1

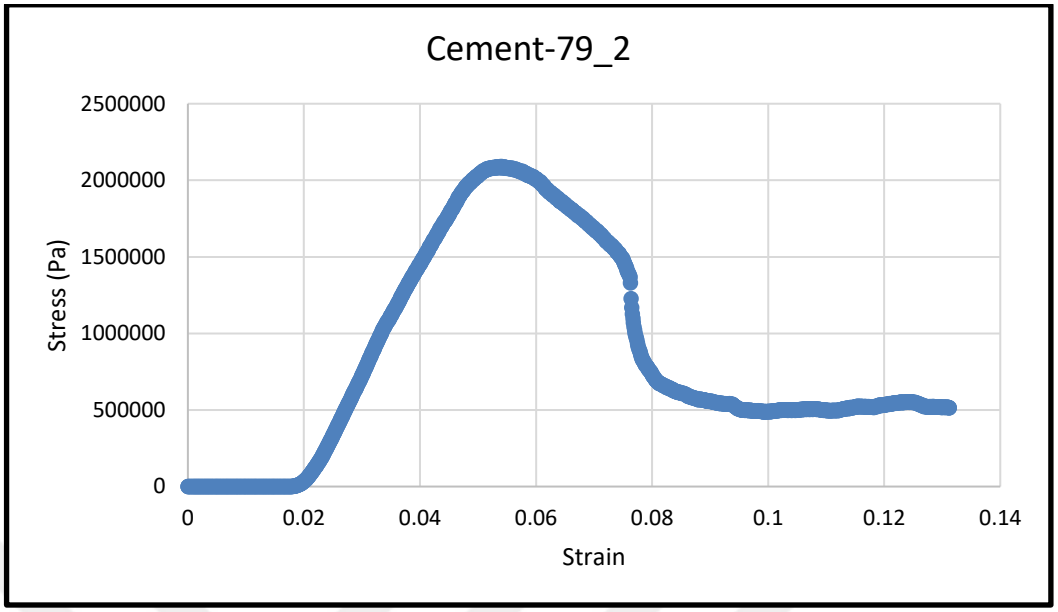

Figure B.11. Stress-Strain curve of Cement-79C-3/25_2

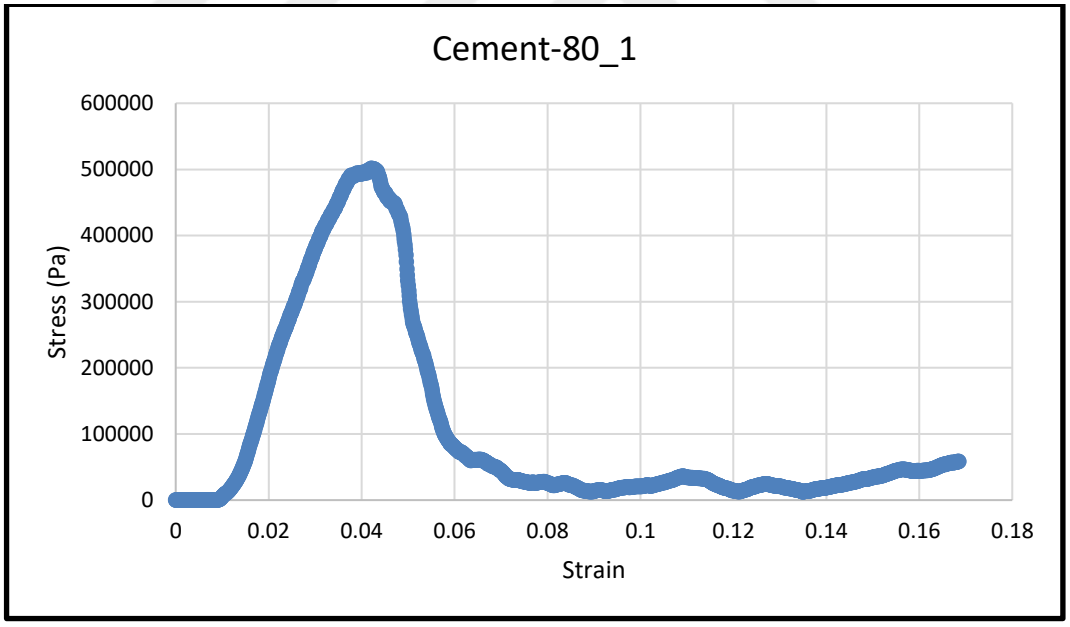

Figure B.12. Stress-Strain curve of Cement-80C-3/37_1

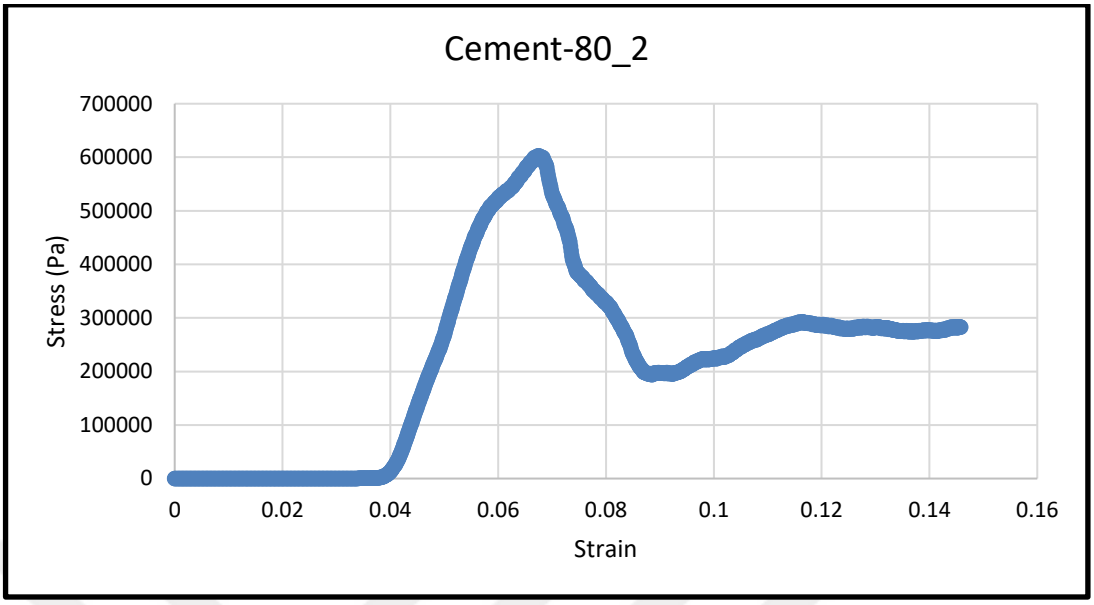

Figure B.13. Stress-Strain curve of Cement-80C-3/37_2

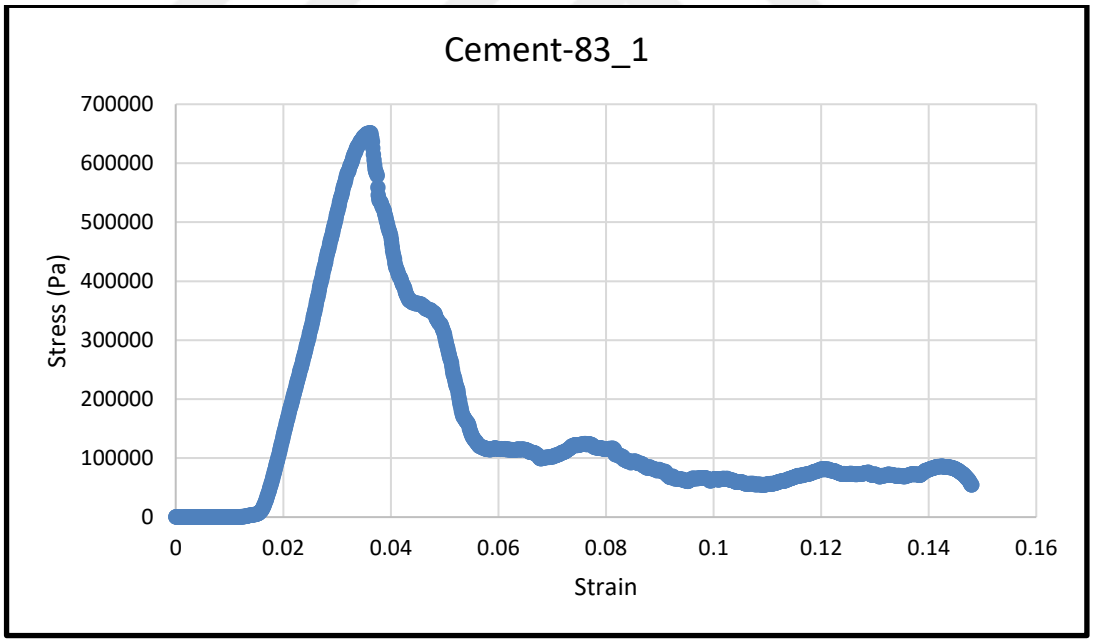

Figure B.14. Stress-Strain curve of cement-83_1

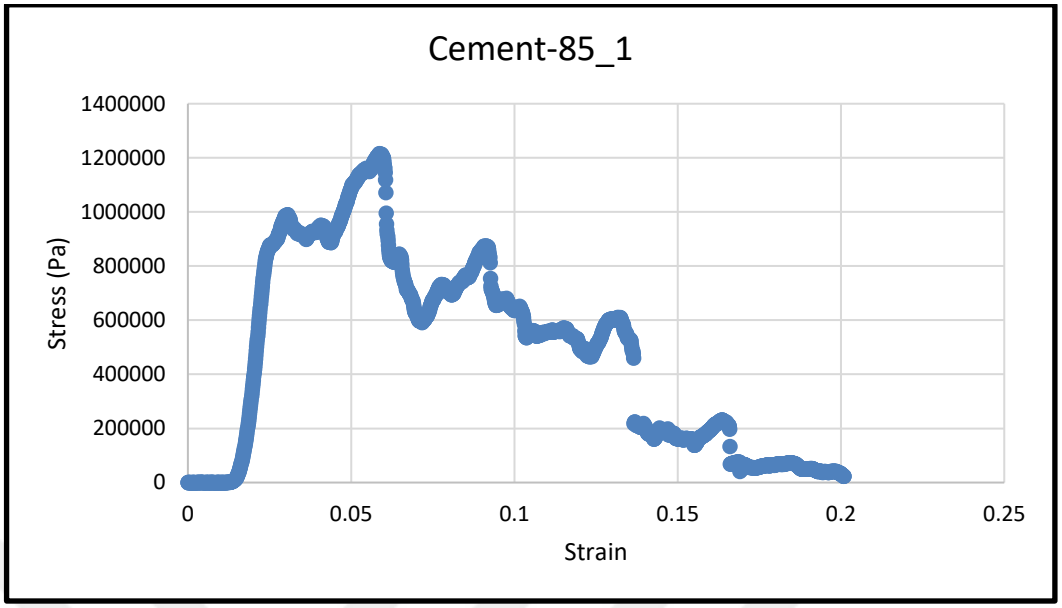

Figure B.15. Stress-Strain curve of cement-85_1

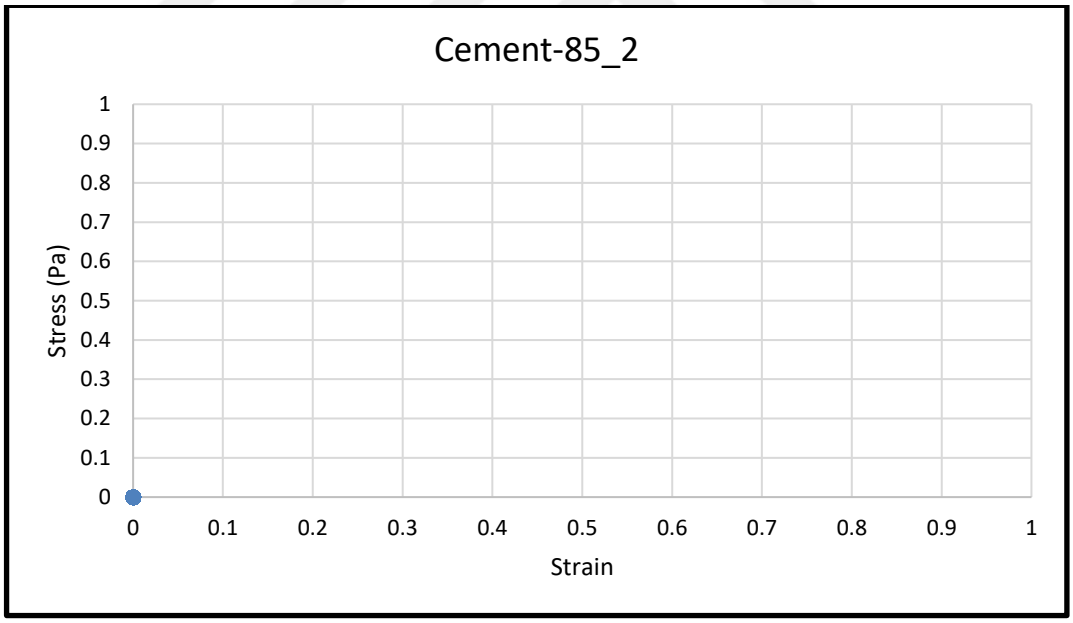

Figure B.16. Stress-Strain curve of cement-85_2

APPENDIX C: ETHICAL APPROVAL FORM

YEDİTEPE ÜNİVERSİTESİ

T.C. YEDİTEPE ÜNİVERSİTESİ, DENEY HAYVANLARI ETİK KURULU

(YÜDHEK)

ETİK KURUL KARARI

Toplantı Tarihi	Karar No	İlgi	Proje Yürütücüsü
01.08.2019	771	18.07.2019	Feride Şermin UTKU

'İpek polimer ve Ca-P kompozit biyomalzemenin sıçanlarda kranial dokuya osteoentegrasyonu' adlı bilimsel çalışma etik kurulumuzda görüşülmüş olup, çalışmanın etik kurallara uygun olduğuna oy birliğiyle karar verilmiştir.

Etik Onay Geçerlilik Süresi: 3 Yıl	Hayvan Türü ve cinsiyeti: Sıçan ♂	Hayvan Sayısı: 6

GÖREVİ	ADI SOYADI	
Başkan	Prof. Dr. Bayram YILMAZ	
Başkan Yardımcısı	Prof. Dr. Erdem YEŞİLADA	KATILMADI
Raportör	Vet. Hekim Engin SÜMER	
Üye	Prof. Dr. M. Ece GENÇ	
Üye	Prof. Dr. Rukset ATTAR	
Üye	Doç. Dr. Soner DOĞAN	KATILMADI
Üye	Doç. Dr. Ediz DENİZ	KATILMADI
Üye	Prof. Dr. Gamze TORUN KÖSE	
Üye	Doç. Dr. Aylin YABA UÇAR	KATILMADI
Üye	Hakan GÖKSEL	
Üye	Ahmet ŞENKARDEŞLER	